Interactions between Heliospheric and Ionospheric Plasma in Geospace

by

Huy-Sinh Trung

A dissertation submitted in partial fulfillment
of the requirements for the degree of
Doctor of Philosophy
(Physics)
in The University of Michigan
2022

Doctoral Committee:

Professor Karl Krushelnick, Co-Chair
Professor Michael Liemohn, Co-Chair
Dr. Natalia Ganushkina
Professor James Slavin
Professor Alexander Thomas

Huy-Sinh Trung

trungs@umich.edu

ORCID iD: 0000-0003-0884-573X

ACKNOWLEDGEMENTS

The completion of this thesis would not have been possible without my adviser, Professor Michael Liemohn. Mike encouraged me and believed in me when I did not believe in myself and my work. His empathy, tremendous support when I was having bouts of depression and anxiety helped me move forward slowly but surely.

I am very grateful to Professor Karl Krushelnick, Professor James Slavin, Professor Alexander Thomas, and Dr. Natalia Ganushkina in serving on my committee and their feedback in improving the content of this thesis.

I am deeply indebted to Professor Raluca Ilie from the University of Illinois in teaching me how to use the Space Weather Modeling Framework and teaching the ins and outs of the code. I would also like to thank Professor Dan Welling in providing examples of simulations using multifluid magnetohydrodynamics.

Lastly, I would like to thank my family for their encouragement, love, and support and putting up with me for the past few years.

The work generated in this thesis was supported by NASA under grants 80NSSC17K0015 and NNX17AB87G. My graduate years were also supported by a NASA Earth and Space Science Fellowship, a Rackham Merit Fellowship, Graduate Student Instructor positions, and Research Assistant positions. The data generated in this thesis was done through the use of NASA's High-End Computing.

TABLE OF CONTENTS

ACKNOWLEDGEMENTS ii

LIST OF FIGURES vi

LIST OF TABLES xiii

LIST OF ABBREVIATIONS xiv

ABSTRACT xv

CHAPTER

I. Introduction 1

1.1 Introduction 1
1.2 The Magnetosphere 2
1.3 The Ionosphere 4
1.4 Boundaries and the Geopause 5
1.5 Geopause Unanswered Questions 9
1.5.1 Question 1: How do the geopauses behave with respect to the magnetopause in steady state? 9
1.5.2 Question 2: How do the geopauses behave in response to the solar wind's magnetic field reversal? 9
1.5.3 Question 3: How do the force terms in the multifluid momentum equation relate to the geopauses? 10
1.6 Thesis Outline 10

II. Modeling the Magnetosphere 11

2.1 Magnetospheric Modeling 11
2.2 Boundary Conditions and Magnetospheric Plasma Sources . . 17
2.3 Ionospheric Modeling 17
2.4 Simulation Setup 20

III. Steady State Characteristics of the Terrestrial Geopause . . 25

3.1 Introduction 25
3.2 Methods 28
3.2.1 Global Magnetosphere Modeling 29
3.3 Results 31
3.3.1 Geopause comparisons from outflow 32
3.3.2 Comparisons between the geopauses and last closed field line 34
3.4 Discussion 36
3.5 Summary and Conclusions 43

IV. Transient Characteristics of the Terrestrial Geopause 46

4.1 Introduction 46
4.2 Methods 48
4.3 Results 50
4.3.1 Cross-Polar Cap Potential 52
4.3.2 Effect of outflow composition on nightside geopause dynamics 54
4.3.3 Comparison of Plasma Properties with Geopauses along the Sun-Earth Line 58
4.4 Discussion 61
4.5 Conclusion 64

V. Momentum Sources in Multifluid MHD and their Relation to the Geopauses 74

5.1 Introduction 74
5.2 Methods 76
5.3 Results 78
5.3.1 Case 1: Hydrogen only ionosphere, Northward IMF 79
5.3.2 Case 2: Oxygen only ionosphere, Northward IMF . 82
5.3.3 Case 1: Hydrogen only ionosphere, Southward IMF 88
5.3.4 Case 2: Oxygen only ionosphere, Southward IMF . 98
5.4 Discussion 104
5.5 Conclusion 111

VI. Conclusions 113

6.1 Summary 113
6.2 Study 1: Steady State Characteristics of the Terrestrial Geopause 114
6.3 Study 2: Transient Characteristics of the Terrestrial Geopause 114

6.4 Study 3: Momentum Sources in Multifluid MHD and their Relation to the Geopauses 115
6.5 Further work 116

Bibliography 117

LIST OF FIGURES

Figure

1.1 Conceptual illustration of the Earth's magnetosphere under the response of the solar wind. Credit: NASA/Goddard/Aaron Kaase . . 2

1.2 Schematic by *Kronberg et al.* (2014) of heavy ion trajectories in the Earth's magnetosphere under the response of various energy inputs (orange arrows). The red line are the magnetic fields. The green lines are the particle trajectories where ionized oxygen is non-negligible. The blue lines are the particle trajectories where ionized oxygen is insignificant. 6

1.3 Illustration summarizing the various processes (red letters) resulting from the Sun's interaction with the ionosphere and the ionospheric structures forming as a response. (*Hultqvist et al.*, 1999) 7

1.4 Diagram by *Moore and Delcourt* (1995) comparing the geopause to familiar magnetospheric boundaries. Top illustration shows the X-Z (meridional) plane. Middle cut shows the X-Y (equatorial) plane. The sun is on the left for both top and middle cuts. Bottom cut is the Y-Z plane looking from the Sun to the Earth. The plasma number density is indicated by the grey colors. The darker the grey, the denser the plasma density is. 8

2.1 Typical conductivity values in the midlatitude daytime ionosphere (*Kelley*, 2009). The Pedersen conductivity, σ_P , and the Hall conductivity, σ_H, are scaled relative to the parallel conductivity, σ_0. The dashed line is a typical nighttime Pedersen conductivity profile. . . 18

2.2 Diagram of timescales and lengthscales of various plasma systems in the solar system (*Tóth et al.*, 2012). 22

3.1 Number density geopause (a) Top left, meridional cut for northward IMF. (b) Top right, meridional cut for southward IMF. (c) Bottom left, equatorial cut for northward IMF. (d) Bottom left, equatorial cut for southward IMF. 37

3.2 Mass density geopause (a) Top left, meridional cut for northward IMF. (b) Top right, meridional cut for southward IMF. (c) Bottom left, equatorial cut for northward IMF. (d) Bottom left, equatorial cut for southward IMF. 38

3.3 Pressure geopause (a) Top left, meridional cut for northward IMF. (b) Top right, meridional cut for southward IMF. (c) Bottom left, equatorial cut for northward IMF. (d) Bottom left, equatorial cut for southward IMF. 39

3.4 (a) Left, magnetopause projection in the meridional plane when the IMF is northward. (b) Right, magnetopause projection in the meridional plane when the IMF is southward. 40

3.5 Geopauses for a plasma composed of solar wind and ionospheric hydrogen in the meridional plane. (a) Left, northward IMF. (b) Right, southward IMF. Note that the mass density geopause and the number density geopause are identical. 41

3.6 Geopauses for a plasma composed of solar wind hydrogen and ionospheric oxygen in the meridional plane. (a) Left, northward IMF. (b) Right, southward IMF. 42

3.7 Geopauses for a plasma composed of solar wind hydrogen, ionospheric hydrogen and oxygen in the meridional plane. (a) Left, northward IMF. (b) Right, southward IMF. 43

3.8 Geopauses for a plasma composed of solar wind hydrogen, ionospheric hydrogen and oxygen in the meridional plane for an inner boundary mass density of 28 amu/cm^3. (a) Left, northward IMF. (b) Right, southward IMF. 44

4.1 Plots of the various geopause definitions at 08:30 UT for a plasma composed of solar wind hydrogen and ionospheric oxygen (Case 2) for the solar wind magnetic field configuration going from North to South. Top left: Meridional cut of the geopauses. Top right: Equatorial cut of the geopauses. Bottom: Solar wind magnetic field in the z-direction as a function of time plotted in red, blue line corresponds to 0, and the dashed black line is a visual indicator of the current time in the simulation. 52

4.2 Plots of the various geopause definitions at 09:00 UT for a plasma composed of solar wind hydrogen and ionospheric oxygen (Case 2) for the solar wind magnetic field configuration going from North to South. Top left: Meridional cut of the geopauses. Top right: Equatorial cut of the geopauses. Bottom: Solar wind magnetic field in the z-direction as a function of time plotted in red, blue line corresponds to 0, and the dashed black line is a visual indicator of the current time in the simulation. 53

4.3 Plots of cross-polar cap potential. (a) Left, CPCP for the South-to-North IMF configuration. The dashed vertical line at 04:00 UT corresponds to the IMF reversal from South-to-North. (b) Right, CPCP for the North-to-South IMF configuration. The dashed vertical line at 08:00 UT corresponds to the IMF reversal from North-to-South. . 66

4.4 Time series of the nightside number density geopause along the Sun-Earth line (a) Left, South-to-North IMF configuration. The dashed vertical line at 04:00 UT corresponds to the IMF reversal from South-to-North. (b) Right, North-to-South IMF configuration. The dashed vertical line at 08:00 UT corresponds to the IMF reversal from North-to-South. 67

4.5 Time series of the nightside mass density geopause along the Sun-Earth line (a) Left, South-to-North IMF configuration. The dashed vertical line at 04:00 UT corresponds to the IMF reversal from South-to-North. (b) Right, North-to-South IMF configuration. The dashed vertical line at 08:00 UT corresponds to the IMF reversal from North-to-South. 68

4.6 Time series of the nightside pressure geopause along the Sun-Earth line (a) Left, South-to-North IMF configuration. The dashed vertical line at 04:00 UT corresponds to the IMF reversal from South-to-North. (b) Right, North-to-South IMF configuration. The dashed vertical line at 08:00 UT corresponds to the IMF reversal from North-to-South. 69

4.7 Time series of the nightside geopauses along the negative x axis for a plasma composed of solar wind hydrogen and ionospheric hydrogen. Top row, y-component of the current density. Middle row, solar wind velocity in the x-direction. Bottom row, z-component of the magnetic field. Left column, South-to-North IMF configuration. The dashed vertical line at 04:00 UT corresponds to the IMF reversal from South-to-North. Right column, North-to-South IMF configuration. The dashed vertical line at 08:00 UT corresponds to the IMF reversal from North-to-South. Note that the number density and mass density geopauses are identical. 70

4.8 Time series of the nightside geopauses along the Sun-Earth line for a plasma composed of solar wind hydrogen and ionospheric oxygen. Top row, y-component of the current density. Middle row, solar wind velocity in the x-direction. Bottom row, z-component of the magnetic field. Left column, South-to-North IMF configuration. The dashed vertical line at 04:00 UT corresponds to the IMF reversal from South-to-North. Right column, North-to-South IMF configuration. The dashed vertical line at 08:00 UT corresponds to the IMF reversal from North-to-South. 71

4.9 Time series of the nightside geopauses along the Sun-Earth line for a plasma composed of solar wind hydrogen, and ionospheric hydrogen and oxygen. Top row, y-component of the current density. Middle row, solar wind velocity in the x-direction. Bottom row, z-component of the magnetic field. Left column, South-to-North IMF configuration. The dashed vertical line at 04:00 UT corresponds to the IMF reversal from South-to-North. Right column, North-to-South IMF configuration. The dashed vertical line at 08:00 UT corresponds to the IMF reversal from North-to-South. 72

4.10 Time series of the nightside geopauses along the Sun-Earth line for a plasma composed of solar wind hydrogen, and ionospheric hydrogen and oxygen at an inner boundary mass density of 28 amu/cm^3. Top row, y-component of the current density. Middle row, solar wind velocity in the x-direction. Bottom row, z-component of the magnetic field. Left column, South-to-North IMF configuration. The dashed vertical line at 04:00 UT corresponds to the IMF reversal from South-to-North. Right column, North-to-South IMF configuration. The dashed vertical line at 08:00 UT corresponds to the IMF reversal from North-to-South. 73

5.1 Force densities of ionospheric hydrogen for the simulation of solar wind hydrogen with ionospheric hydrogen during northward IMF. Top row: X-component of the gyration force density (a), bulk terms (b), and friction (c). Bottom row: Z-component of the gyration force density (d), bulk terms (e), and friction (f) 83

5.2 Force densities ratios of ionospheric hydrogen for the simulation of solar wind hydrogen with ionospheric hydrogen during northward IMF. Top row: X-component of the gyration force density (a), bulk terms (b), and friction (c). Bottom row: Z-component of the gyration force density (d), bulk terms (e), and friction (f) 84

5.3 Force densities of solar wind hydrogen for the simulation of solar wind hydrogen with ionospheric hydrogen during northward IMF. Top row: X-component of the gyration force density (a), bulk terms (b), and friction (c). Bottom row: Z-component of the gyration force density (d), bulk terms (e), and friction (f) 85

5.4 Force densities ratios of solar wind hydrogen for the simulation of solar wind hydrogen with ionospheric hydrogen during northward IMF. Top row: X-component of the gyration force density (a), bulk terms (b), and friction (c). Bottom row: Z-component of the gyration force density (d), bulk terms (e), and friction (f) 86

5.5 Force densities of ionospheric oxygen for the simulation of solar wind hydrogen with ionospheric oxygen during northward IMF. Top row: X-component of the gyration force density (a), bulk terms (b), and friction (c). Bottom row: Z-component of the gyration force density (d), bulk terms (e), and friction (f) 89

5.6 Force densities ratios of ionospheric oxygen for the simulation of solar wind hydrogen with ionospheric oxygen during northward IMF. Top row: X-component of the gyration force density (a), bulk terms (b), and friction (c). Bottom row: Z-component of the gyration force density (d), bulk terms (e), and friction (f) 90

5.7 Force densities of solar wind hydrogen for the simulation of solar wind hydrogen with ionospheric oxygen during northward IMF. Top row: X-component of the gyration force density (a), bulk terms (b), and friction (c). Bottom row: Z-component of the gyration force density (d), bulk terms (e), and friction (f) 91

5.8 Force densities ratios of solar wind hydrogen for the simulation of solar wind hydrogen with ionospheric oxygen during northward IMF. Top row: X-component of the gyration force density (a), bulk terms (b), and friction (c). Bottom row: Z-component of the gyration force density (d), bulk terms (e), and friction (f) 92

5.9 Force densities of ionospheric hydrogen for the simulation of solar wind hydrogen with ionospheric hydrogen during southward IMF. Top row: X-component of the gyration force density (a), bulk terms (b), and friction (c). Bottom row: Z-component of the gyration force density (d), bulk terms (e), and friction (f) 94

5.10 Force densities ratios of ionospheric hydrogen for the simulation of solar wind hydrogen with ionospheric hydrogen during southward IMF. Top row: X-component of the gyration force density (a), bulk terms (b), and friction (c). Bottom row: Z-component of the gyration force density (d), bulk terms (e), and friction (f) 95

5.11 Force densities of solar wind hydrogen for the simulation of solar wind hydrogen with ionospheric hydrogen during southward IMF. Top row: X-component of the gyration force density (a), bulk terms (b), and friction (c). Bottom row: Z-component of the gyration force density (d), bulk terms (e), and friction (f) 96

5.12 Force densities ratios of solar wind hydrogen for the simulation of solar wind hydrogen with ionospheric hydrogen during southward IMF. Top row: X-component of the gyration force density (a), bulk terms (b), and friction (c). Bottom row: Z-component of the gyration force density (d), bulk terms (e), and friction (f) 97

5.13 Force densities of ionospheric oxygen for the simulation of solar wind hydrogen with ionospheric hydrogen during southward IMF. Top row: X-component of the gyration force density (a), bulk terms (b), and friction (c). Bottom row: Z-component of the gyration force density (d), bulk terms (e), and friction (f) 100

5.14 Force densities ratios of ionospheric oxygen for the simulation of solar wind hydrogen with ionospheric hydrogen during southward IMF. Top row: X-component of the gyration force density (a), bulk terms (b), and friction (c). Bottom row: Z-component of the gyration force density (d), bulk terms (e), and friction (f) 101

5.15 Force densities of solar wind hydrogen for the simulation of solar wind hydrogen with ionospheric hydrogen during southward IMF. Top row: X-component of the gyration force density (a), bulk terms (b), and friction (c). Bottom row: Z-component of the gyration force density (d), bulk terms (e), and friction (f) 102

5.16 Force densities ratios of solar wind hydrogen for the simulation of solar wind hydrogen with ionospheric hydrogen during southward IMF. Top row: X-component of the gyration force density (a), bulk terms (b), and friction (c). Bottom row: Z-component of the gyration force density (d), bulk terms (e), and friction (f) 103

LIST OF TABLES

Table

3.1 Inner Boundary Conditions. Sw is short for solar wind and Io is short for ionospheric. 32

4.1 Inner Boundary Conditions. Sw is short for solar wind and Io is short for ionospheric. 51

4.2 Summary of response timings for the South-to-North IMF simulations. Sw is short for solar wind and Io is short for ionospheric. . . . 57

4.3 Summary of spike timings for North-to-South IMF simulations. Sw is short for solar wind and Io is short for ionospheric. 58

5.1 Inner boundary conditions 78

5.2 Summary of results for Case 1 (ionospheric H^+) with northward IMF 104

5.3 Summary of Case 2 (ionospheric O^+) results with northward IMF . 105

5.4 Summary of Case 3 (ionospheric H^+) results with southward IMF . 106

5.5 Summary of Case 4 (ionospheric O^+) results with southward IMF . 107

LIST OF ABBREVIATIONS

AU astronomical unit

CME coronal mass ejection

IMF inteplanetary magnetic field

MHD magnetohydrodynamics

SWMF Space Weather Modeling Framework

ABSTRACT

The Sun interacts with the Earth through electromagnetic radiation, gravitationally, and through the solar wind. The solar wind carrying the Sun's magnetic field interacts with the Earth's magnetosphere and drives the dynamics of near Earth space. In near Earth space, plasma from the Earth's ionosphere can be accelerated into the Earth's magnetosphere due to the dynamics induced by the solar wind. The ionospheric plasma can then interact with the solar wind plasma. In this thesis, we explore the concept of a geopause, a surface defined where solar wind and ionospheric plasma quantities are equal. For example, the number density geopause is defined where the solar wind number density equals the ionospheric plasma number density.

We simulated the geospace environment through the Space Weather Modeling Framework by employing its multifluid magnetohydrodynamics model to track the velocities, mass densities, and pressures of the heliospheric and ionospheric plasmas separately. The Earth's spin axis and magnetic field were aligned for our numerical simulations in order to isolate the effects of the solar wind magnetic field. We performed numerical experiments where the solar wind number density, pressure, and velocities were kept constant but the solar wind magnetic field had two different configurations. The two configurations used were 1) the solar wind magnetic field was kept parallel to the Earth's spin axis (northward) and then flipped very quickly to be antiparallel to the Earth's spin axis (southward) 2) the solar wind magnetic field was kept southward and then flipped northward. The ionospheric inner bound-

ary was kept to have no radial velocity and solely driven by magnetohydrodynamics forces with four different ion compositions of the ionosphere. The compositions used were a hydrogen ionosphere, a hydrogen oxygen ionosphere mix with a mass density equal to the pure hydrogen ionosphere case, an ionosphere composed of hydrogen and oxygen equal in number density, and an oxygen only ionosphere. These numerical experiments generated over 12 hours of simulation data.

Over the course of the 12 hours of simulation data, we recorded the location of the mass density, number density, and pressure geopauses. In one study, we analyzed the geopauses throughout the simulation to examine the relation of the geopause size in response to the ionospheric composition and the conditions in the solar wind magnetic field. At the last time step of the simulation, we generated another study by comparing the mass density, number density, and pressure geopauses to the magnetopause in steady state to understand whether one physical process governed the transition in a plasma being dominated by the solar wind to the ionospheric plasma. In the last study, we calculated the source terms in the momentum equations at 12:00 and compared them to the geopauses to develop an understanding in the physical properties of the geopauses.

CHAPTER I

Introduction

1.1 Introduction

The most common state of ordinary matter in the universe is the plasma state. In this state of matter, gases are ionized and its dynamics are influenced by electric and magnetic fields. Objects in the universe that are commonly found in the plasma state are stars. On Earth, plasmas can be used in industrial applications such as material processing (*Bonizzoni and Vassallo*, 2002). Experimentally, plasmas have been used in controlled nuclear fusion settings with tokamaks and stellarators.

In the solar system, the Sun provides a steady stream of plasma in the form of the solar wind. The solar wind is emitted in all directions. It escapes from the solar corona which has a temperature of 10^6 K. The solar wind is a plasma mainly dominated by hydrogen. The outflow of the solar wind plasma also transports the Sun's magnetic field throughout the solar system. At 1 astronomical unit (AU), the solar wind has an average magnetic field intensity of 5.1 nT, an average speed of 410 km/s, an average density of 5.5 cm^{-3}, and an average proton temperature of 10 eV (*Klein and Vech*, 2019).

1.2 The Magnetosphere

When one mentions the word magnetosphere, we refer to the region of space near a body (in this case Earth) where its magnetic field is dominant. Without an external source of plasma with a magnetic field, the Earth's magnetic field is well approximated as a dipole. With the presence of the solar wind, the Earth's magnetic field is altered under the response of the transported solar magnetic field (called interplanetary magnetic field), kinetic pressure and thermal pressure. Fig. 1.1 has a conceptual illustration of the shape of the Earth's magnetosphere.

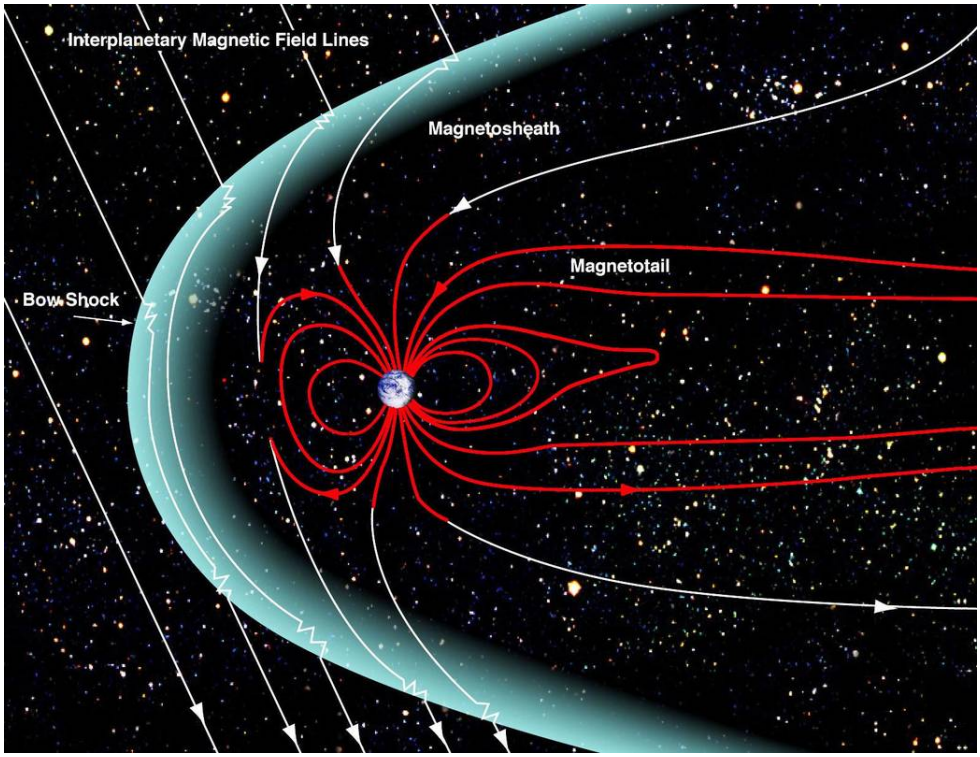

Figure 1.1: Conceptual illustration of the Earth's magnetosphere under the response of the solar wind. Credit: NASA/Goddard/Aaron Kaase

Understanding the interactions between the solar wind and the magnetosphere has both economic and scientific value. Space weather events (magnetospheric disturbances by the solar wind) can be very damaging. In recent history, a 1989 geomagnetic storm resulted in a power grid failure in Québec, and a 2003 Halloween

geomagnetic storm caused a 90 minute power grid blackout for over 50000 customers in Sweden (*Eastwood et al.*, 2017). In terms of scientific value, it is a natural laboratory to study plasma physics. The Magnetospheric Multiscale Mission (MMS) was launched in order to probe regions where magnetic reconnection occurred (*Burch et al.*, 2016a). Magnetic reconnection converts magnetic energy into kinetic energy for the local plasma (*Priest and Forbes*, 2000). In October 2015, MMS directly observed magnetic reconnection in the Earth's magnetopause (*Burch et al.*, 2016b).

In the most favorable conditions for magnetospheric activity, the solar wind has a magnetic field that is antiparallel to the Earth's magnetic field. The solar wind interacts with the Earth's magnetosphere at the magnetopause, a boundary separating the solar wind and magnetospheric plasma. At this boundary, magnetic reconnection will be maximized. The local environment for magnetic reconnection dictates the rate at which magnetic energy is converted to kinetic energy (*Cassak and Shay*, 2007). For the Sun-Earth system, this means that some magnetic field lines from the Sun will merge with the Earth's magnetic field in that reconnection region. This enables the solar wind plasma to enter the Earth's magnetosphere. Some of the solar wind will carry the magnetic flux from the Earth's dayside (the Sun illuminated side of the Earth) to the Earth's nightside (the non-illuminated side of the Earth).

The transport of magnetic flux from the dayside to the nightside flux elongates the dipolar terrestrial magnetic field. To support the elongation of the dipolar magnetic field, a current sheet is formed. The magnetic field of the magnetotail along with the right solar wind conditions (namely antiparallel magnetic field) can trigger magnetic reconnection and a fast release in energy from the magnetotail to the Earth's ionosphere.

In the Earth's magnetosphere, there are two sources of magnetospheric plasma. One source is the solar wind while the other source is the ionosphere. To enter the magnetosphere, the solar wind must cross the magnetopause through magnetic

reconnection, turbulent exchange through the boundary, or convection accross the boundary. For the ionosphere to enter the magnetosphere, it must overcome the force of gravity in the upper atmosphere. The details will be covered in the next section.

1.3 The Ionosphere

The other major source of plasma in the Earth's magnetosphere is the ionosphere. The solar wind used to be thought of as the sole contributor to magnetospheric dynamics. However, *Shelley et al.* (1972) analyzed data from a polar orbiting satellite and showed that ionized oxygen fluxes was frequently larger than ionized hydrogen fluxes during geomagnetic storm periods. Those observations were carried over a wide range of latitudes. *Sharp et al.* (1982) used satellite measurements to show that ionospheric plasma could dominate the plasma sheet during active times. Further observations by *Young et al.* (1982); *Chappell et al.* (1987) supported the idea that ionized oxygen played a non negligible role in magnetospheric structure and dynamics.

The ionosphere is located about 50 km above the Earth's surface and extends up to 1000 km above the Earth's surface. The ionosphere forms as a result of the absorption of solar photons at the EUV and X-ray wavelengths by the atmosphere. This results into the ionization of the neutral gas and the production of ionized particles.

At the magnetospheric level, the energy inputs into the Earth's ionosphere are electron precipitation, Poynting flux, and extreme ultraviolet (EUV) radiation. The outflow ionospheric species are ionized hydrogen, singly ionized helium, and singly ionized oxygen. The ionospheric outflow is typically dominated by hydrogen but can also have significant amounts of oxygen during magnetospheric active times (*Maggiolo and Kistler*, 2014).

In the near Earth current sheet, ionized helium makes up 2.5 % by number density of the total plasma compared to ionized oxygen which makes up 7.5 % of the total plasma during quiet times. In active times, ionized helium only makes up 0.5 % of the

total plasma while ionized oxygen makes up 9 % of the total plasma (*Gloeckler and Hamilton*, 1987). Fig. 1.2 summarizes the various energy inputs and the ionospheric outflows to the magnetosphere.

At the ionospheric level, processes contributing to the energization of ionospheric plasma include frictional heating, broadband waves, lower hybrid waves, ion cyclotron waves, solitary kinetic Alfvén waves, and centrifugal acceleration (*Hultqvist et al.*, 1999). Frictional heating results from the interaction of the ionospheric plasma with the neutral atmosphere. The rest of these processes (minus centrifugal acceleration) are plasma processes. These processes help in accelerating ionospheric plasma into the magnetosphere. However, in this thesis these processes are not directly modeled. The ionospheric model that is going to be discussed in chapter 2 indirectly takes into account these processes through the conductance model.

1.4 Boundaries and the Geopause

Within the magnetosphere, there are different plasma structures with distinct number densities and temperatures. These plasma structures contain ionospheric, heliospheric plasma, or a combination of both.

One such structure is the plasmasphere. The plasmasphere is formed as a result of the escape of ionospheric ions along magnetic field lines from the Earth's sunlit side. With the Earth's rotation also carrying the magnetic field lines, the resulting structure is a torus extending to about 4 R_E. The plasmasphere number density ranges from 10 to 10^4 cm^{-3}, has temperatures of about 1 eV, and is composed of H^+ ($\sim$ 80% by number density), He^+ ($\sim$ 10-20% by number density), and O^+ (several percent by number density, highly dependent on magnetospheric activity) (*Goldstein*, 2007). The boundary of the plasmasphere is called the plasmapause. It is a region defined by a drop off in the plasma number density by 1 to 2 orders of magnitude (*Chappell et al.*, 1970).

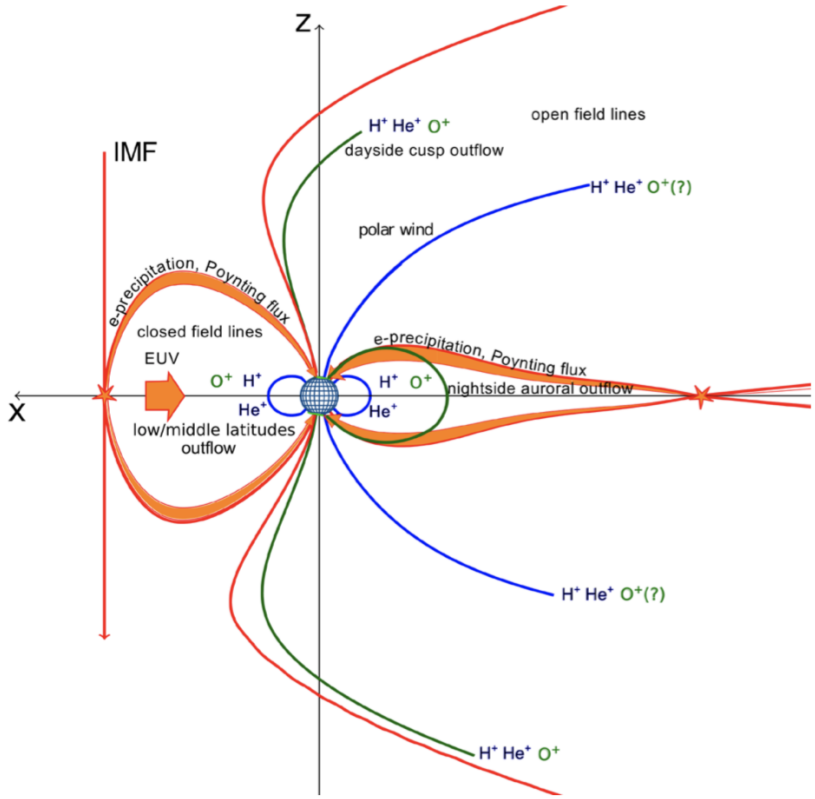

Figure 1.2: Schematic by *Kronberg et al.* (2014) of heavy ion trajectories in the Earth's magnetosphere under the response of various energy inputs (orange arrows). The red line are the magnetic fields. The green lines are the particle trajectories where ionized oxygen is non-negligible. The blue lines are the particle trajectories where ionized oxygen is insignificant.

Another plasma region is the plasma mantle. The plasma mantle consists of plasma in the high latitudes of the magnetosphere originating from inflowing shocked solar wind plasma. It can enter the magnetosphere through the cusps (regions where the Earth's magnetic field lines transition from closing in the dayside to closing in the nightside). The plasma mantle has temperatures close to the shocked solar wind (ranging from 0.05 to 0.2 keV) and a number density of about 0.1 to 1 cm^{-3} (*Wang et al.*, 2014).

The low latitude boundary layer (LLBL) is a boundary layer located inside of the magnetopause and is composed of solar wind plasma and ionospheric plasma. Observations have shown that the LLBL have at least two layers, an inner layer and

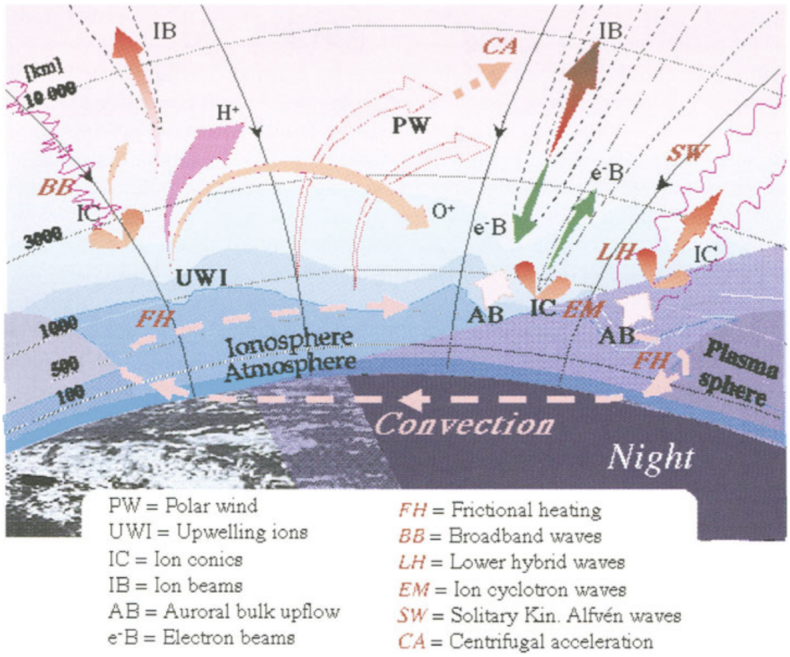

Figure 1.3: Illustration summarizing the various processes (red letters) resulting from the Sun's interaction with the ionosphere and the ionospheric structures forming as a response. (*Hultqvist et al.*, 1999)

an outer layer. The outer layer has plasma properties similar to the magnetosheath (shocked solar wind) plasma and the inner layer has plasma properties similar to the magnetospheric plasma (*Nakamura*, 2021).

The magnetopause is thought of as the boundary separating solar wind plasma and magnetospheric plasma. Physically, the magnetopause represents a location where magnetic field lines transition from connecting to Earth to connecting to the solar wind (*Borovsky and Valdivia*, 2018). In the simplest model of the dayside magnetopause, it is found as a surface where the solar wind ram pressure is balanced by the magnetic pressure from the Earth's magnetic field.

Moore and Delcourt (1995) generalized the concept of the magnetopause, the boundary where the solar wind plasma is in pressure equilibrium with the magnetospheric plasma. In their generalization, they defined a surface where plasma from two different sources have equal contributions. This is called the geopause. For Earth,

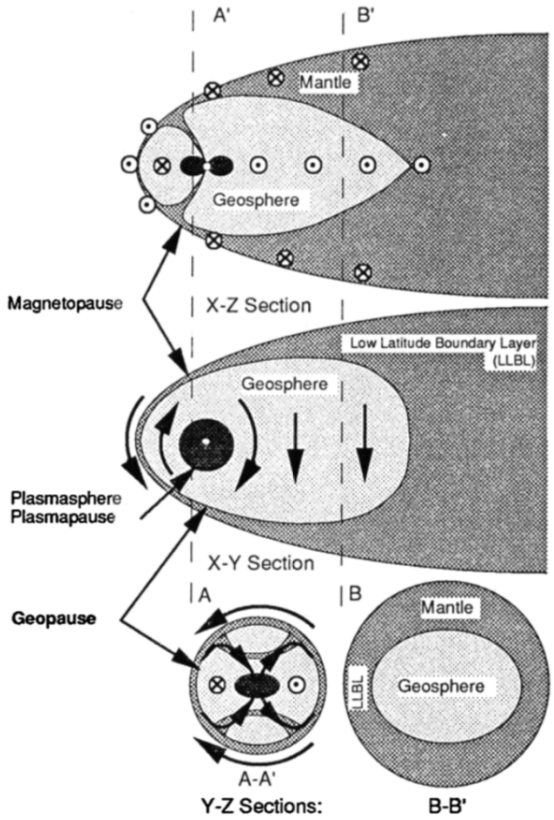

Figure 1.4: Diagram by *Moore and Delcourt* (1995) comparing the geopause to familiar magnetospheric boundaries. Top illustration shows the X-Z (meridional) plane. Middle cut shows the X-Y (equatorial) plane. The sun is on the left for both top and middle cuts. Bottom cut is the Y-Z plane looking from the Sun to the Earth. The plasma number density is indicated by the grey colors. The darker the grey, the denser the plasma density is.

the two plasma sources are the solar wind and the ionosphere. For example, the pressure geopause is defined as the surface where the solar wind thermal pressure is equal to the ionospheric thermal pressure. Such surfaces can be defined for both mass density and number density. With these geopauses, we can identify regions where the ionospheric plasma is dominant.

Moore and Delcourt developed the concept of the geopause as an analogue of the sea to air interface where the coupling between the sea and air leads to energy dissipation and the generation of storms from the disturbances occuring at that boundary. The geopause is important due to the particle and energy exchanges between the

ionospheric and heliospheric plasma and can possibly develop physical processes contributing to geomagnetic storms and substorms.

1.5 Geopause Unanswered Questions

The three questions that this thesis attempts to answer are,

1. How do the geopauses behave with respect to the magnetopause in steady state?
2. How do the geopauses behave in response to the solar wind's magnetic field reversal?
3. How do the force terms in the multifluid momentum equation relate to the geopauses?

1.5.1 Question 1: How do the geopauses behave with respect to the magnetopause in steady state?

This question was not addressed by past research. The first numerical study of geopauses in the Earth's magnetosphere by *Winglee* (1998) demonstrated through multifluid MHD that the ionosphere could be a dominant source of plasma in the magnetosphere. *Xu et al.* (2016) modeled the interaction of the solar wind with Mars and applied the notion of geopauses to suggest that planetary ions at Mars could escape at the lobes (at high latitudes). Searching the literature shows that comparisons between the magnetopause and the geopause are lacking. Thus, the first study addresses this question.

1.5.2 Question 2: How do the geopauses behave in response to the solar wind's magnetic field reversal?

There has been a dearth of research on the dynamics of geopauses. Only a few papers exist which contain different time snapshots of the morphology of the geopauses

at Earth (*Winglee*, 1998, 2000). The study emerging from this question is a natural follow up to the first study. The first study addressed the steady state behavior. The second study addresses the dynamic behavior of the geopause.

1.5.3 Question 3: How do the force terms in the multifluid momentum equation relate to the geopauses?

Numerical geopause studies are a very small subset of studies emerging from the use of multifluid MHD. While the first multifluid MHD simulation was related to the study of geopauses *Winglee* (1998), subsequent simulations (*Winglee et al.*, 2002; *Glocer et al.*, 2009a; *Brambles et al.*, 2010; *Wiltberger et al.*, 2010; *Ilie et al.*, 2013) focused on data-model comparisons to validate their codes. This study analyzes the source terms in the multifluid MHD equations and compares them to the boundaries in steady state.

1.6 Thesis Outline

In chapter 2, we introduce the equations used in simulating the magnetosphere. In chapter 3, we compare the various geopause definitions to the magnetopause in steady state. In chapter 4, we analyze the transient effects of mass density on geopause structure. In chapter 5, the geopauses are compared to the force density terms in the momentum equations. In chapter 6, we summarize the results and discuss future work.

CHAPTER II

Modeling the Magnetosphere

2.1 Magnetospheric Modeling

To obtain the multifluid equations, we start from kinetic theory. To make the derivation simpler, we will neglect collision terms. A more in depth discussion on kinetic theory can be found in *Gombosi* (1994). The number of particles of a fluid species α with a phase space distribution $f_\alpha(\mathbf{x}, \mathbf{v}, t)$ is,

$$N(\mathbf{x}, t) = \int f_\alpha(\mathbf{x}, \mathbf{v}, t) d^3v d^3x \tag{2.1}$$

The Boltzmann equation describes the evolution of the phase space distribution. In an electromagnetic field for particles with a mass m_α and charge q_α, it takes the form,

$$\frac{df_\alpha}{dt} = \frac{\partial f_\alpha}{\partial t} + \mathbf{v} \cdot \nabla_{\mathbf{x}} f_\alpha + \frac{q_\alpha}{m_\alpha}(\mathbf{E} + \mathbf{v} \times \mathbf{B}) \cdot \nabla_{\mathbf{v}} f_\alpha = 0 \tag{2.2}$$

E and **B**, are the electric and magnetic fields. They are found by using Maxwell's equations. To obtain the multifluid MHD equations, we need to take moments of the Vlasov equation. The zeroth moment of the distribution function is,

$$n_\alpha(\mathbf{x}, t) = \int f_\alpha(\mathbf{x}, \mathbf{v}, t) d^3v \tag{2.3}$$

where n_α is the number density of species α.

Taking the first moment of the distribution function yields,

$$n_\alpha(\mathbf{x},t)\mathbf{u}_\alpha(\mathbf{x},t) = \int \mathbf{v} f_\alpha(\mathbf{x},\mathbf{v},t) d^3v \tag{2.4}$$

where $\mathbf{u}_\alpha$ corresponds to the bulk velocity of species α.

The second moment of the distribution function is,

$$\mathbf{P}_\alpha(\mathbf{x},t) = m_\alpha \int \mathbf{v}\mathbf{v} f_\alpha(\mathbf{x},\mathbf{v},t) d^3v \tag{2.5}$$

where $\mathbf{P}_\alpha$ is the pressure tensor.

Integrating (2.2) through velocity space (which is taking the zeroth moment) and multiplying by the particle mass m_α, we obtain the mass continuity equation,

$$\frac{\partial \rho_\alpha}{\partial t} + \nabla \cdot (\rho_\alpha \mathbf{u}_\alpha) = 0 \tag{2.6}$$

where ρ_α is the mass density of species α and is related to the number density by $\rho_\alpha = n_\alpha m_\alpha$

Next, multiplying the Vlasov equation by the particle mass, m_α, and velocity $\mathbf{v}$ and integrating over velocity space yields the momentum equation,

$$\frac{\partial \rho_\alpha \mathbf{u}_\alpha}{\partial t} + \nabla \cdot (\rho_\alpha \mathbf{u}_\alpha \mathbf{u}_\alpha + \mathbf{P}_\alpha) = n_\alpha q_\alpha (\mathbf{E} + \mathbf{u}_\alpha \times \mathbf{B}) \tag{2.7}$$

In the context of this thesis, the pressure tensor is assumed to be isotropic because anisotropic multifluid MHD has not been implemented in the SWMF. So, the momentum equation is rewritten as,

$$\frac{\partial \rho_\alpha \mathbf{u}_\alpha}{\partial t} + \nabla \cdot (\rho_\alpha \mathbf{u}_\alpha \mathbf{u}_\alpha + p_\alpha I) = n_\alpha q_\alpha (\mathbf{E} + \mathbf{u}_\alpha \times \mathbf{B}) \tag{2.8}$$

where p_α is the isotropic pressure, and I is the unit index tensor.

We can keep on going and take higher and higher moment orders of the Vlasov equation but this procedure will never close the equations. Thus, we need a closure relation. One of the most typical assumptions regarding the plasma in the magnetosphere is that the plasma is adiabatic. Thus, we can relate the pressure and mass density of a fluid with the expression,

$$p_\alpha \rho_\alpha^{-\gamma} = C \tag{2.9}$$

where γ is the adiabatic index and C is a constant. Within this thesis, the plasma is assumed to be an ideal gas and so γ takes the value of $5/3$. To derive an equation for the pressure equation, take the total time derivative of (2.9) and use the equation of mass continuity to obtain the expression,

$$\frac{\partial p_\alpha}{\partial t} + \nabla \cdot (p_\alpha \mathbf{u}_\alpha) = -(\gamma - 1) p_\alpha \nabla \cdot \mathbf{u}_\alpha \tag{2.10}$$

The last equation needed for a magnetospheric plasma is Faraday's law of induction,

$$\frac{\partial \mathbf{B}}{\partial t} = -\nabla \times \mathbf{E} \tag{2.11}$$

Next, we use the momentum equations for the electron plasma to obtain Ohm's Law, that is to relate the electric field $\mathbf{E}$ to known quantities. The ion and electron momentum equations are,

$$\frac{\partial \rho_s \mathbf{u}_s}{\partial t} + \nabla \cdot (\rho_s \mathbf{u}_s \mathbf{u}_s + I p_s) = n_s q_s (\mathbf{E} + \mathbf{u}_s \times \mathbf{B}) \tag{2.12}$$

$$\frac{\partial \rho_e \mathbf{u}_e}{\partial t} + \nabla \cdot (\rho_e \mathbf{u}_e \mathbf{u}_e + I p_e) = -n_e q (\mathbf{E} + \mathbf{u}_e \times \mathbf{B}) \tag{2.13}$$

where q is the elementary charge, the s subscript denotes the ion species, and the

e subscript denotes the electron fluid. By comparing the ion and electron momentum equations, we can neglect the terms relating to ρ_e given that the electron mass is smaller than the species ion mass. This simplification allows us to solve for the electric field in the electron momentum equation,

$$\mathbf{E} = -\mathbf{u}_e \times \mathbf{B} - \frac{\nabla p_e}{q n_e} \tag{2.14}$$

The definition of the current density relates the ion velocities to the electron velocity,

$$\mathbf{J} = \sum_s q_s n_s \mathbf{u}_s - q n_e \mathbf{u}_e \tag{2.15}$$

The electron velocity is then,

$$\mathbf{u}_e = \mathbf{u}_+ - \frac{\mathbf{J}}{q n_e} \tag{2.16}$$

where $\mathbf{u}_+$ is defined as the charge average velocity, and takes the form,

$$\mathbf{u}_+ = \frac{\sum_s q_s n_s \mathbf{u}_s}{q n_e} \tag{2.17}$$

And so, substituting the electron velocity into the expression for the electric field (2.14) is rewritten as,

$$\mathbf{E} = -\mathbf{u}_+ \times \mathbf{B} + \frac{\mathbf{J} \times \mathbf{B}}{q n_e} - \frac{\nabla p_e}{q n_e} \tag{2.18}$$

The first term physically represents a non-relativistic transformation to a frame where the velocity is the charge averaged velocity, the second term is the Hall term, and the last term is the ambipolar electric field.

Substituting the expression for the electric field into Faraday's law then yields,

$$\frac{\partial \mathbf{B}}{\partial t} = \nabla \times \left(\mathbf{u}_+ \times \mathbf{B} - \frac{\mathbf{J} \times \mathbf{B}}{q n_e} + \frac{\nabla p_e}{q n_e} \right) \tag{2.19}$$

solving Faraday's law numerically with the additional Hall term and the ambipolar electric field is much more expensive computationally. The Hall term adds a second order spatial derivative due to Ampere's law relating the current density to the curl of the magnetic field. It is assumed that the electron pressure gradient and the electron number density gradient are in the same direction. Thus, those terms are neglected and Faraday's law is simplified to,

$$\frac{\partial \mathbf{B}}{\partial t} = \nabla \times (\mathbf{u}_+ \times \mathbf{B}) \tag{2.20}$$

The momentum equation for ions is then,

$$\frac{\partial \rho_s \mathbf{u}_s}{\partial t} + \nabla \cdot (\rho_s \mathbf{u}_s \mathbf{u}_s + I p_s) = n_s q_s (\mathbf{u_s} - \mathbf{u}_+) \times \mathbf{B} + \frac{n_s q_s}{n_e q} (\mathbf{J} \times \mathbf{B} - \nabla p_e) + S_{p_s} \tag{2.21}$$

In practice, solving the momentum equation in near Earth space requires a way to implement a friction term between the different fluid species in order to limit relative fluid velocities. *Glocer et al.* (2009a) implemented a friction term, S_{p_s}, in the momentum equation with the form,

$$S_{\rho_s \mathbf{u}_s} = \frac{1}{\tau_c} \sum_{i \neq s} \min(\rho_s, \rho_i)(\mathbf{u}_i - \mathbf{u}_s) \left(\frac{\mid \mathbf{u}_s - \mathbf{u}_i \mid}{u_c} \right)^{\alpha_c} \tag{2.22}$$

τ_c, the cutoff time scale, is set to 1000 s. $\mathbf{u}_c$, the cutoff velocity, is set to 100 km/s. α_c, the cutoff exponent, is set to 2. i is the index denoting the other ion fluids. This term is an ad-hoc friction term. These parameters are the default values used in the code for Earth simulations.

One additional question remains, what is the electron pressure gradient? One way to solve for it is to use the electron pressure equation,

$$\frac{\partial p_e}{\partial t} + \nabla \cdot (p_e \mathbf{u}_e) = -(\gamma - 1) p_e \nabla \cdot \mathbf{u}_e \tag{2.23}$$

In the Earth's magnetosphere, the electron pressure can be approximated as $p_e = 0.2 \sum p_s$ (*Glocer et al.*, 2009a). This approximation saves computational time.

Putting everything together, the equations of multifluid MHD are,

$$\frac{\partial \rho_s}{\partial t} + \nabla \cdot (\rho_s \mathbf{u}_s) = 0 \tag{2.6}$$

$$\frac{\partial \rho_s \mathbf{u}_s}{\partial t} + \nabla \cdot (\rho_s \mathbf{u}_s \mathbf{u}_s + I p_s) = n_s q_s (\mathbf{u_s} - \mathbf{u}_+) \times \mathbf{B} + \frac{n_s q_s}{n_e q} (\mathbf{J} \times \mathbf{B} - \nabla p_e) + S_{p_s} \tag{2.21}$$

$$\frac{\partial \mathbf{B}}{\partial t} = \nabla \times (\mathbf{u}_+ \times \mathbf{B}) \tag{2.20}$$

$$\frac{\partial p_s}{\partial t} + \nabla \cdot (p_s \mathbf{u}_s) = -(\gamma - 1) p_s \nabla \cdot \mathbf{u}_s \tag{2.10}$$

Alternatively, instead of using the adiabatic pressure equation, we can multiply the Vlasov equation by $0.5 m_s v_s^2$, integrate over velocity space, and use the newly obtained expression for Ohm's law to derive the equation for the evolution of the hydrodynamic energy density, $\epsilon_s = \rho_s v_s^2/2 + p_s/(\gamma - 1)$,

$$\frac{\partial \epsilon_s}{\partial t} + \nabla \cdot [(\epsilon_s + p_s)\mathbf{u}_s] = \mathbf{u}_s \cdot \left[n_s q_s (\mathbf{u_s} - \mathbf{u}_+) \times \mathbf{B} + \frac{n_s q_s}{n_e q} (\mathbf{J} \times \mathbf{B} - \nabla p_e) \right] \tag{2.24}$$

However, for terrestrial magnetospheric simulations, the ratio of thermal pressure to magnetic pressure, β, is very small very close to Earth and thus, the magnetic terms would dominate the energy equation and cause problems in the numerical solution. Thus, the pressure equation is preferred in this context.

2.2 Boundary Conditions and Magnetospheric Plasma Sources

For the Earth's magnetosphere, there are two sets of boundary conditions necessary to setup the simulations. We can specify the outer boundary conditions, with one face of the simulation domain, the solar wind conditions. The other faces of the simulation domain correspond to outflowing boundary conditions. The other set of boundary conditions are inner boundary conditions centered at 2.5 Earth radii (R_E). The inner boundary acts as a source for ionospheric plasma. This is the focus of the next section.

2.3 Ionospheric Modeling

The goal of coupling a global magnetospheric model with an ionospheric model is to find the electric potential under the current densities provided by the MHD code. The equation for charge conservation is,

$$\frac{\partial \rho_q}{\partial t} + \nabla \cdot \mathbf{J} = 0 \tag{2.25}$$

and when applied to the ionosphere, the current density is assumed to be divergence free (*Kelley*, 2009).

We can estimate the timescale for growth of an electric field if there were any large scale free charges in the ionosphere,

$$\tau \sim \frac{\rho_q}{\nabla \cdot \mathbf{J}} \sim \frac{\epsilon_0 \nabla \cdot \mathbf{E}}{\nabla \cdot \mathbf{J}} \sim \frac{\epsilon_0 E}{\sigma E} \sim \frac{\epsilon_0}{\sigma} \tag{2.26}$$

where ϵ_0 is the vacuum permittivity and σ is the electric conductance. We assumed a spatially uniform conductance and used the simplest form of Ohm's law, $\mathbf{J} = \sigma \mathbf{E}$ to perform this estimation. Choosing the smallest values of conductivity in the

ionosphere, ($\sim 10^{-5}$ mho/m), yields a timescale for growth of about 1 microsecond for any non-zero divergence in the current density (see Fig. 2.1 for reference values of conductivities found in the ionosphere). This would imply that electric fields in the ionosphere would grow at a very fast rate. Thus, the assumption that $\nabla \cdot \mathbf{J} = 0$ is justified. Alternatively, we could have justified using the divergence free condition for the current density by using the MHD approximation.

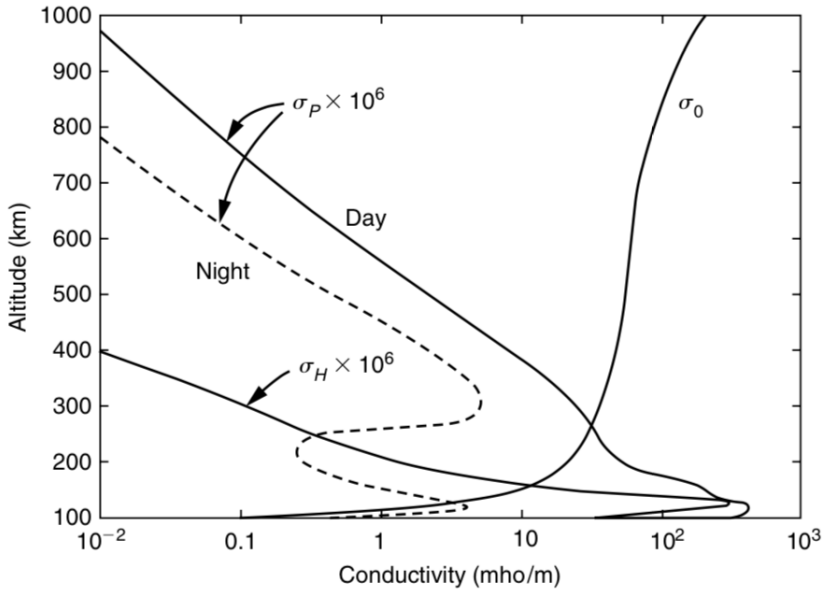

Figure 2.1: Typical conductivity values in the midlatitude daytime ionosphere (*Kelley*, 2009). The Pedersen conductivity, σ_P , and the Hall conductivity, σ_H, are scaled relative to the parallel conductivity, σ_0. The dashed line is a typical nighttime Pedersen conductivity profile.

We can use the divergence free current density to obtain the equation central to the ionospheric electrodynamics model. We expand the operator along coordinates perpendicular and parallel to the magnetic field we obtain,

$$\nabla \cdot \mathbf{J} = \nabla_\perp \cdot \mathbf{J}_\perp + \frac{\partial J_\parallel}{\partial s} = 0 \tag{2.27}$$

where $\mathbf{J}_\perp$ is the current density components perpendicular to the magnetic field and $J_\parallel$ is the current density component parallel to the magnetic field (field aligned current

density in the literature). Mathematically, they are defined as,

$$\mathbf{J}_\perp = \mathbf{J} \times \frac{\mathbf{B}}{B} = \mathbf{J} \times \hat{b} \tag{2.28}$$

and,

$$J_\parallel = \mathbf{J} \cdot \hat{b} \tag{2.29}$$

where $\hat{b}$ is the magnetic field unit vector. The field aligned current is provided by the magnetohydrodynamics code. Thus, we can use divergence free condition of the current density to integrate along the magnetic field line and obtain the expression,

$$\int_{s_1}^{s_2} \frac{\partial J_\parallel}{\partial s} ds = -\int_{s_1}^{s_2} \nabla_\perp \cdot \mathbf{J}_\perp ds \tag{2.30}$$

where s denotes the distance along the magnetic field line.

A more general form of Ohm's law applied to the ionosphere is,

$$\mathbf{J} = \boldsymbol{\sigma} \cdot \mathbf{E} \tag{2.31}$$

Then the field aligned current is,

$$J_\parallel(s_2) - J_\parallel(s_1) = -\int_{s_1}^{s_2} \nabla_\perp \cdot (\boldsymbol{\sigma} \cdot \mathbf{E}) ds \tag{2.32}$$

One of the other assumptions used in ionospheric modeling is that the electric field component parallel to the magnetic field is very small (*Vasyliūnas*, 2012). This simplifies the calculation by having the integral act only over the conductivity. Furthermore, the magnetic field in the ionosphere is assumed to vary slowly over time. Then, the electric field can be written in terms of the electric potential, ϕ, as $\mathbf{E} = -\nabla\phi$. This assumption makes sense because at the ionospheric level, the magnetic field is dominated by the Earth's intrinsic dipole field.

We place s_1 at the base of the ionosphere (50 km) and s_2 at the top of the ionosphere (about 1000 km). The field aligned current at the base of the ionosphere is 0. The field aligned current at the top of the ionosphere is provided by the MHD code. So we can simplify (2.32) as,

$$\boxed{J_{\parallel} = \nabla_{\perp} \cdot (\boldsymbol{\Sigma} \cdot \nabla\phi)} \tag{2.33}$$

where Σ is the height integrated conductivity and is mathematically defined as,

$$\Sigma = \int_{s_1}^{s_2} \boldsymbol{\sigma} ds \tag{2.34}$$

(2.33) is the equation central to the ionospheric electrodynamics model. It relates the field aligned current density to the electric potential given a conductance model.

2.4 Simulation Setup

Fig. 2.2 gives a sense of the various length scales and time scales of space physics systems in the solar system. Referring to that figure, we are studying solar wind magnetosphere interactions. At this level, the length scale examined is about 1 solar radius (which is about 100 Earth radii), and the time scale is about 1 hour. Thus, we do not need to use a simulation domain extending from the Sun to the Earth, and we do not need to use grid sizes at the scale of the ion gyroradius. We focus on large scale magnetospheric phenomena and take a global approach that doesn't focus on the microphysics of outflow, reconnection, or turbulence.

The gyrofrequency for a particle of charge q and mass m in a magnetic field $\mathbf{B}$ is,

$$\omega_c = \frac{|q|B}{m} = 9.58 \times 10^{-2} |Z| \left(\frac{B}{\mathrm{nT}}\right) \left(\frac{m}{m_p}\right)^{-1} \mathrm{s}^{-1} \tag{2.35}$$

where Z is the charge state of the particle.

The gyroradius for a particle of speed v can then be derived from the gyrofrequency. It takes the form,

$$r = \frac{v}{\omega_c} = \frac{10.4}{|Z|}\left(\frac{v}{\mathrm{km/s}}\right)\left(\frac{B}{\mathrm{nT}}\right)^{-1}\left(\frac{m}{m_p}\right)\mathrm{km} \tag{2.36}$$

The simulation code used in this thesis is the Space Weather Modeling Framework (SWMF) (*Tóth et al.*, 2012; *Gombosi et al.*, 2021). It is a software framework that links physical systems with differing length scales and timescales. It is one of the only codes capable of modeling the solar system from the corona to the heliosphere.

The need for a software framework arose from the application of the Block Adaptive Tree Solar wind Roe-type Upwind Scheme (BATS-R-US) in the Earth's magnetosphere. In its original inception, BATS-R-US solved the equations of single fluid ideal MHD (*Powell et al.*, 1999). In that study, no physics based ionospheric model was used. In another study, *Ridley et al.* (2001) coupled BATS-R-US to an empirical ionospheric model. In a more complex study, *Ridley et al.* (2003) coupled BATS-R-US to upper atmospheric models and an ionospheric model. *De Zeeuw et al.* (2004) later coupled BATS-R-US to a ring current model and an ionospheric model. In each of these instances, the codes did not allow for an arbitrary selection of models or for flexibility on parallel computers. Thus, a software interface was needed to alleviate these issues and the SWMF was born (*Tóth et al.*, 2005).

One of the original codes of the SWMF was the Block Adaptive Tree Solar wind Roe-type Upwind Scheme (BATS-R-US). In its original inception, BATS-R-US solved the equations of single fluid ideal MHD (*Powell et al.*, 1999). Later, the capabilities of BATS-R-US was extended to solve for the semi-relativistic MHD equations (*Gombosi et al.*, 2002), multispecies (all species are held to the same velocity) MHD equations (*Ma et al.*, 2002), anisotropic pressure (*Meng et al.*, 2012), Hall MHD (*Tóth et al.*, 2008), and multifluid MHD (*Glocer et al.*, 2009a). This thesis uses the multifluid MHD capabilities of BATS-R-US.

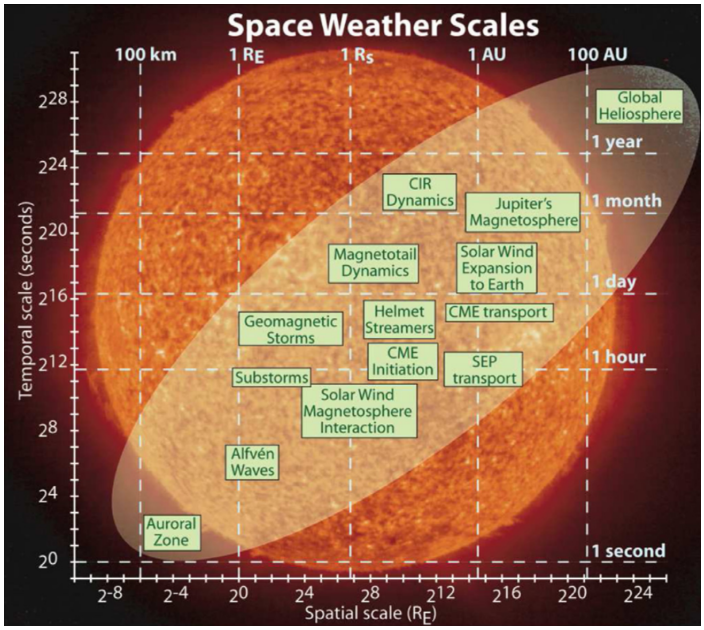

Figure 2.2: Diagram of timescales and lengthscales of various plasma systems in the solar system (*Tóth et al.*, 2012).

The conductivity models used within the Space Weather Modeling Framework for the ionospheric electrodynamics module is the Ridley Ionospheric Model (*Ridley and Liemohn*, 2002; *Ridley et al.*, 2004). The model numerically solves (2.33) for the electric potential. The model specifies the conductivity tensor. The current densities at the inner boundary of the code are mapped along the magnetic field line to the ionospheric domain. Specifically, the current density at the inner boundary ($J_{\parallel}(r = 3R_E)$) is multiplied by a factor of B_I/B_3 where B_I is the magnetic field at the base of the ionosphere, and B_3 is the magnetic field at the inner boundary at 3 Earth radii. This statement is derived from the facts that along a magnetic flux tube, the magnetic flux is constant and the current is conserved. Once the electric potential is calculated, the inner boundary velocity from the ionospheric particles can be calculated as,

$$\mathbf{v} = \frac{\mathbf{B} \times \nabla\phi}{B^2} \tag{2.37}$$

The tangential component of this velocity is what is provided to the global magnetospheric code.

The simulation domain is set to $(X, Y, Z) = [-224, 32] \times [-128, 128] \times [-128, 128]$ R_E. The single fluid Alfvén speed is,

$$v_A = \frac{B}{\sqrt{\mu_0 \rho}} = 22 \left(\frac{B}{nT} \right) \left(\frac{n}{\text{cm}^{-3}} \right)^{-1/2} \left(\frac{m}{m_p} \right)^{-1/2} \text{km/s} \tag{2.38}$$

And so, the time step taken within the simulations must be less than,

$$t = \frac{L}{v_A} \tag{2.39}$$

There are two sets of boundary conditions used in simulating the Earth's magnetospheric system. They are the inner boundary and the outer boundary. The inner boundary consists of a spherical surface centered around Earth with a radius of 2.5 R_E. The outer boundary consists of the six faces at the ends of the simulation domain.

The inner boundary acts as the reservoir for ionospheric plasma. The boundary conditions at the inner boundary are zero radial velocity for the ionospheric outflow, an inner boundary number density of 28 per cubic centimeter, and a temperature of 2.5×10^4 K. The mass density used will be dependent upon the composition of the ionosphere. Those specifics are included in Chapter 3, Chapter 4, and Chapter 5.

At the outer boundary, five of the faces at the ends of simulation domain consist of outflowing boundary conditions where the gradients for all variables are set to 0. This is an appropriate boundary condition based on the fact that the solar wind is supersonic and thus, downstream information will not propagate upstream. The other face acts as the source of solar wind. The solar wind is introduced at X = 32 R_E. The solar wind velocity is only in the X-direction with a value of -450 km/s. The mass density is 8.7 amu/cm^3. The temperature is 1.2×10^5 K. The magnetic field has a magnitude of 10 nT and is only in the z-direction. These parameters are

chosen to be constant in time in order to isolate the effects of the ionospheric outflow onto the magnetosphere.

There are two magnetic field configurations used in the simulations, south-to-north and north-to-south. In the south-to-north IMF case, the solar wind magnetic is pointed southward (negative B_z) for the first four hours of the simulation. Then, the solar wind magnetic field is reversed to a northward (positive B_z) configuration for the next 8 hours. In the north-to-south case, the opposite configuration is used, the solar wind is northward for the first 8 hours of the simulation and the next four hours the solar wind is southward.

CHAPTER III

Steady State Characteristics of the Terrestrial Geopause

3.1 Introduction

The first model of a boundary separating the solar wind plasma from the ionospheric plasma was developed by *Chapman and Ferraro* (1931). At this boundary, called the magnetopause, solar wind conditions dictate how well the solar wind interacts with the Earth's magnetosphere. During magnetic reconnection, the Dungey cycle describes how magnetic flux is transported from the dayside to the nightside magnetosphere (*Dungey*, 1961). The asymmetric reconnection rate is dependent on conditions in both the magnetospheric plasma and the solar wind (*Cassak and Shay*, 2007). The magnetospheric plasma sources include the solar wind and a non-negligible ionospheric plasma.

Shelley et al. (1972) observed energetic fluxes of heavy ions in the inner magnetosphere exceeding proton fluxes in the keV range during a geomagnetic storm. *Sharp et al.* (1982) used ISEE 1 data collected in the plasma sheet to show that the ionosphere was a dominant source to the plasma sheet during active periods. *Young et al.* (1982) used 48 months of ESA-GEOS 1 data to demonstrate enhanced O^+ density in the magnetosphere during geomagnetic activity. *Chappell et al.* (1987) concluded

that ionospheric outflows were large enough to account for observed magnetospheric plasma densities without the need for a solar wind.

With mounting evidence that the ionosphere was an important source of ions to the magnetosphere, *Moore and Delcourt* (1995) developed the concept of a geopause to help describe magnetospheric regions. The geopause is a surface defined by equal contributions of the solar wind to the ionospheric plasma. For example, the mass density geopause is the surface defined by the mass density of the solar wind equal to the mass density of the ionospheric plasma. The most well known example of a geopause is the magnetopause.

However, the geopause is difficult to study directly with satellite data due to the presence of hydrogen ions in both the solar wind and the ionospheric plasma. Indirectly, *Moore et al.* (1999) used Polar data to show an increase in ionospheric plasma number density in response to a coronal mass ejection (CME). This implied that the density geopause was displaced due to the CME compression. *Chandler and Moore* (2003) also used Polar data to demonstrate the presence of plasmaspheric ions near the equatorial magnetopause region. This showed indirectly the presence of the dayside number density geopause. Fortunately, simulations circumvent this issue by tracking solar wind plasma and ionospheric plasma separately. *Winglee* (1998) used a numerical two fluid magnetohydrodynamics (MHD) model to track solar wind hydrogen and ionospheric hydrogen. During northward inteplanetary magnetic field (IMF), the geopause was confined to the inner magnetosphere. During southward IMF, the geopause expanded into the nightside covering the near-Earth neutral line. The simulations showed that ionospheric plasma was an important source to the current sheet.

In reality, the ionospheric outflow is not only composed of hydrogen but also by oxygen (*Shelley et al.*, 1972; *Sharp et al.*, 1982; *Young et al.*, 1982) and possibly nitrogen (*Ilie and Liemohn*, 2016). *Winglee* (2000) corrected this issue by expanding

the multifluid MHD (MF-MHD) model to include O^+ along with the solar wind H^+ and ionospheric H^+ in the plasma. They used the same 3-fluid model to quantitatively demonstrate that the mass loading of the ionospheric outflow diminished the cross polar cap potential by providing a momentum loss source term to the solar wind. *Glocer et al.* (2009a), *Wiltberger et al.* (2010), *Ilie et al.* (2013) have used MF-MHD (with only 2 fluids, H^+ and O^+) simulations to investigate the effects of ionospheric outflow from O^+ on the magnetosphere. They also showed a reduction in the cross polar cap potential.

Xu et al. (2016) applied the concept of geopause to study composition boundaries at Mars. This study was the first time the concept of the "geopause" was quantitatively applied to another planet. They concluded that the magnetic lobes are dominated by ions from Mars. This implied that ion escape could occur not only at the plasma sheet but at the lobes.

So far, studies comparing the geopauses and magnetopauses have not been conducted. In fact, essentially missing in most of these studies is a direct comparison of the various definitions of geopause. While the structure and dynamics of the magnetopause are often discussed, the plasma geopauses defined by *Moore and Delcourt* (1995) have not been placed into context relative to the magnetopause. This study addresses this issue with a systematic numerical study of four different geopause definitions, using a multifluid magnetohydrodynamic model within a coupled modeling framework. This study focuses on the static configurations of these geopause locations rather their dynamics. We apply several different inner boundary condition specifications as well as two standard interplanetary magnetic field (IMF) cases, purely northward and purely southward.

3.2 Methods

We employ the Space Weather Modeling Framework (*Tóth et al.*, 2012) to simulate the magnetospheric system. The Space Weather Modeling Framework (SWMF) is a modular software framework capable of linking different models to simulate the system reliably and efficiently. It has been used to successfully model processes in Earth's magnetosphere, such as storm dynamics (*Tóth et al.*, 2007; *Zhang et al.*, 2007; *Ilie et al.*, 2010b,a, 2013; *Meng et al.*, 2012, 2013); solar wind mass and energy coupling to the magnetosphere (*Ridley*, 2007; *Yu and Ridley*, 2009; *Ilie et al.*, 2010b,a, 2013; *Welling and Ridley*, 2010); and ionosphere coupling with the magnetosphere (*Zhang et al.*, 2007; *Glocer et al.*, 2009a; *Ilie et al.*, 2015b,a). The SWMF has also been systematically validated through several community-wide "challenges" (*Pulkkinen et al.*, 2010, 2011, 2013; *Rastätter et al.*, 2011, 2013; *Shim et al.*, 2012) and even monthlong simulations (*Haiducek et al.*, 2017) and multiyear real-time nowcasting validation (*Liemohn et al.*, 2018). Therefore, even though no data-model comparisons are made in this study, the results from the SWMF have been shown to be realistic, and therefore the systematic trends to be highlighted below are robust. For this endeavor, the two systems coupled are the global magnetosphere and the ionosphere. The ionospheric electrostatic potential model used is the Ridley Ionosphere Model (RIM) (*Ridley and Liemohn*, 2002; *Ridley et al.*, 2004), which solves for the 2D height integrated potential of the ionosphere. RIM passes information about the potential to the global magnetosphere model while the global magnetosphere model provides field aligned current information to RIM. RIM uses a conductance model that includes solar EUV, starlight, and polar cap conductance.

3.2.1 Global Magnetosphere Modeling

The magnetospheric plasma has a solar wind component and an ionospheric component. To capture the physics of a multi component plasma, we use multifluid magnetohydrodynamics (MF-MHD). Within the SWMF, the Block-Adaptive-Tree Solar wind Roe-type Upwind Scheme (*Powell et al.*, 1999) models MF-MHD and enables the tracking of individual plasma pressures, mass densities, and velocities. For the simulations presented in this study, we use either a two or three fluid plasma for our simulations. The solar wind plasma is always modeled using H^+. The ionospheric plasma is modeled using either H^+ or O^+, or both. A summary of the different plasma compositions used can be found in Table 3.1. For the runs where H^+ is present in both the ionospheric plasma and the solar wind plasma, H^+ is distinguished by its source. The equations of multifluid MHD are:

$$\frac{\partial \rho_s}{\partial t} + \nabla \cdot (\rho_s \mathbf{u}_s) = S_{\rho_s}, \tag{3.1}$$

$$\frac{\partial \rho_s \mathbf{u}_s}{\partial t} + \nabla \cdot (\rho_s \mathbf{u}_s \mathbf{u}_s + I p_s) = n_s q_s (\mathbf{u_s} - \mathbf{u}_+) \times \mathbf{B} + \frac{n_s q_s}{n_e e} (\mathbf{J} \times \mathbf{B} - \nabla p_e) + S_{\rho_s \mathbf{u}_s}, \tag{3.2}$$

$$\frac{\partial p_s}{\partial t} + \nabla \cdot (p_s \mathbf{u}_s) = -(\gamma - 1) p_s \nabla \cdot \mathbf{u_s} + S_{p_s}, \tag{3.3}$$

$$\frac{\partial \mathbf{B}}{\partial t} - \nabla \times (\mathbf{u}_+ \times \mathbf{B}) = 0, \tag{3.4}$$

Equation 1 is the mass equation, equation 2 is the momentum equation, equation 3 is the pressure equation, and equation 4 is Faraday's law. ρ_s, n_s, $\mathbf{u}_s$, q_s, and p_s, denote the mass density, number density, velocity, charge and pressure of the ion species. n_e denotes the number density of the electron plasma. e is the elementary charge. p_e is the electron gas pressure. It is taken to be 0.2 times the total ion pressure (*Glocer et al.*, 2009a). I is the unit dyadic tensor. γ is the adiabatic index and takes the value of 5/3. $\mathbf{u}_+$ is the all-species averaged velocity defined as,

$$\mathbf{u}_+ = \frac{\Sigma_s q_s n_s \mathbf{u_s}}{e n_e} \tag{3.5}$$

S_{ρ_s}, $S_{\rho_s \mathbf{u}_s}$, and S_{p_s} are the source terms for the mass, momentum, and pressure ion equations. For Earth magnetospheric simulations, the mass and pressure source terms are neglected. We assume a collisionless plasma and neglect mass and pressure source terms as well as chemical reactions. However, the momentum source term cannot be neglected. The two stream instability limits the relative velocity between ion fluids parallel to the magnetic field. This instability cannot be resolved directly with our grid resolution. We use the artificial friction source term introduced by *Glocer et al.* (2009a) to keep the relative velocity between ion fluids to realistic values. The momentum source term takes the form,

$$S_{\rho_s \mathbf{u}_s} = \frac{1}{\tau_c} \sum_{i \neq s} \min(\rho_s, \rho_i)(\mathbf{u}_i - \mathbf{u}_s) \left(\frac{\mid \mathbf{u}_s - \mathbf{u}_i \mid}{u_c} \right)^{\alpha_c} \tag{3.6}$$

τ_c, the cutoff time scale, is set to 1000 s. $\mathbf{u}_c$, the cutoff velocity, is set to 100 km/s. α_c, the cutoff exponent, is set to 2. i is the index denoting the other ion fluids.

For more details on the derivation of the multifluid MHD equations see *Glocer et al.* (2009a). The coordinate system used is Geocentric Solar Magnetospheric (GSM). The simulation domain is $(X, Y, Z) = [-224, 32] \times [-128, 128] \times [-128, 128]$. The simulation time is set to 12 hours. Due to the idealized nature of this study, the Earth's rotation axis and magnetic dipole are aligned along the Z-axis.

3.2.1.1 Outer Boundary Conditions

The solar wind is introduced at the outer boundary of the system (X = 32 R_E). For the simulations presented in this study, we use two types of solar wind magnetic field conditions. For all runs, the solar wind velocity, magnetic field intensity, mass density and temperature are constant. The velocity of the solar wind is only in the

X-direction with a value of -450 km/s. The mass density of the solar wind is 8.7 amu/cm^3. The temperature is set to 1.2×10^5 K. The magnetic field polarity is reversed at a set time. In the south-to-north IMF case, the solar wind has its IMF B_z component of +10 nT and at 8:00 UT, the solar wind reverses to -10 nT and the simulation continues for 4 hours. In the north-to-south case, the solar wind has its IMF B_z component set to -10 nT for the first 4 hours of the simulation, then at 4:00 UT, the solar wind's IMF reverses to +10 nT for the next 8 hours. This solar wind configuration studied is the same as that used by previous studies (*Welling and Ridley*, 2010; *Liemohn and Welling*, 2016). Note that only the results at the end of the 12-hour simulation will be shown and discussed below. That is, this study focuses on the static structure of the various geopause locations, rather the dynamics of these boundaries (that will be the focus of a follow-on study).

3.2.1.2 Inner Boundary Conditions

The inner boundary is the source of ionospheric plasma in our simulations. It is a diffusive boundary set at a geocentric radius of 2.5 R_E. For this study, we treat four different inner boundary conditions corresponding to different ionospheric plasma compositions. The inner boundary conditions are presented in Table 3.1.

Welling and Liemohn (2014) have discussed the use of steady state boundary conditions in numerical simulations. Specifically, they examined the use of an inner boundary density specification with no assigned outflow velocity, allowing the forces within the MHD model to drive the outflow. While these types of outflows are not physically self-consistent, they can reproduce large scale structures.

3.3 Results

We present meridional (X-Z plane, Y = 0) and equatorial (X-Y plane, Z = 0) cuts of the geopause at 12:00 UT. To determine the geopause location, we cycle through

	Case 1	Case 2	Case 3	Case 4
# of fluids	2	2	3	3
MHD fluids	Sw H^+ Io H^+	Sw H^+ Io O^+	Sw H^+ Io H^+ Io O^+	Sw H^+ Io H^+ Io O^+
% Composition by Number	100 % Io H^+	100 % Io O^+	50 % Io H^+ 50 % Io O^+	94 % Io H^+ 6 % O^+
Total Number Density [/cm^3]	28	28	28	14.875
Total Mass Density [amu/cm^3]	28	448	240	28
Temperature of all ions [10^4 K]	2.5	2.5	2.5	2.5

Table 3.1: Inner Boundary Conditions. Sw is short for solar wind and Io is short for ionospheric.

each cell, calculating the ratio of the solar wind quantity to the total plasma quantity at the cell vertices. The cells must encapsulate the value 0.5, the ratio at which the contributions from the solar wind and the ionospheric plasmas are equal. Then, we perform a linear interpolation along the cell edges to mark the coordinates of the geopause. The magnetopause is defined by the last closed magnetic field line (*Song et al.*, 1999; *Siscoe et al.*, 2001). It is found by drawing iteratively field lines along the Sun-Earth line. The definition of the magnetopause used in this paper differs from the classical definition which relies on identifying regions in the magnetosphere with large currents. Identification of the magnetopause using the classical definition is unreliable in cases where the incoming solar wind is northward.

3.3.1 Geopause comparisons from outflow

Fig. 3.1 shows the number density geopause for the different IMF configurations at 12:00 UT. For northward IMF (Fig. 3.1(a) and (c)), the number density geopauses across all outflow conditions are similar. In the meridional plane, the geopauses have a lobe structure. In the southward IMF case (Fig. 3.1(b) and (d)), the number density geopause projections in the meridional and equatorial plane have a larger

cross sectional area with increasing oxygen content at the inner boundary for the cases with identical number densities (black, red, and blue lines). When comparing the inner boundaries with equal mass densities (green and black lines), the number density geopause has a larger projected area with the inner boundary with a higher particle content.

The mass density geopauses are displayed in Fig. 3.2. The northward IMF cases (Fig. 3.2(a) and (c)) show an ordering by the mass density of the ionospheric outflow. In the dayside, the outflows with significant portions of oxygen ions (blue and red lines) have a structure that is $\sim$2 R_E further sunward of the lighter outflow cases. In the nightside, the mass density geopauses extend more antisunward, with increasing mass densities at the inner boundary. Unlike the equatorial number density geopauses, the equatorial mass density geopauses do not share the same structure. The equatorial mass densities display an asymmetry across the X-axis. This asymmetry grows with increasing oxygen content at the inner boundary. The southward IMF cases (Fig. 3.2(b) and (d)) have a projected surface area in the meridional and equatorial plane that increases with respect to the mass density at the inner boundary. Similar to the northward IMF case, the dayside mass density geopause is further along the Sun-Earth line with increasing oxygen content in the outflow.

Fig. 3.3 shows the pressure geopause locations for the 4 outflow cases. The pressure geopauses for northward IMF (Fig. 3.3(a) and (c)) are not very extensive. In the meridional plane, there is a very small lobe structure associated with the outflows with oxygen (red and blue lines). In the equatorial plane, the pressure geopauses are at the simulation inner boundary. In the southward IMF case (Fig. 3.3(b) and (d)), the pressure geopause size increases with increasing inner boundary mass density. The two cases with mostly O^+ outflow have extremely long pressure geopause tails, extending past the end of the plot at -60 R_E and, in fact, going to $\sim$ -145 R_E for the 50:50 hydrogen-oxygen mix at the inner boundary and to $\sim$ -165 R_E downstream of

Earth for the pure oxygen inner boundary. Note however, that the pressure geopause does not extend into the dayside equatorial magnetosphere. For both northward and southward IMF, this is a region for which the plasma pressure is dominated by solar wind origin particles.

For comparison, let us now consider the last closed field line for the 4 boundary density cases and IMF settings. The magnetopause structures of the different outflow cases are very similar for northward IMF (Fig. 3.4(a)). In the dayside, the magnetopauses overlap along the Sun-Earth line. In the nightside, the magnetopauses of the heavier outflow cases are $\sim$2 R_E closer to Earth than the lighter cases. Similar to the northward IMF case, the dayside magnetopause for the southward IMF case is nearly the same for all types of outflow used in this study (Fig. 3.4(b)). However, the nightside magnetopause structure is larger for the lighter outflow cases (green and black lines) than the heavier outflow cases (red and blue lines). The magnetopause formed by the lighter cases are separated by $\sim$10 R_E from the heavier cases.

3.3.2 Comparisons between the geopauses and last closed field line

In the previous subsection, we have analyzed the influence of inner boundary conditions on the individual geopause definitions. Now, we are comparing the 4 geopauses for a given inner boundary case.

Fig. 3.5 presents the 4 geopause boundaries for Case 1 (solar wind H^+ and ionospheric H^+), with only ionospheric H^+ set at the inner simulation boundary. For this case, the outflowing particles are all protons, so the number density of the ionospheric origin plasma is identical to its mass density. Therefore, these two geopauses are identical and only the mass density curve is visible in the plots. In the northward IMF case, the magnetopause extends the farthest out from the planet, with the density geopauses next and the pressure geopause at the simulation inner boundary. The ordering is completely different for the southward IMF case, especially on the

nightside, where the density geopauses extend the farthest, followed by the pressure geopause, and finally the last closed field line closest to the Earth. On the dayside, the magnetopause still extends the farthest, just beyond the density geopause.

At the other extreme outflow case where O^+ is the sole ionospheric species (Case 2), Fig. 3.6 displays the 4 geopause boundaries. For northward IMF, the shape and size of the magnetopause and number density geopause are similar to Case 1. The pressure geopause is still confined to the inner boundary but has a very small lobe structure. On the nightside, the mass density geopause is the largest structure. The ordering by extent along the Sun-Earth line is mass density geopause, magnetopause, number density geopause and pressure geopause. In contrast for the dayside, the magnetopause is the largest, followed by the mass density geopause, number density geopause, then the pressure geopause. For southward IMF, the ordering for longest reach in the nightside is the pressure geopause, the mass density geopause, the number density geopause, and the magnetopause. At the dayside, the ordering is still the same as it was for northward IMF, magnetopause, mass density geopause, number density geopause, and pressure geopause.

For a 50:50 H^+ to O^+ outflow composition (Case 3), the composition boundaries show an intermediate picture for the mass density geopause in northward IMF (Fig. 3.7). That is, the size and shape of the mass density geopause is between both Case 1 and Case 2. The pressure geopause has a smaller lobe structure compared to Case 2. In the nightside, the geopause structure reaching the farthest is the magnetopause, followed by the mass density geopause, number density geopause, and pressure geopause. In the dayside, the ordering by largest extent is the magnetopause, mass density geopause, number density geopause, and the pressure geopause. For southward IMF, the geopause ordering structure by largest extent is the pressure geopause, mass density geopause, number density geopause, and magnetopause. For northward IMF, in this case the ordering by largest extent is magnetopause, mass

density geopause, number density geopause, and pressure geopause.

Figure 3.8 plots the 4 boundaries for both IMF configurations. For northward IMF, the magnetopause is once again the most dominant in the dayside and nightside structure, followed by the mass density geopause, number density geopause and pressure geopause. For southward IMF, the nightside structure most dominant is the mass density geopause followed by the number density geopause, magnetopause, and pressure geopause. The dayside structure most dominant is the magnetopause, then the mass density geopause, number density geopause, and pressure geopause.

For northward IMF, the most dominant boundary in size is the magnetopause (Fig. 3.5(a), 3.6(a), 3.7(a), 3.8(a)) with the number density and pressure geopauses that are confined close to Earth. However, the outflows with significant amounts of oxygen have a mass density geopause structure comparable in size to the magnetopause. For southward IMF, while the magnetopause dominates the dayside (Fig. 3.5(a), 3.6(a), 3.7(a), 3.8(a)), the other geopauses are much larger in cross sectional area in the nightside with increasing outflow mass density.

3.4 Discussion

This study shows that the region of dominance by Earth-origin plasma or magnetic field can be significantly different depending on both the composition of the outflowing ions and the direction of the IMF. These differences in geopause extent matter because of how these parameters (number density, mass density, plasma pressure, and magnetic field) influence the physics of forces and flows in near-Earth space. In particular, these parameters appear in specific places within the MHD equations. Let us consider how each of the four parameters appears in equations 1 through 6 above. Number density, n_s, appears twice in the momentum equation as well as in the species-averaged velocity, $\mathbf{u}_+$. This means that number density plays a critical role in the magnetic induction equation. Mass density, ρ_s, not only appears throughout

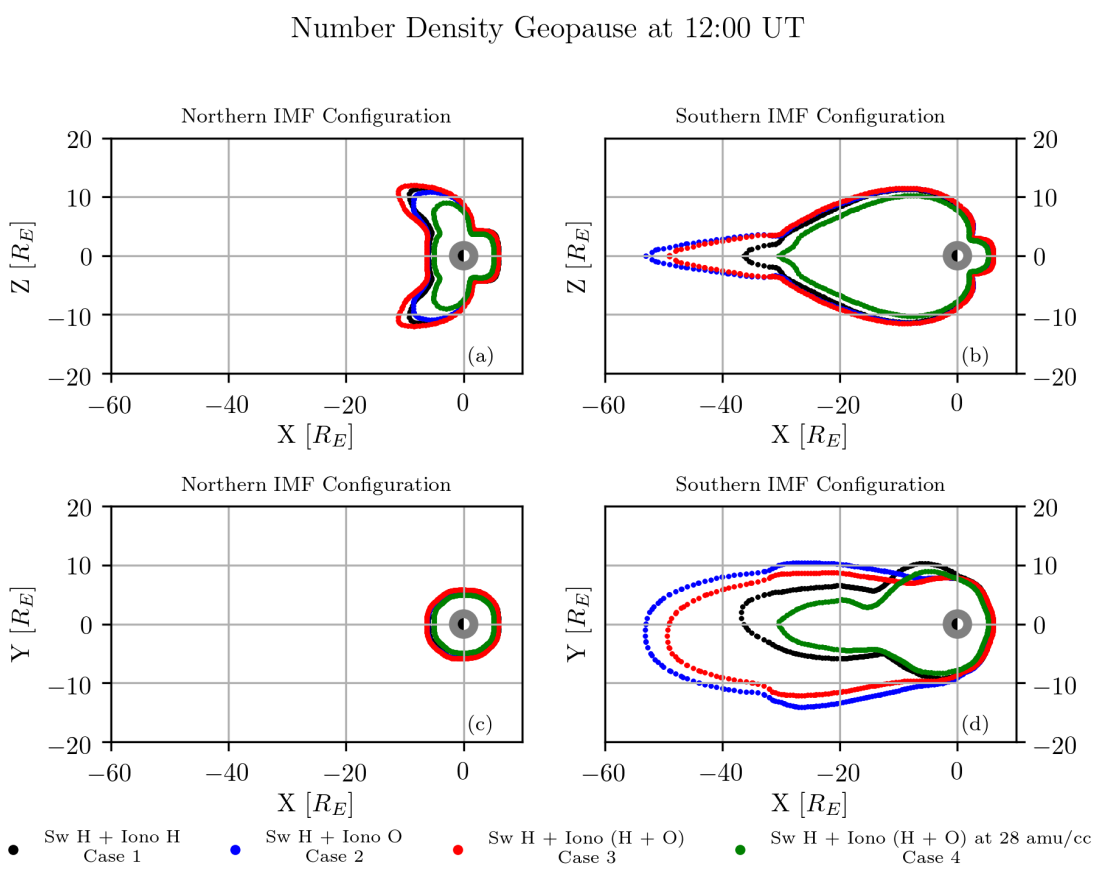

Figure 3.1: Number density geopause (a) Top left, meridional cut for northward IMF. (b) Top right, meridional cut for southward IMF. (c) Bottom left, equatorial cut for northward IMF. (d) Bottom left, equatorial cut for southward IMF.

the continuity equation but also in the momentum equation and as a multiplier in the momentum source term. Its key role in $S_{\rho_s \mathbf{u}_s}$ means that it modulates friction between the species. Plasma pressure, p_s, is ubiquitous in the pressure equation, of course, but also appears in the momentum equation through the electron pressure, p_e ($p_e = 0.2 \sum_s p_s$). Furthermore, it combines with magnetic energy for conservation of energy calculations, therefore influencing energy transport. Finally, magnetic field, B, appears not only twice in the induction equation but also twice in the momentum equation, taking part in the flow of plasma through the system. In summary, it is seen that each term in the MHD equations is influenced by one or more of the parameters

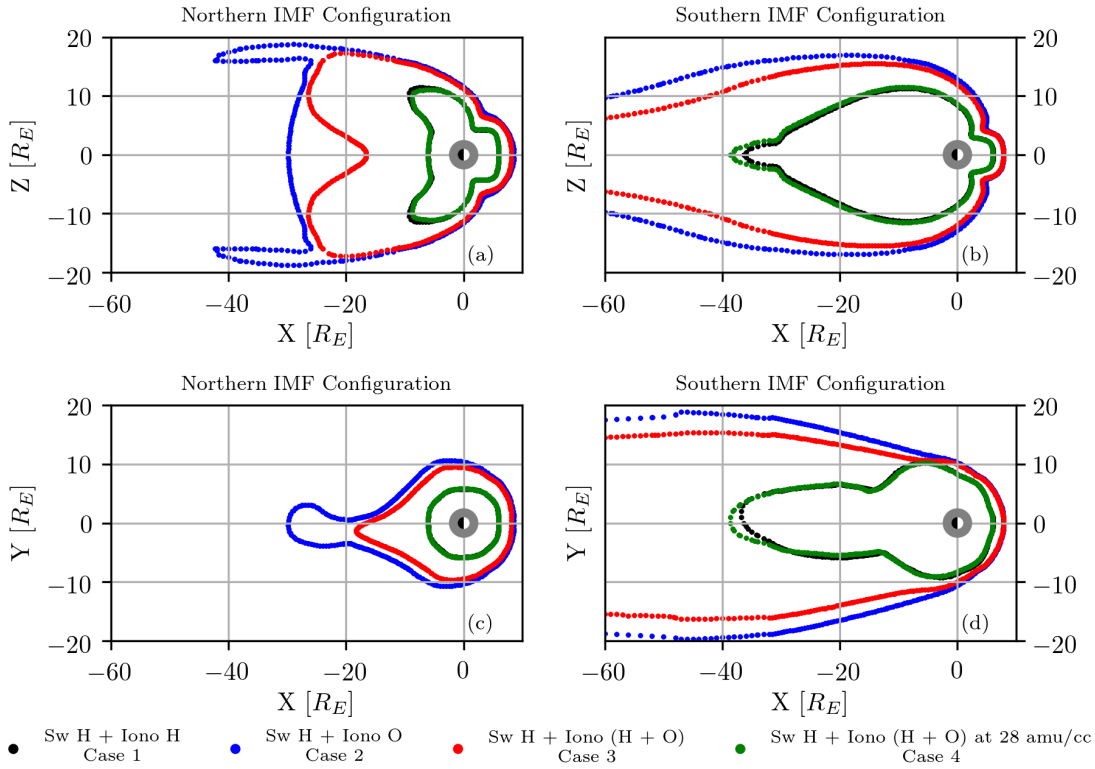

Figure 3.2: Mass density geopause (a) Top left, meridional cut for northward IMF. (b) Top right, meridional cut for southward IMF. (c) Bottom left, equatorial cut for northward IMF. (d) Bottom left, equatorial cut for southward IMF.

we have examined in our geopause results presented above.

Determining which geopause is the most important depends on the magnitudes of these terms within the MHD equations. We will not go into a detailed examination of this here because this study focused on idealized simulations. It is left to a later study to consider real-event intervals and the importance of a particular geopause location relative to another. One conclusion that can be drawn for now, however, is that there is no single surface in near-Earth space at which the physics switches from being governed by the Sun to being governed by the Earth. The differences in the geopauses presented above reveal that there is a transition from solar to Earth dominance in

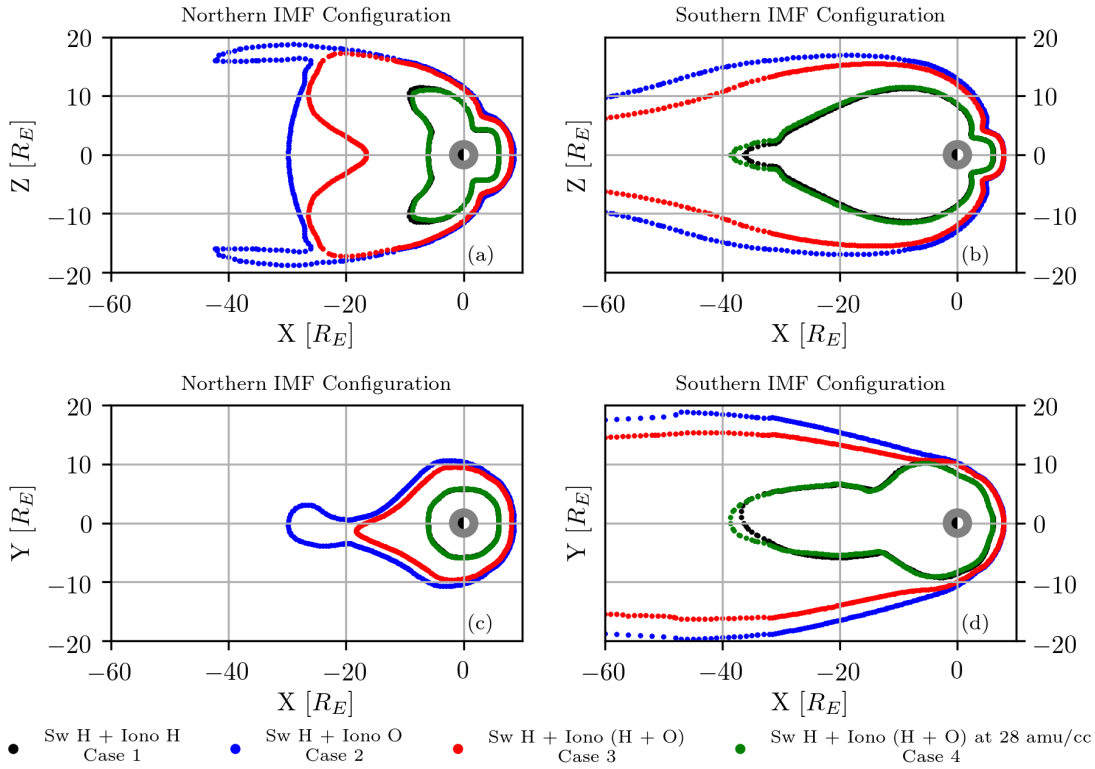

Figure 3.3: Pressure geopause (a) Top left, meridional cut for northward IMF. (b) Top right, meridional cut for southward IMF. (c) Bottom left, equatorial cut for northward IMF. (d) Bottom left, equatorial cut for southward IMF.

the physics of geospace. The magnetopause, often considered the outer boundary of Earth's influence in the solar system, is just one such boundary delineating a switch in Sun-Earth dominance of the physics. For northward IMF, this boundary is typically the farthest from the Earth, but for southward IMF, this boundary is typically the closest to the Earth.

Now let us consider the physics governing the shape of the boundaries. Within the momentum equation, a multiplier factor, $n_s q_s/(n_e e)$, is attached to the $\mathbf{J} \times \mathbf{B}$ and ∇p_e terms. For the simulations, this multiplier factor is simplified to n_s/n_e. Due to quasineutrality, the electron number density is equal to the total magnetospheric

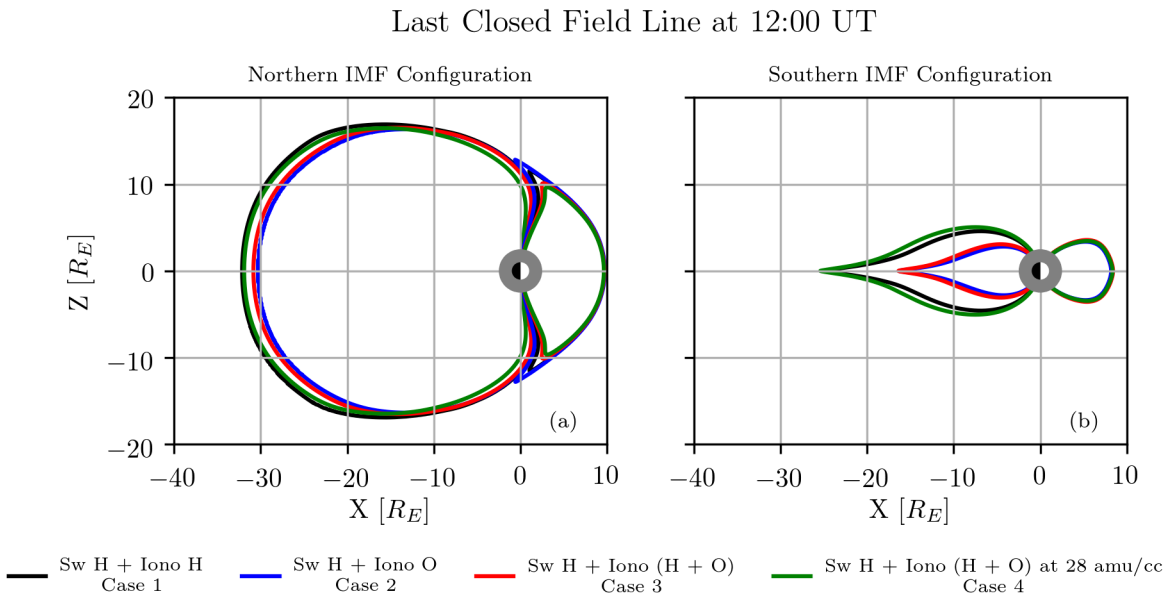

Figure 3.4: (a) Left, magnetopause projection in the meridional plane when the IMF is northward. (b) Right, magnetopause projection in the meridional plane when the IMF is southward.

plasma number density. By applying the momentum equation to the solar wind, the multiplier factor at values of 0.5 becomes the density geopause. The shape and size of the density geopause is sensitive to the difference between the $\mathbf{J} \times \mathbf{B}$ and ∇p_e. During southward IMF, the gradient of the electron pressure increases at high latitudes due to the increased convection associated with the ionospheric species. This in turn causes the density geopause to be pushed out in the nightside and expand. In the dayside, the density geopause reduces in size due to the increased solar wind access through magnetic reconnection. For northward IMF, the reduction in magnetic convection will cause a greater influence from the solar wind in the nightside magnetosphere. This results in the number density geopause to shrink in size. Since the mass density and pressure of the plasma species are related to the number densities of the plasma species, the mass density and pressure geopauses display similar behavior compared to the number density geopause. That is, the geopauses reduce in size during northward

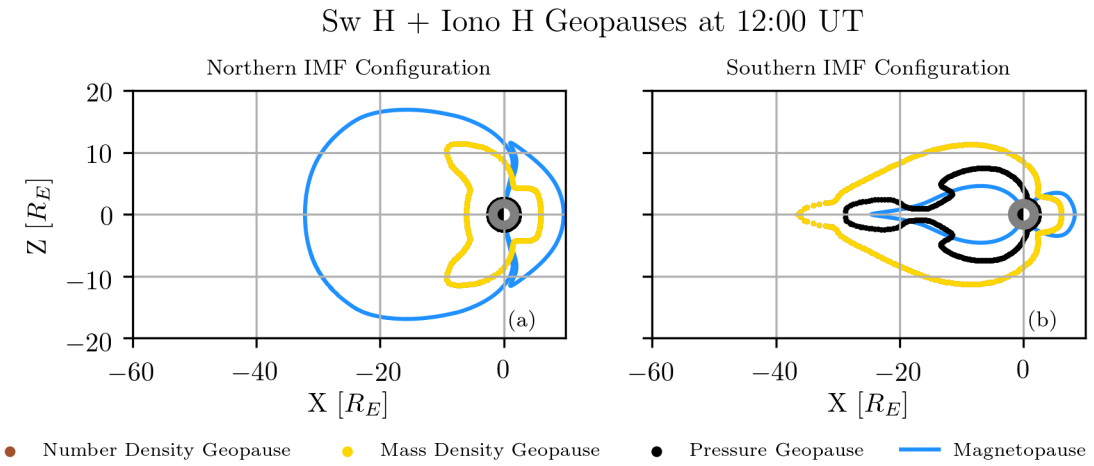

Figure 3.5: Geopauses for a plasma composed of solar wind and ionospheric hydrogen in the meridional plane. (a) Left, northward IMF. (b) Right, southward IMF. Note that the mass density geopause and the number density geopause are identical.

IMF and increases in size during southward IMF.

During northward IMF, the magnetopause responds poorly to the inner boundary mass density. This can be attributed to the lack of magnetic flux transport due to reconnection from the dayside to the nightside. The nightside differences in the magnetopause are due to high latitude reconnection. During southward IMF, the dayside magnetopause locations between the different outflows are nearly identical. The different number density geopauses and pressure geopauses show that the solar wind dominates the magnetopause. Thus, ionospheric plasma plays a small part in dayside magnetic reconnection. Unlike the dayside magnetopause, the nightside magnetopause has shown some sensitivity to the composition of the inner boundary. Since the nightside magnetopause is contained within the number density geopause, the ionospheric plasma takes a greater part in the reconnection process compared to the dayside. For both IMF configurations, the confinement of the dayside pressure geopause to the inner boundary indicates the inability of MHD forces to enable outflow

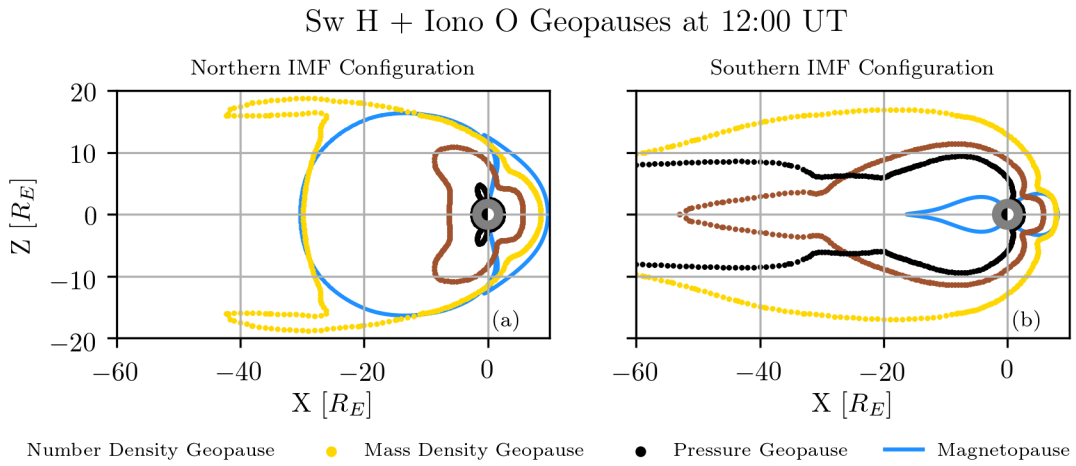

Figure 3.6: Geopauses for a plasma composed of solar wind hydrogen and ionospheric oxygen in the meridional plane. (a) Left, northward IMF. (b) Right, southward IMF.

of ionospheric ions at lower latitudes. One explanation might be because of to the lack of a causal outflow model. The other explanation is due to the absence of an inner magnetosphere model that includes drift physics. Our simulations have not included a ring current model. Simulations that coupled ring current models to global MHD models have shown an increase in pressure by an order of magnitude at the inner magnetosphere compared to pure magnetospheric MHD runs (*De Zeeuw et al.*, 2004; *Pembroke et al.*, 2012; *Glocer et al.*, 2013; *Welling et al.*, 2018). Including an inner magnetosphere model will push the dayside pressure geopause further out of the inner boundary. However, the ring current models currently available in the SWMF do not distinguish the hydrogen plasma by its solar wind and ionospheric sources. This issue will be addressed in a future study by coupling BATS-R-US to the Hot Electron Ion Drift Integrator (HEIDI) ring current model (*Ilie et al.*, 2012). With the coupling of HEIDI, we expect an expansion in size of the pressure geopause. One unanswered question relating to this study is: Where do the gyration, body forces, and friction terms in the momentum equations become prominent? This issue will be addressed

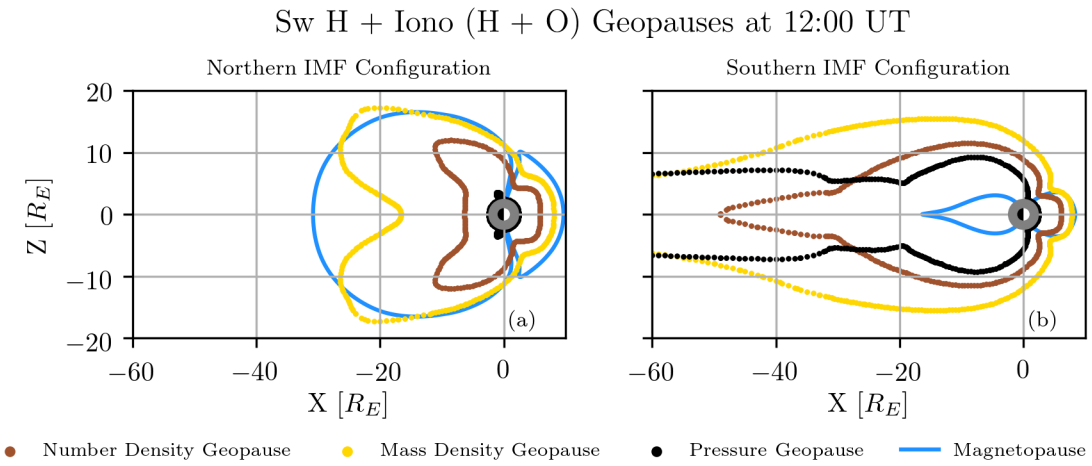

Figure 3.7: Geopauses for a plasma composed of solar wind hydrogen, ionospheric hydrogen and oxygen in the meridional plane. (a) Left, northward IMF. (b) Right, southward IMF.

in a future study analyzing the contribution of each term in the simulation region.

3.5 Summary and Conclusions

We have performed multifluid MHD simulations where the ionospheric plasma was distinguished from the solar wind plasma. In these simulations, we used a passive inner boundary in which we maintained the same number density and varied the amount of oxygen. For the sake of comparison, we also used an inner boundary composition with oxygen with mass densities similar to a solely hydrogen plasma. We used two different solar wind conditions where the solar wind mass density, velocity, temperature and magnetic field intensity were the same, but the polarities were different.

Our results indicate that the geopause structures formed during steady state was dependent on the abundance of oxygen ions in the ionospheric outflow during southward IMF. For northward IMF, only the mass density geopause varied with the inner

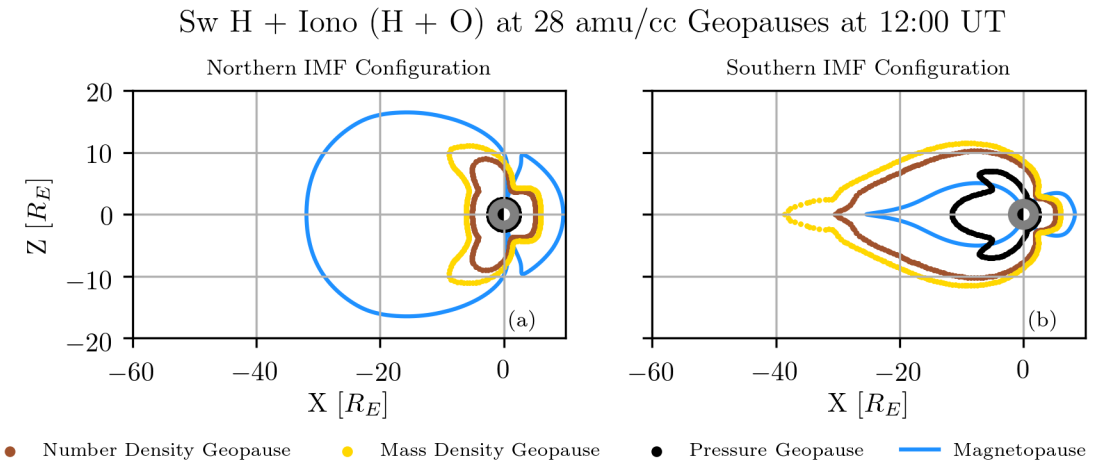

Figure 3.8: Geopauses for a plasma composed of solar wind hydrogen, ionospheric hydrogen and oxygen in the meridional plane for an inner boundary mass density of 28 amu/cm^3. (a) Left, northward IMF. (b) Right, southward IMF.

boundary conditions. For the magnetopause in both IMF configurations, the dayside magnetopause did not vary between the different simulated ionospheric outflow cases. However, the nightside magnetopause was sensitive to the presence of oxygen ions present in the ionospheric outflow. In the north IMF case, a significant presence of oxygen in the outflow brings the nightside magnetopause further in along the Sun-Earth line by a few Earth radii compared to the oxygen poor outflow cases. In the south IMF case, the nightside magnetopause along the Sun-Earth line is about 10 Earth radii further in for the oxygen rich outflow simulations, compared to the oxygen poor outflow simulations.

Within each set of simulations, we have seen that for northward IMF, the magnetopause was the largest structure in both the dayside and the nightside. This indicates that the solar wind dominated the magnetopause. For southward IMF, while the magnetopause still is the largest structure in the dayside, the geopauses in the nightside are comparable if not larger than the magnetopause. This indicates that

ionospheric plasma can dominate in regions outside of the nightside magnetopause.

We have discussed the ramifications of the differences in these geopause locations which imply that the physics governing near-Earth space does not have a single surface at which the governing processes switch from solar wind dominance to ionospheric dominance. Instead, there is a gradual transition as a set of physical processes associated with each parameter (number density, mass density, plasma pressure, and magnetic field) switch at different surfaces. The location of these surfaces strongly depend on both of the controlling factors considered in this study: the composition of the outflowing particles and the orientation of the IMF.

CHAPTER IV

Transient Characteristics of the Terrestrial Geopause

4.1 Introduction

Shelley et al. (1972) detected energetic heavy ion fluxes corresponding to oxygen in the inner magnetosphere during active times. This suggested that the ionosphere was a significant source of plasma to the magnetosphere. Studies by *Sharp et al.* (1982), *Young et al.* (1982), and *Chappell et al.* (1987) further supported the idea that the ionosphere significantly contributed to the magnetosphere. As such, the need for models beyond single fluid magnetohydrodynamics (MHD) were needed to take into account the contribution from the ionospheric plasma.

The first numerical simulation using a multifluid MHD model was developed by *Winglee* (1998). The simulation distinguished solar wind plasma from the ionospheric plasma. This study demonstrated numerically that the ionosphere could be a dominant source of plasma in the plasma sheet. In another study, *Winglee* (2000) extended the numerical simulation to also include ionospheric oxygen and showed that it was possible for oxygen to be found deep in the magnetotail in large concentrations.

Studies by *Glocer et al.* (2009a), *Brambles et al.* (2010), *Wiltberger et al.* (2010), and *Ilie et al.* (2013) also used multifluid MHD codes and demonstrated the impor-

tance of heavy ions outflows. Ionospheric outflow has been attributed as the cause of periodic magnetotail reconnection leading to sawtooth injections *Brambles et al.* (2010); *Wiltberger et al.* (2010). Others have found that O^+ in the inner magnetosphere increases during substorm injections *Ilie et al.* (2013), confirming observational findings *Mitchell et al.* (2001).

Moore (1991) and *Moore and Delcourt* (1995) developed a concept to understand the influence of the ionosphere relative to the solar wind, the geopause. The geopause is a generalization of the magnetopause. The geopause is a surface delimited by equal contributions of the solar wind relative to that of the ionosphere. It can be defined by the number density, mass density, or pressure. For example, the pressure geopause is the surface where the thermal pressure of the solar wind particles equals the thermal pressure of the ionosphere particles.

The analyses performed by *Winglee* (1998) and *Winglee* (2000) presented isosurfaces of the terrestrial geopauses at different time snapshots. A geopause analysis by *Xu et al.* (2016) was applied to Mars to explore the shape of pressure and ion composition boundaries. They also presented time snapshots of the geopauses. Geopause analysis was applied in our previous study *Trung et al.* (2019). We employed a multifluid MHD code coupled to an ionospheric model to compare the geopauses to the magnetopause in steady state under different solar wind magnetic field conditions and ionospheric outflow compositions. Our simulations indicated that no single boundary controlled the transition from a solar wind dominated plasma to an ionosphere dominated plasma.

Most of the geopause studies so far have presented only a few sample times. Thus, more work is required to understand the dynamic behavior of geopauses. In this study, we analyze the dynamics of the different geopause types under various solar wind magnetic field configurations and ionospheric compositions.

4.2 Methods

This study was derived from simulation data generated from the Space Weather Modeling Framework (SWMF) (*Tóth et al.*, 2012). Our previous study (*Trung et al.*, 2019) analyzed the last time step to understand the characteristics of the steady-state geopause. In this paper, we summarize the results of the full 12 hours of simulation data.

Since this study is a follow up to our analysis of the steady state geopause, we provide only a short explanation of our methods used. Using the SWMF, we couple the global magnetosphere to the ionosphere. The ionosphere is modeled through the Ridley Ionosphere Model (RIM) (*Ridley and Liemohn*, 2002; *Ridley et al.*, 2004), which is a two-dimensional height integrated ionospheric potential solver. The potential from RIM is then provided to the global magnetosphere as a horizontal velocity field at its inner boundary. Meanwhile, the global magnetosphere model feeds to RIM the field aligned current.

The global magnetosphere model uses multifluid magnetohydrodynamics (MF-MHD). The equations of MF-MHD are discretized using the Block-Adaptive-Tree Solar wind Roe-type Upwind Scheme (*Powell et al.*, 1999). The implementation of the multifluid equations are presented in (*Glocer et al.*, 2009a). The MF-MHD equations for the global magnetosphere are,

$$\frac{\partial \rho_s}{\partial t} + \nabla \cdot (\rho_s \mathbf{u}_s) = 0, \tag{4.1}$$

$$\frac{\partial \rho_s \mathbf{u}_s}{\partial t} + \nabla \cdot (\rho_s \mathbf{u}_s \mathbf{u}_s + I p_s) = n_s q_s (\mathbf{u_s} - \mathbf{u}_+) \times \mathbf{B} + \frac{n_s q_s}{n_e e} (\mathbf{J} \times \mathbf{B} - \nabla p_e) + S_{\rho_s \mathbf{u}_s}, \tag{4.2}$$

$$\frac{\partial p_s}{\partial t} + \nabla \cdot (p_s \mathbf{u}_s) = -(\gamma - 1) p_s \nabla \cdot \mathbf{u_s}, \tag{4.3}$$

$$\frac{\partial \mathbf{B}}{\partial t} - \nabla \times (\mathbf{u}_+ \times \mathbf{B}) = 0, \tag{4.4}$$

$$\mathbf{u}_+ = \frac{\Sigma_s q_s n_s \mathbf{u_s}}{e n_e} \tag{4.5}$$

$$S_{\rho_s \mathbf{u}_s} = \frac{1}{\tau_c} \sum_{i \neq s} \min(\rho_s, \rho_i)(\mathbf{u}_i - \mathbf{u}_s) \left(\frac{\mid \mathbf{u}_s - \mathbf{u}_i \mid}{u_c} \right)^{\alpha_c} \tag{4.6}$$

Equation 1 is the conservation of mass equation, equation 2 is the momentum equation, equation 3 is the pressure equation, equation 4 is Faraday's law, equation 5 is the charge averaged ion velocity denoted by $\mathbf{u}_+$, and equation 6 is the parameterized interspecies friction term. ρ_s, n_s, $\mathbf{u}_s$, q_s, and p_s, are the mass density, number density, velocity, charge and pressure of the ion species. n_e is the number density of the electron. e is the elementary charge. p_e is the electron gas pressure. It is taken to be 0.2 times the total ion pressure (*Glocer et al.*, 2009a). I is the unit dyadic tensor. γ is the adiabatic index and takes the value of 5/3. τ_c, the cutoff time scale, has a value of 1000 s. $\mathbf{u}_c$, the cutoff velocity, is equal to 100 km/s. α_c, the cutoff exponent, is equal to 2. These numbers are the default values used within the SWMF for artificial friction. i is the index denoting the other ion fluids. The global magnetosphere model uses the Geocentric Solar Magnetospheric (GSM) coordinate system. The simulation bounds (in R_E) are $(X, Y, Z) = [-224, 32] \times [-128, 128] \times [-128, 128]$. We simulated the magnetosphere for 12 hours of simulation time. This study sets the Earth's rotation axis and magnetic dipole along the Z-axis for idealized conditions.

For all simulation runs, the outer boundary will act as the source of the solar wind. It is introduced at X = 32 R_E. The solar wind velocity, magnetic field intensity, mass density and temperature do not change in time. The velocity of the solar wind only has an X-component and is set to -450 km/s. The solar wind mass density is 8.7 amu/cm^3. The solar wind temperature is 1.2×10^5 K. The magnetic field intensity is 10 nT. There are 2 different configurations for the solar wind magnetic field, north-to-south or south-to-north. The magnetic field is only set in the z-direction (B_z). However, it is set northward (positive Z-direction) or southward (negative Z-direction) for a set period of time. In the north-to-south IMF case, B_z is +10 nT from 0:00 UT to 8:00

UT. Then, from 08:01 UT to 12:00 UT, B_z is -10 nT. In the south-to-north case, B_z is -10 nT from 0:00 UT to 4:00 UT, then B_z is 10 nT from 04:01 UT to 12:00 UT.

The inner boundary introduces ionospheric plasma in the simulation. This boundary is centered on Earth with a radius of 2.5 R_E. At the inner boundary, the ionospheric plasma bulk radial velocity is zero. The tangential velocity of the ionospheric plasma at the inner boundary is calculated from the E $\times$ B drift velocity. The inner boundary electric field is determined from the potential calculated by the Ridley Ionospheric Model. Outside of the inner boundary, the ionospheric plasma's momentum is affected by the combination of gyration, J $\times$ B, and electron pressure gradient forces. *Welling and Liemohn* (2014) explored in depth the consequences of using passive outflows in magnetospheric simulations. They found that passive outflows could reproduce dynamical structures found in measurements. Validation studies of various geospace models demonstrated that the passive outflow simulations using the SWMF performed well in data-model comparisons (*Rastätter et al.*, 2011, 2013; *Pulkkinen et al.*, 2010, 2011, 2013). *Liemohn et al.* (2018) performed a long term study using the single fluid version of the SWMF with and without a ring current model to perform data-model comparison on Dst values. Both types of simulations used passive outflow. They found that the simulations with a ring current model performed better than the ones without a ring current model, especially during magnetic storms.

We study four different ionospheric plasma compositions. The different compositions are summarized in Table 4.1. The inner boundary composition is changed, introducing different fractions of O^+ (from 0 to 100 %) so that the number density and/or the mass density at the inner boundary is set to 28.

4.3 Results

Fig. 4.1 and Fig. 4.2 show time snapshots of the geopauses for case 2 for a North-to-South IMF reversal. A more intuitive picture can be formed if the simulation

	Case 1	Case 2	Case 3	Case 4
# of fluids	2	2	3	3
MHD fluids	Sw H^+ Io H^+	Sw H^+ Io O^+	Sw H^+ Io H^+ Io O^+	Sw H^+ Io H^+ Io O^+
% Composition by Number	100 % Io H^+	100 % Io O^+	50 % Io H^+ 50 % Io O^+	94 % Io H^+ 6 % O^+
Total Number Density [/cm^3]	28	28	28	14.875
Total Mass Density [amu/cm^3]	28	448	240	28
Temperature of all ions [10^4 K]	2.5	2.5	2.5	2.5

Table 4.1: Inner Boundary Conditions. Sw is short for solar wind and Io is short for ionospheric.

data from after the IMF reversal is presented. As such, we present time series plots in this section. Animations of the evolution of the geopause after IMF reversal are also included as supplemental information for all 8 simulations being analyzed in this study. Interpretations of the results will be included in the discussion section.

The time series plots presented in this section do not display the full 12 hours of the simulation. Transient effects last for less than three hours after the start of the simulation. In this study, we present the dynamics occurring after the IMF polarity reversal. For the South-to-North IMF configuration, the plot abscissa is from 02:00 UT to 12:00 UT and the polarity reversal time is at 04:00 UT. For the North-to-South IMF configuration, the plot abscissa is from 06:00 UT to 12:00 UT and the reversal time is at 08:00 UT. In comparing Figures 4.1 and 4.2, it is seen that the geopause boundaries are rapidly expanding tailward soon after the IMF reversal. The largest is the mass density geopause (yellow curves), followed by the number density geopause (maroon curves), as expected for ionospheric outflow of pure oxygen ions. The smallest is the pressure geopause, which had collapsed down to the inner boundary of the MF-MHD simulation domain during steady northward IMF but is now quickly expanding from the high-latitude regions. This motion of

the geopauses downtail, first in the lobes and then in the plasma sheet, is evident in all ionospheric composition settings. There are typically several occurrences of near-tail reconnection and plasma composition changes after an IMF reversal, resulting in oscillations of the various parameters to be explored in the following subsections.

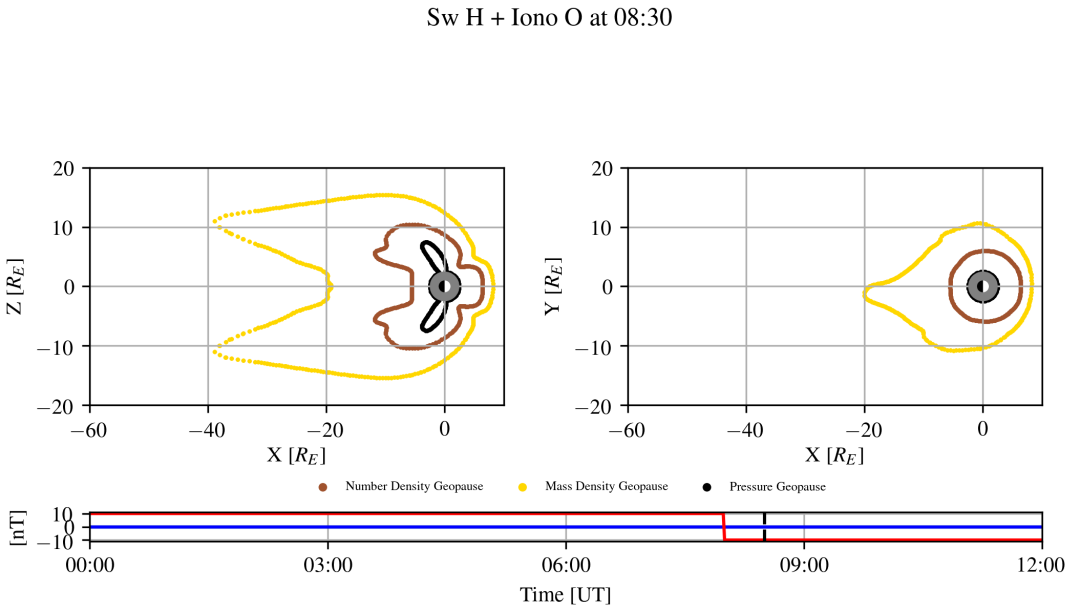

Figure 4.1: Plots of the various geopause definitions at 08:30 UT for a plasma composed of solar wind hydrogen and ionospheric oxygen (Case 2) for the solar wind magnetic field configuration going from North to South. Top left: Meridional cut of the geopauses. Top right: Equatorial cut of the geopauses. Bottom: Solar wind magnetic field in the z-direction as a function of time plotted in red, blue line corresponds to 0, and the dashed black line is a visual indicator of the current time in the simulation.

4.3.1 Cross-Polar Cap Potential

We display the northern cross-polar cap potential (CPCP) in Figure 4.3. The simulations presented here assume that the Earth's spin axis and the magnetic dipole are aligned, the northern hemispheric CPCP values and the southern hemispheric CPCP are identical.

Fig. 4.3(a) displays the CPCP values for the South-to-North IMF configuration.

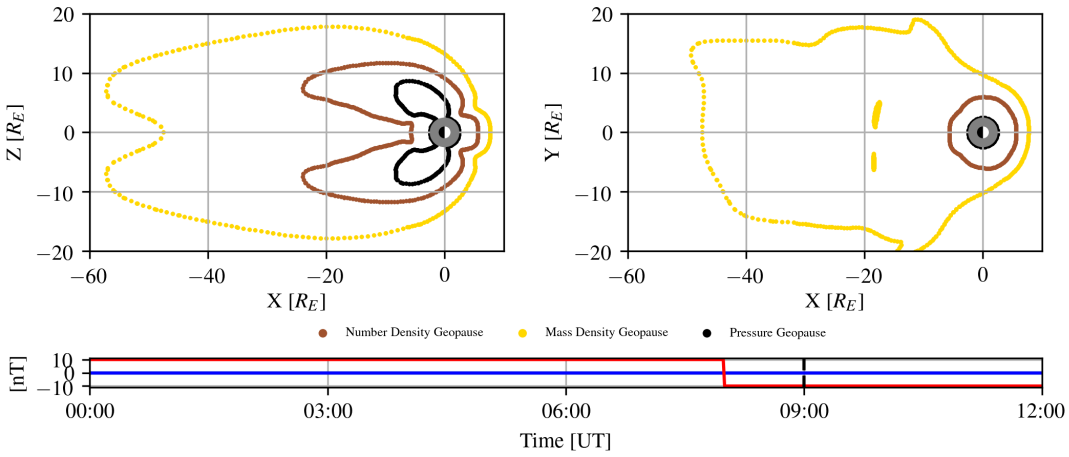

Figure 4.2: Plots of the various geopause definitions at 09:00 UT for a plasma composed of solar wind hydrogen and ionospheric oxygen (Case 2) for the solar wind magnetic field configuration going from North to South. Top left: Meridional cut of the geopauses. Top right: Equatorial cut of the geopauses. Bottom: Solar wind magnetic field in the z-direction as a function of time plotted in red, blue line corresponds to 0, and the dashed black line is a visual indicator of the current time in the simulation.

Before the polarity reversal, the case 2 (blue line) and case 3 (red line) simulations (corresponding to ionospheric outflows dominated by oxygen by mass) have CPCP values close to 165 kV while case 1 (black line) has a CPCP value of about 185 kV and case 4 (green line) has a CPCP value close to 180 kV. After the IMF reversal (at 04:00), the CPCP values for all simulation cases respond to the IMF change at about the same time and drop sharply by about an order of magnitude in about 30 minutes. Then, the voltage slightly increases and subsequently drops in value. The four different outflow cases reach similar CPCP values towards the end of the simulation to 20 kV.

Fig. 4.3(b) displays the CPCP values for the North-to-South IMF configuration. The pattern across all outflow types is a steady voltage around 20 kV during north-

ward IMF, then after the IMF polarity reversal, there is a sharp increase in CPCP values followed by peaks and valleys. During northward IMF, the CPCP values are nearly identical across all of the ionospheric outflow cases. After the IMF reversal to South, the voltages increase in value at nearly the same rate until they reach the first peak. For case 1 (hydrogen ionosphere, black line), the voltage peaks to a value of 198 kV at 08:57 and enters a near steady state near 10:40 UT. For case 2 (oxygen ionosphere, blue line), the voltage peaks to a value of 183 kV at 09:20, then has a second peak of 174 kV at 10:27, and enters a near steady state at 10:50. For case 3 (hydrogen and oxygen ionosphere in equal number density, red line), the voltage peaks to a value of 185 kV at 09:10 and enters near steady state state around 10:20. For case 4 (hydrogen and oxygen ionosphere with a combined mass density of 28 amu/cm^3, green line), the voltage peaks to a value of 198 kV at 08:58 and enters near steady state state around 10:45.

4.3.2 Effect of outflow composition on nightside geopause dynamics

In this section, we present time series of the nightside geopause location closest to Earth for all three definitions of the geopause (number density, mass density, and pressure). To develop an intuition for geopause dynamics, the geopause time series are presented along the Sun-Earth line (Y = 0, Z = 0) in the nightside.

4.3.2.1 Number Density Geopause

In Fig. 4.4(a), the nightside number density geopause for the South-to-North IMF configuration is plotted. Before the change in solar wind magnetic field polarity, the number density geopause displays an ordering by conditions in the outflow. The ordering of the number density geopause closest to Earth is the outflow with ionospheric hydrogen and very slight traces of oxygen (case 4, green line) at -31 R_E, the 100% hydrogen ionospheric outflow (case 1, black line) at -36 R_E, the 50-50 mix of hydrogen

and oxygen (case 3, red line) at -50 R_E, and finally the pure oxygen outflow (case 2, blue line) at -53 R_E. After the reversal, the lighter outflow cases respond to the IMF changes before the heavier cases. For case 1 and case 4, the number density geopauses start to retreat earthward at 04:25. For case 3, the number density geopause starts to expand at 04:38. For case 2, the start time is 04:46. The final number density geopause locations are nearly identical across all cases at -6 R_E.

In contrast, Fig. 4.4(b) shows the nightside number density geopause for the North-to-South IMF configuration. Pre-reversal, the nightside number density geopause for all outflows are close in value at -6 R_E. After the solar wind's magnetic field reverses from 10 nT to -10 nT at 08:00 UT, the nightside Sun-Earth number density geopause across all outflows respond to the changes at about the same time, 09:00 UT. However, after 09:00 UT, the number density geopauses evolve according to the inner boundary conditions. The simulation cases with only ionospheric hydrogen (case 1, black line) and both ionospheric hydrogen and oxygen at 28 amu/cm^3 (case 4, green line) settle to a steady state at 11:00. The simulation with ionospheric oxygen and solar wind hydrogen (case 2, blue line) enters a steady state at 11:20. The simulation with equal parts of ionospheric oxygen and ionospheric hydrogen and solar wind enters steady state sooner, at 11:10. The number geopauses have spiky features appearing as a response to the IMF reversal. For case 1, the spikes occur at 09:05 and 09:59. For case 2, there are spikes at 09:20, 09:39, 10:35, and 10:52. For case 3, the spikes are at 09:16, 09:28, 09:57, and 10:14. For case 4, the spikes occur at 09:03 and 09:55. At the end of the simulation, the pure oxygen outflow and 50-50 oxygen outflow cases have density geopauses locations around -54 R_E and -49 R_E respectively. The pure hydrogen outflow has a density geopause locations around -36 R_E. The outflow composed of 6% oxygen and 94% ionospheric hydrogen by number has a density geopause location around -30 R_E.

4.3.2.2 Mass Density Geopause

The mass density geopause locations along the Sun-Earth line present similar features compared to the number density geopause. That is there is an ordering by the mass density of the ionospheric outflow. For the south-to-north IMF case (Fig. 4.5(a)), the mass density geopauses of cases 1 and 4 (black and green lines) respond to the IMF changes at 04:25. Case 2 (blue line) starts responding at 04:41. Case 3 (red line) responds at 04:30. Cases 1 and 4 enter steady state at 06:10 and ends the simulation with a mass density geopause location of -5 R_E. Case 3 enters steady state at 07:20 and has a final value of about -18 R_E. Case 2 enters steady state at 07:30 and has a final value of -30 R_E.

Looking at the North-to-South IMF configuration (Fig. 4.5(b)), the mass density geopauses for all cases start to respond at 08:40. Cases 1 and 4 spike at 09:05. Case 2 has spikes at 09:45 and 10:56. Case 3 has spikes at 09:30 and 10:11. The mass density geopauses for case 1 and 4 enter near steady state at 11:00. Cases 2 and 3 do not seem to enter a steady state.

4.3.2.3 Pressure Geopause

Fig. 4.6(a) displays the nightside pressure geopause along the Sun-Earth line for the South-to-North IMF configuration. Case 1 responds to the IMF polarity reversal at 04:18 while case 4 responds at 04:10. Case 2 responds at 04:35. Case 3 responds at 04:32. Similar to the mass density geopauses, the oxygen rich outflow cases (blue and red lines) respond last to the changes in the solar wind magnetic field. They take the longest time to return to a steady state with a pressure geopause location of -2.5 R_E. The pressure geopause for case 1 reaches steady state at 06:21. Case 2 reaches steady state at 08:52. Case 3 reaches steady steate at 07:48. Case 4 reaches steady state at 05:51.

Fig. 4.6(b) displays the nightside pressure geopause for the North-to-South IMF

configuration. Case 1 responds to the IMF reversal at 09:32. Case 2 responds at 09:25. Case 3 responds at 09:20. Case 4 responds at 09:31. Case 1 has a spike at 10:05. Case 2 has a spikes at 09:38, 10:01, 10:58, and 11:20. Case 3 has spikes at 09:23, 09:40, 10:07, and 10:31. Case 4 has a spike at 09:54. The pressure geopauses for case 2 and 3 do not appear to reach a near steady state. Case 1 reaches a steady state at 10:50. Case 4 reaches a steady state at 10:05.

Table 4.2 summarizes the response timings for the South to North IMF configuration while Table 4.3 summarizes the response timings for the North to South IMF configuration.

	Cross Polar Cap Potential Response Time (in UT)	Number Density Geopause Contraction Start Time(in UT)	Mass Density Geopause Contraction Start Time (in UT)	Pressure Geopause Contraction Start Time (in UT)
Case 1 (Sw H^+ + Io H^+)	04:10	04:25	04:25	04:18
Case 2 (Sw H^+ + Io O^+)	04:10	04:46	04:41	04:35
Case 3 (Sw H^+ + Io H^+ + Io O^+)	04:10	04:38	04:30	04:32
Case 4 (Sw H^+ + Io H^+ + Io O^+ at 28 amu/cc)	04:10	04:25	04:25	04:10

Table 4.2: Summary of response timings for the South-to-North IMF simulations. Sw is short for solar wind and Io is short for ionospheric.

	Cross Polar Cap Potential Spike Timings (in UT)	Number Density Geopause Spike Timings (in UT)	Mass Density Geopause Spike Timings (in UT)	Pressure Geopause Spike Timings (in UT)
Case 1 (Sw H^+ + Io H^+)	08:57	09:05 09:59	09:05 09:59	10:05
Case 2 (Sw H^+ + Io O^+)	09:20 10:27	09:20 09:39 10:35 10:52	09:46 10:00 10:56 11:18	09:38 10:01 10:58 11:20
Case 3 (Sw H^+ + Io H^+ + Io O^+)	09:10	09:16 09:28 09:57 10:14	09:30 09:43 10:11 10:29	09:23 09:40 10:07 10:31
Case 4 (Sw H^+ + Io H^+ + Io O^+ at 28 amu/cc)	08:58	09:03 09:55	09:05 09:58	09:54

Table 4.3: Summary of spike timings for North-to-South IMF simulations. Sw is short for solar wind and Io is short for ionospheric.

4.3.3 Comparison of Plasma Properties with Geopauses along the Sun-Earth Line

The figures presented in this section (Fig. 4.7-4.10) plot the geopause locations along the Sun-Earth line (number density, mass density, and pressure) as a function of time for each outflow case. In the background of these plots, we plot 3 parameters along the negative x-axis: the current density in the y-direction, the solar wind velocity in the x-direction, and the z-component of the magnetic field. These three parameters are chosen to provide a fair comparison across all simulations. The magnetic field values plotted have been limited to absolute values of B_z above 10 nT in order to not saturate the magnetic field values due to the Earth's dipolar magnetic field.

In Fig. 4.7, the geopause locations for a plasma composed of ionospheric hydro-

gen and solar wind hydrogen are presented. Since hydrogen is the only component of both the solar wind plasma and the ionospheric plasma, the calculation to determine the mass density geopause and number density geopause are identical. Thus, the mass density geopause and number density geopause have the same size and shape. Shortly after the solar wind magnetic field reverses from south to north (Fig. 4.7(a)), the current density in the y-direction (J_y) along the Sun-Earth line begins to weaken, this is accompanied by the geopause locations moving Earthward. After the IMF reversal, J_y settles to a relative steady state faster than the geopauses. In Fig. 4.7(b), the intensification of J_y along the Sun-Earth line is followed by the expansion in the geopause locations. Some of these features move very fast downtail as the magnetosphere reconfigures for the new and stronger driving conditions. It is also seen that the motions of the geopause locations sometimes follows the current density changes, but other times do not, such as the large excursions occurring near 10:00.

Shortly after the South-to-North IMF reversal, the solar wind x-velocity penetrates the nightside magnetosphere as the geopauses compress (Fig. 4.7(c)) and the magnetic field is dominated entirely by the solar wind (Fig. 4.7(e)). In the North-to-South IMF case, the expansion of the mass density geopause and number density geopause is preceded by solar wind velocity signatures going in opposite directions (Fig. 4.7(d). In Fig. 4.7(f), there are two white bands corresponding to very weak values in B_z.

In the case of a oxygen-only ionospheric outflow (Fig. 4.8), J_y behaves in a similar manner compared to a hydrogen-only ionospheric outflow after the IMF changes polarity. For the South-to-North case (Fig. 4.8(a)), The current density J_y weakens and is accompanied by a decrease in the size of the geopause along the x-direction. The compression of the geopauses is also accompanied by an enlarging channel of near neutral solar wind velocity extending from the number density geopause past the mass density and pressure geopauses (Fig. 4.8(c)). There is also a signature (Fig.

4.8(e)) with alternating colors for B_z. For the North-to-South case (Fig. 4.8(b)), the growth in geopause location is accompanied by the intensification of J_y. A near neutral solar wind x-velocity channel is also observed before the expansion of the geopauses (Fig. 4.8(d)). Unlike Case 1, there are now 5 white bands in Fig. 4.8(f). 4 of those bands are close to the geopause spike.

With the outflow consisting of equal parts of ionospheric oxygen and ionospheric hydrogen by number (Fig. 4.9), we observe a similar behavior where the weakening of the current density is accompanied by a drop in the geopause location and the intensification of the current density is accompanied by the expansion of the geopauses. Similar to Case 2, geopause compressions and expansions are preceded by a channel of near neutral solar wind x-velocity. This case also observes 5 channels of weak B_z values.

For the outflow case consisting of 94% ionospheric hydrogen and 6% ionospheric oxygen (Fig. 4.10), the plots resemble the case where the magnetospheric plasma includes both solar wind hydrogen and ionospheric hydrogen. However, in this case, the number density geopause and mass density geopauses are separate. The number density geopause is smaller compared to the mass density geopause. Also, the pressure geopause is greatly reduced in its downtail distance here in Case 4 compared to Case 1 shown in Figure 4.6, both for northward and southward IMF. Even though the mass density at the inner boundary is the same between Cases 1 and 4, the reduced number density at the inner boundary for Case 4 significantly impacts not only the number density geopause but also the pressure geopause. The magnetopause as defined by the last closed field line, however, is essentially the same between Cases 1 and 4, shifting outward by 1 to 2 R_E in Case 4 compared to Case 1. The solar wind velocity profile along the Sun-Earth line and magnetic field z-component display a similar profile as in Case 1. Case 4 has 2 white bands.

4.4 Discussion

The results presented above can be interpreted in several ways. Below we examine the reasons for the dynamical features seen during the IMF turnings and put these into the context of the different ionospheric outflow conditions applied in the 4 runs. We discuss the connection of geopause motion with some physical parameters but not with others, and the relationship of outflow mass density to the formation of magnetotail dynamical structures.

Taking a closer look at the geopauses for each type of outflow (Fig. 4.7-4.10), we see that for the South-to-North IMF case after the IMF reversal, the decoupling of the IMF with the Earth's magnetosphere leads to a reduction in magnitude and size of the current sheet. Shortly after the reduction in current density in the y-direction, the geopauses begin to shrink in size. However, the geopauses' dynamical behavior are not as correlated with J_y for northward IMF as both the solar wind velocity and B_z are. The outflow mass densities and number densities do not seem to affect the geopause contraction start times as strongly as the geopause starting position. In this IMF configuration, it also seems, as seen by comparing Figure 4.3 with Figures 4.4-4.6, that the outflow mass density and number density do not affect the cross polar cap potential, as seen in Figures 4.3-4.6.

For the North-to-South IMF case, the increasing mass densities between the cases seem to delay spike timings of the geopauses and the cross polar cap potential. In this magnetic field configuration, the current density intensifies after the IMF reverses. This is due to the magnetic flux coming from the dayside magnetopause. The intensification of the current density is then followed by the expansion in size of the geopauses due to the increased ionospheric outflow. Similar to the South-to-North IMF case, the dynamical behavior of the geopauses do not correlate well with J_y along the Sun-Earth line, as evidenced in the (b) panels of Figures 4.7-4.10. The cross polar

cap potential profile is affected by the concentration of oxygen in the outflow with higher mass density outflows reaching smaller peaks and steady state voltages.

After the IMF reversal for both configurations, the current density in the y-direction enters steady state faster than the z-component of the magnetic field and the x-velocity of the solar wind along the Sun-Earth line. This indicates that the cross tail current does not play a significant role in shaping geopause dynamics compared to the magnetic field. The connection between the number density, mass density geopause and the magnetic field can be seen through the momentum equation. The ratio of the plasma ion number density to the total plasma number density multiplies the difference between J $\times$ B and ∇p_e. When this ratio is 0.5, it defines the number density geopause and physically represents a location where the J $\times$ B and ∇p_e is applied equally to the solar wind plasma and total ionospheric plasma. The magnetic field also appears in the gyration term. The x-velocity of the various plasma species is also important in impacting the pressure geopause. In the pressure equation, the total time derivative of the plasma pressure of one species depends on the divergence of the plasma species velocity. Thus, the variation in the x-velocity of the solar wind along the Sun-Earth line have shown profiles consistent with the evolution of the pressure geopauses.

The white bands for B_z observed for the North-to-South IMF case in Fig. 4.7(f), 4.8(f), 4.9(f), 4.10(f) correspond to plasmoid signatures. Thus, cases 1 and 4 have two plasmoid signatures while cases 2 and 3 have five plasmoid signatures. The first plasmoid formed results from the IMF magnetic field inversion from North-to-South. Some of the plasmoid signatures are coincident with spikes in the cross-polar cap potential. For these plasmoids, the white bands are bracketed by red and blue bands indicating a more intense plasmoid signature. The plasmoid signatures in our simulations are often precursors to the geopause expansion and spike timings. The additional plasmoid release due to a more massive ionosphere has also been observed

in a study done by *Wiltberger et al.* (2010). In cases 2 and 3, the pressure geopause is larger than the number density geopause. While for cases 1 and 4, the number density geopause is larger than the pressure geopause. If the pressure geopause is larger than the number density geopause, the region outside of the number geopause has hot ionospheric plasma. If the number density geopause is larger than the pressure geopause, the region outside of the pressure geopause has cold ionospheric plasma (*Winglee*, 1998). Thus, the additional plasmoids observed in cases 2 and 3 seem to be coincident with the presence of hot ionospheric plasma in a larger volume in the magnetosphere.

In the case of the South-to-North IMF configurations, cases 2 and 3 release a plasmoid. For these simulations, the same geopause pattern appears: the number density geopause is larger than the pressure geopause. For cases 1 and 4, the geopause pattern is inverted and lacks the formation of a plasmoid.

As clearly seen in the case comparison plots of Figures 4.3-4.6, the simulations with oxygen-dominated outflow take longer to reach a steady state configuration in the magnetotail compared to the hydrogen-dominated outflow cases. This is true for both of the IMF turning configurations.

As mentioned in our previous study, our simulations do not include an inner magnetosphere model, at this time there is no inner magnetosphere model publicly available in the SWMF capable of distinguishing hydrogen plasma by their original source. The simulations performed by *Winglee* (2000) have not included an inner magnetosphere model but, like those presented here, separated solar wind hydrogen from ionospheric hydrogen. In contrast, SWMF simulations where an inner magnetosphere model was coupled to a multifluid MHD model have not distinguished the hydrogen by its sources *Glocer et al.* (2009a, 2013); *Ilie et al.* (2015b); *Welling et al.* (2015); *Liemohn and Welling* (2016); *Komar et al.* (2017).

Because this study involves idealized numerical experiments, the results should

be considered as a qualitative guideline for interpreting geospace observations. That is, the simplified inputs mean that the results should not be directly compared with real event scenarios. The chosen input parameters for these simulations are common, making these results generally indicative of the influence of ionospheric outflow, and applicable for understanding the dynamics of the Earth's geopauses during IMF turning events.

4.5 Conclusion

In this study, we explored the effects of ion composition for passive outflows on the dynamics of the magnetosphere. In the cases where the IMF has changed from North to South, it seems that the mass density (not the number density) of the ionospheric outflow plays a significant role in the dynamics of the magnetosphere. In the cases where the IMF changes from South to North, the dynamics are dependent on the magnetospheric conditions before the reversal which are controlled by the outflow mass density.

In the North-to-South IMF simulations, the geopause response time along the negative x-axis was faster for more massive outflows during southward IMF conditions as seen in the mass density and pressure geopauses. In the mass density and pressure geopauses, the oxygen dominated outflows responded 10 minutes faster than the hydrogen dominated outflows. Increasing the mass density of the ionospheric outflow both increases the region of influence of the Earth's ionospheric particles and increases the time for the magnetosphere to return to a steady state in southward IMF.

While the geopauses for the South-to-North IMF seem to indicate that the ionospheric boundary mass density seems to play a role, the differences in the response time between the simulations is accounted by the large differences in the geopause positions before the solar wind magnetic field polarity reverses. The cross-polar cap

potential produced similar voltage values during northward IMF independent of the mass density of the ionospheric outflow.

Along the Sun-Earth line, we also analyzed the relationship between the geopauses and the magnetic field in the z-direction, the bulk solar wind x-velocity, and the y-current density. The cross tail current did not seem to affect the dynamics of the geopauses as strongly as the magnetic field and the solar wind velocity.

The compositional changes, including the location of the geopauses, often closely matches these plasmoid releases and downtail motion. As the magnetic field oscillates and eventually settles after the IMF reversal, so do the plasma geopauses into their new steady-state configurations. The solar wind x-velocity after reversal generates large regions of near zero values indicative of changes in the size of the nightside magnetopause.

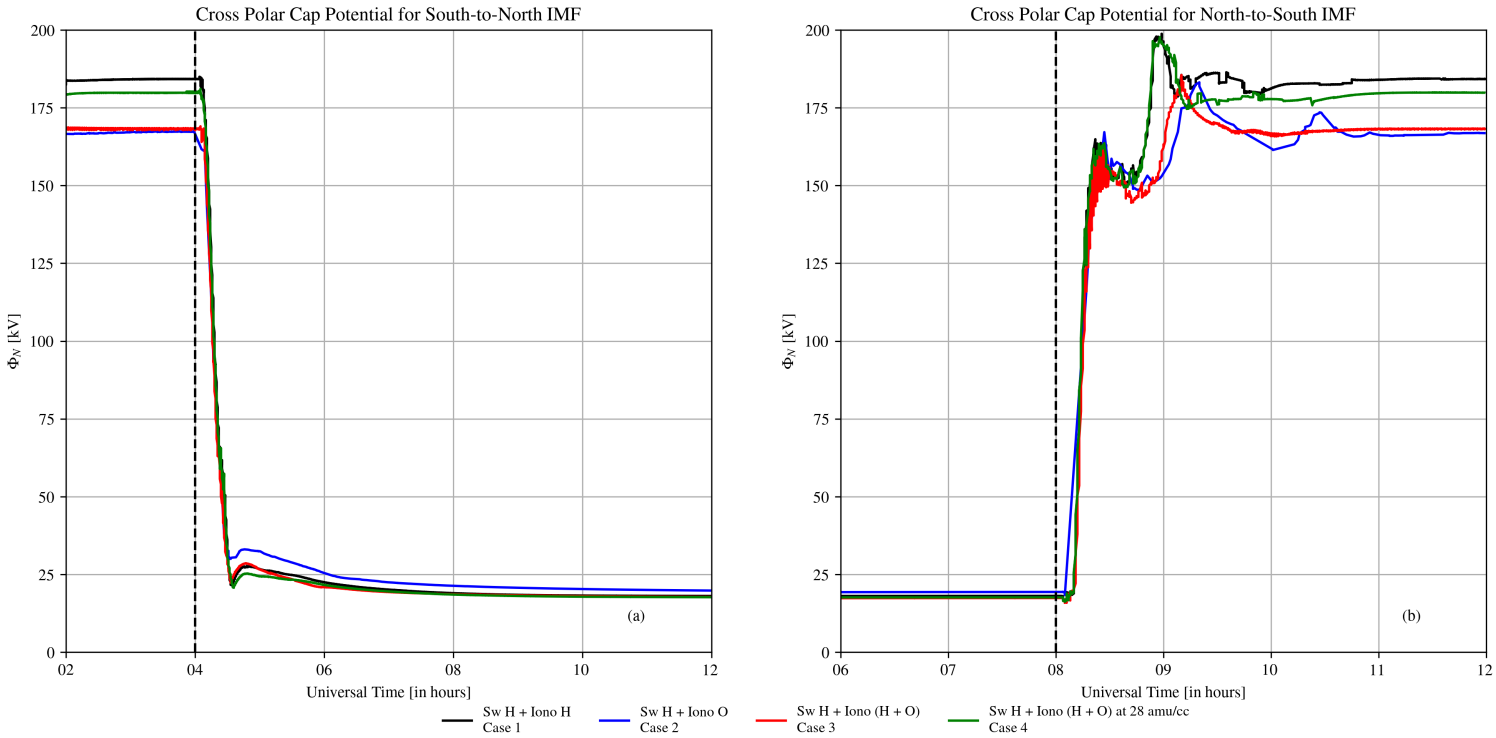

Figure 4.3: Plots of cross-polar cap potential. (a) Left, CPCP for the South-to-North IMF configuration. The dashed vertical line at 04:00 UT corresponds to the IMF reversal from South-to-North. (b) Right, CPCP for the North-to-South IMF configuration. The dashed vertical line at 08:00 UT corresponds to the IMF reversal from North-to-South.

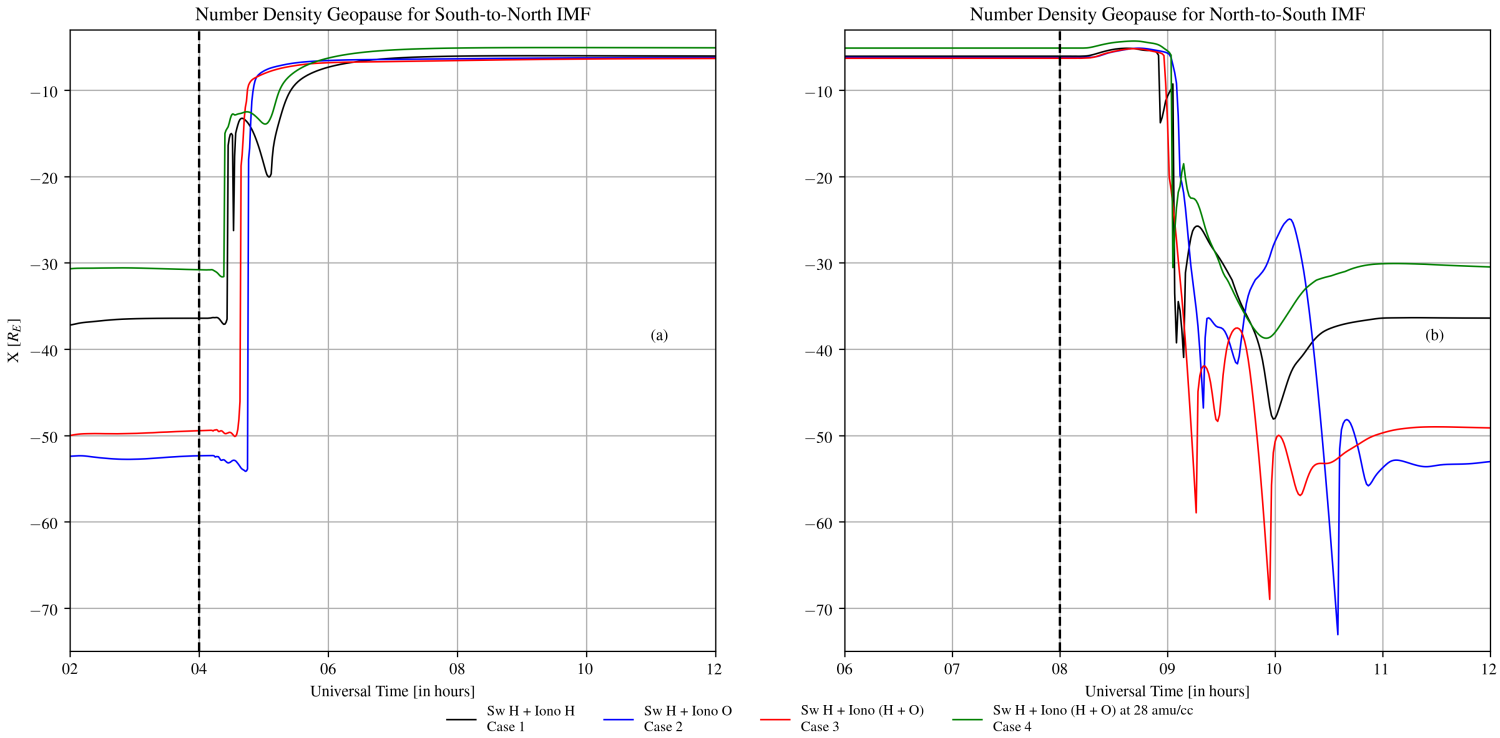

Figure 4.4: Time series of the nightside number density geopause along the Sun-Earth line (a) Left, South-to-North IMF configuration. The dashed vertical line at 04:00 UT corresponds to the IMF reversal from South-to-North. (b) Right, North-to-South IMF configuration. The dashed vertical line at 08:00 UT corresponds to the IMF reversal from North-to-South.

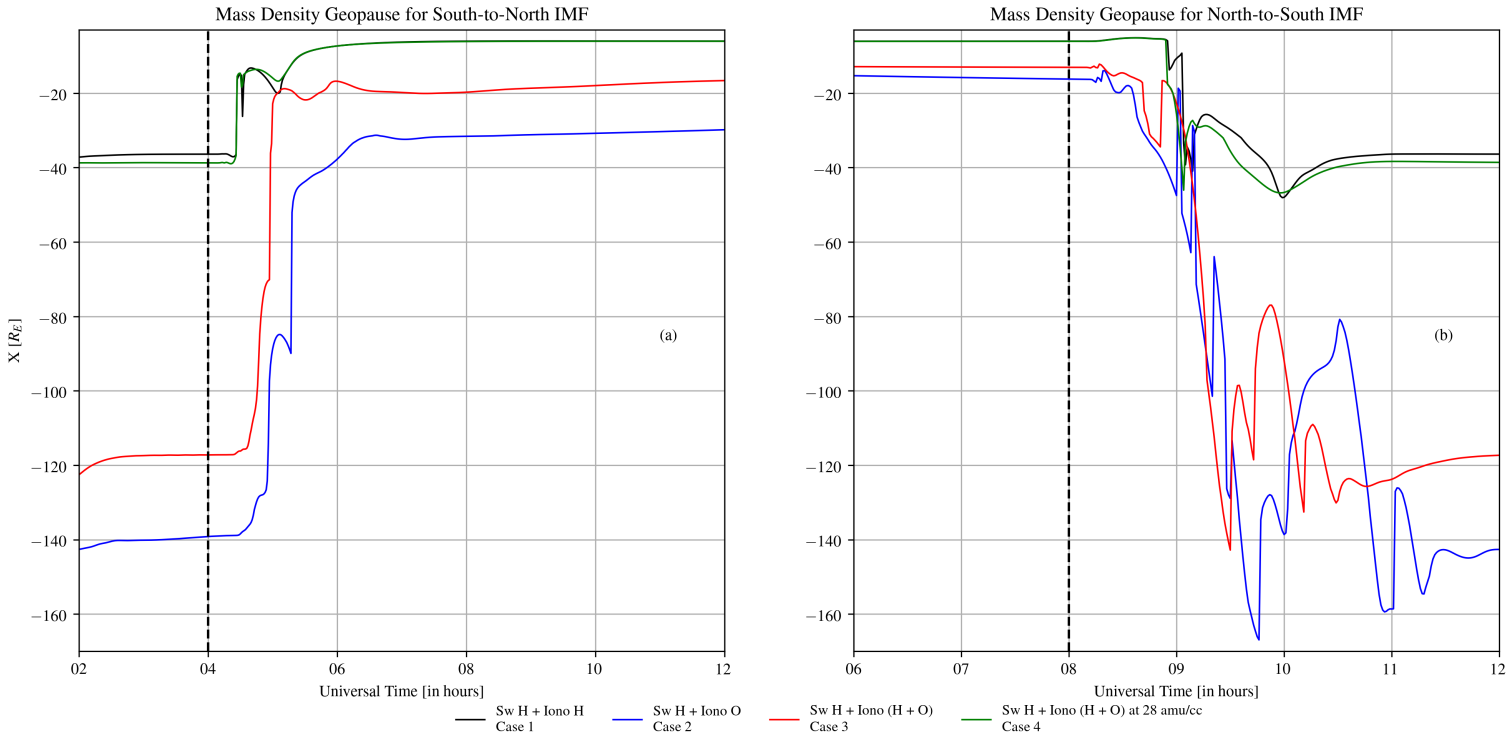

Figure 4.5: Time series of the nightside mass density geopause along the Sun-Earth line (a) Left, South-to-North IMF configuration. The dashed vertical line at 04:00 UT corresponds to the IMF reversal from South-to-North. (b) Right, North-to-South IMF configuration. The dashed vertical line at 08:00 UT corresponds to the IMF reversal from North-to-South.

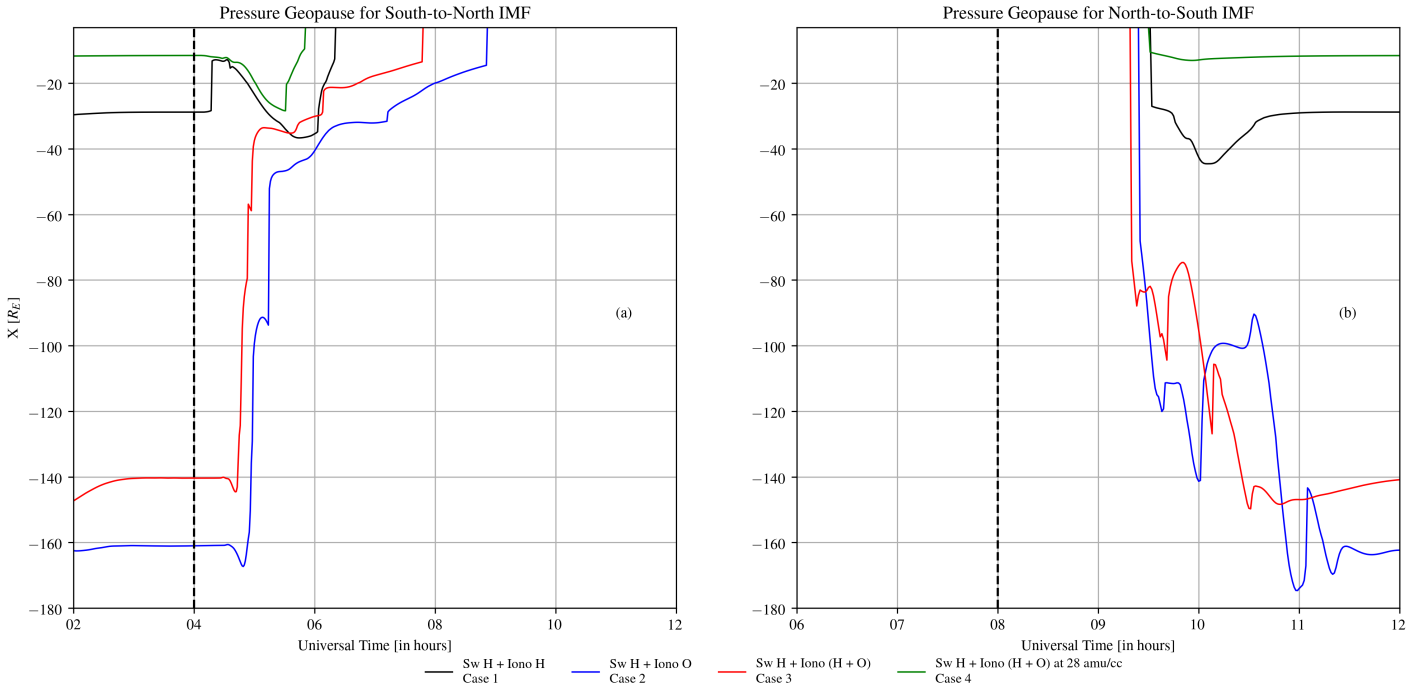

Figure 4.6: Time series of the nightside pressure geopause along the Sun-Earth line (a) Left, South-to-North IMF configuration. The dashed vertical line at 04:00 UT corresponds to the IMF reversal from South-to-North. (b) Right, North-to-South IMF configuration. The dashed vertical line at 08:00 UT corresponds to the IMF reversal from North-to-South.

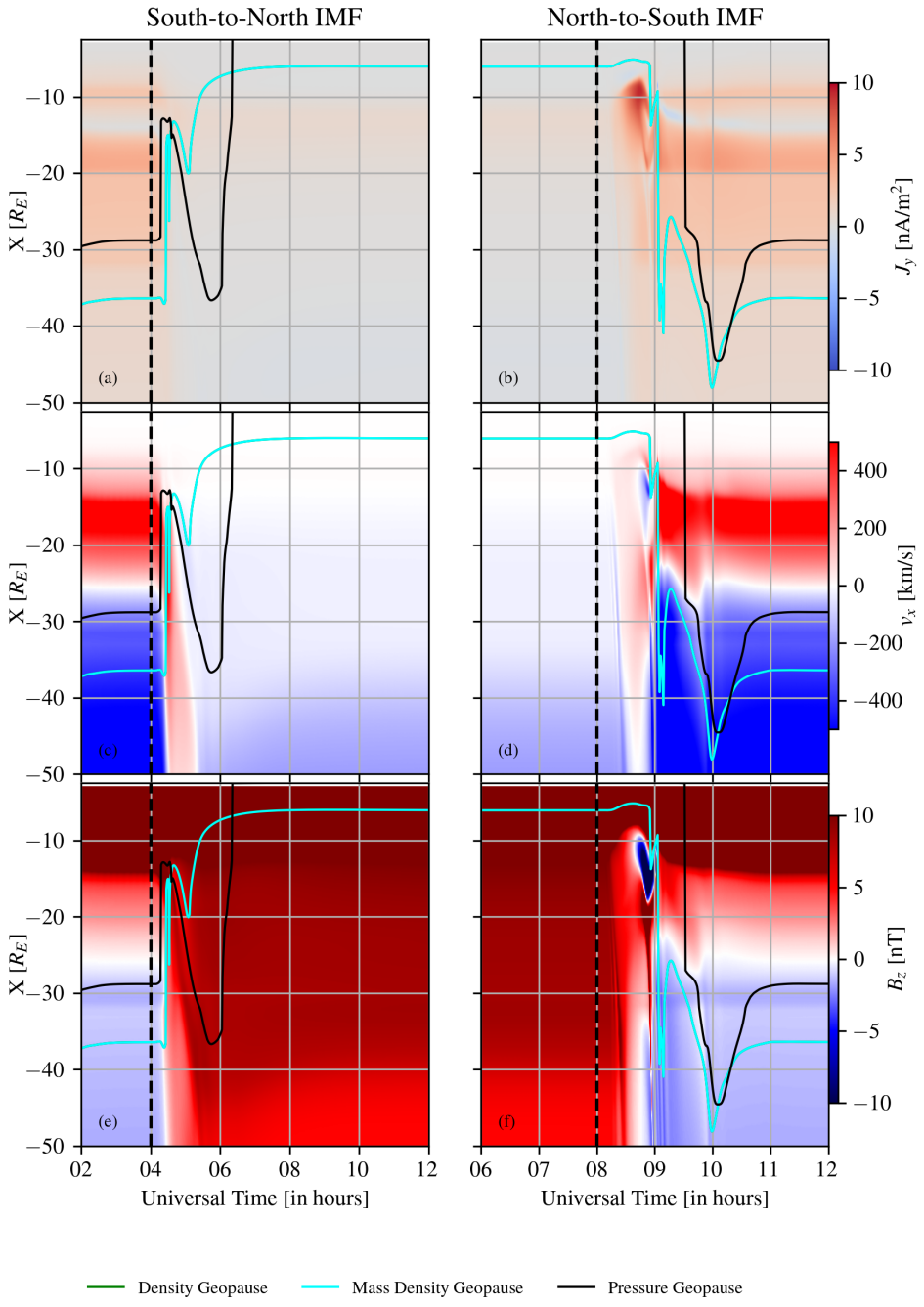

Figure 4.7: Time series of the nightside geopauses along the negative x axis for a plasma composed of solar wind hydrogen and ionospheric hydrogen. Top row, y-component of the current density. Middle row, solar wind velocity in the x-direction. Bottom row, z-component of the magnetic field. Left column, South-to-North IMF configuration. The dashed vertical line at 04:00 UT corresponds to the IMF reversal from South-to-North. Right column, North-to-South IMF configuration. The dashed vertical line at 08:00 UT corresponds to the IMF reversal from North-to-South. Note that the number density and mass density geopauses are identical.

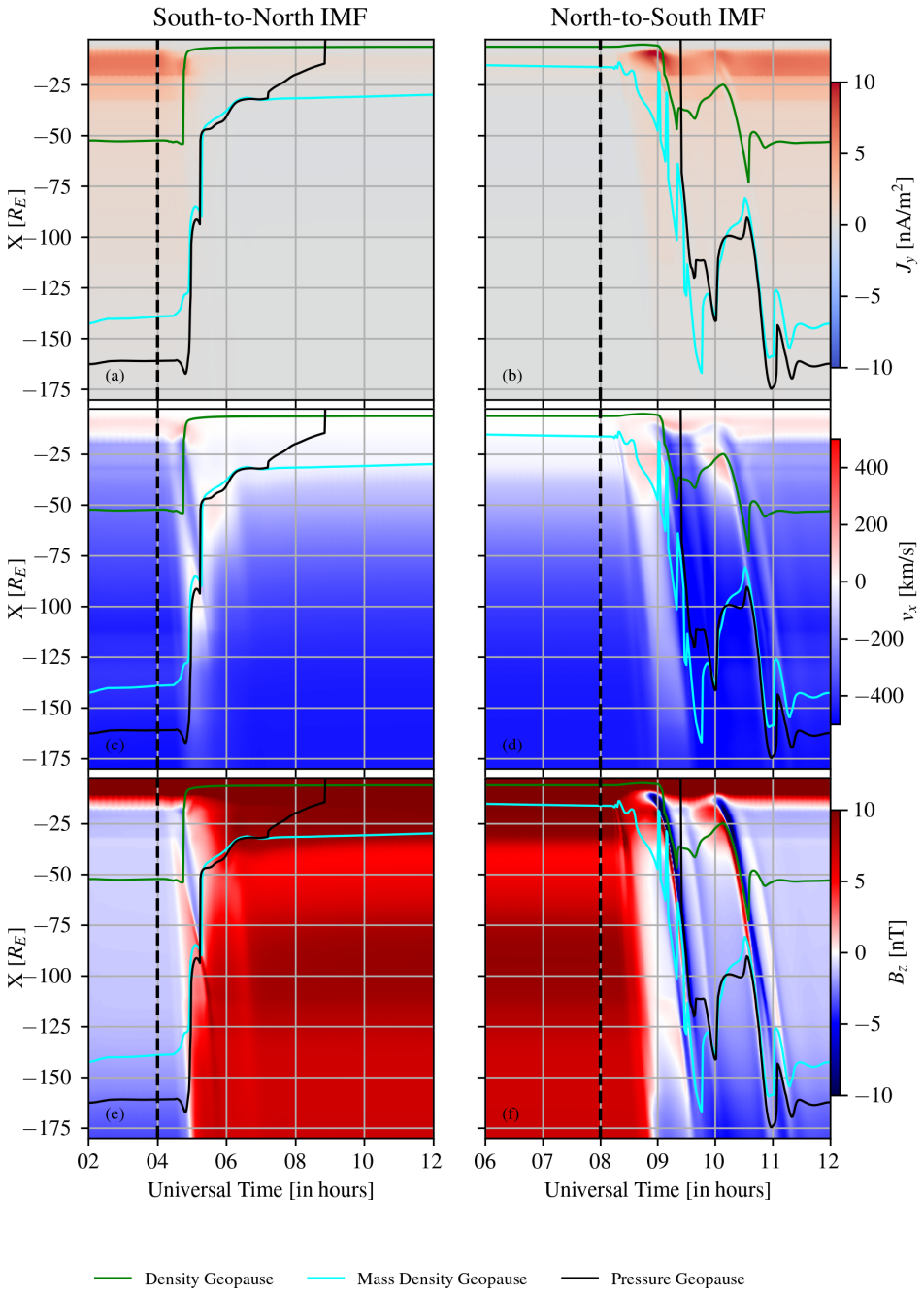

Figure 4.8: Time series of the nightside geopauses along the Sun-Earth line for a plasma composed of solar wind hydrogen and ionospheric oxygen. Top row, y-component of the current density. Middle row, solar wind velocity in the x-direction. Bottom row, z-component of the magnetic field. Left column, South-to-North IMF configuration. The dashed vertical line at 04:00 UT corresponds to the IMF reversal from South-to-North. Right column, North-to-South IMF configuration. The dashed vertical line at 08:00 UT corresponds to the IMF reversal from North-to-South.

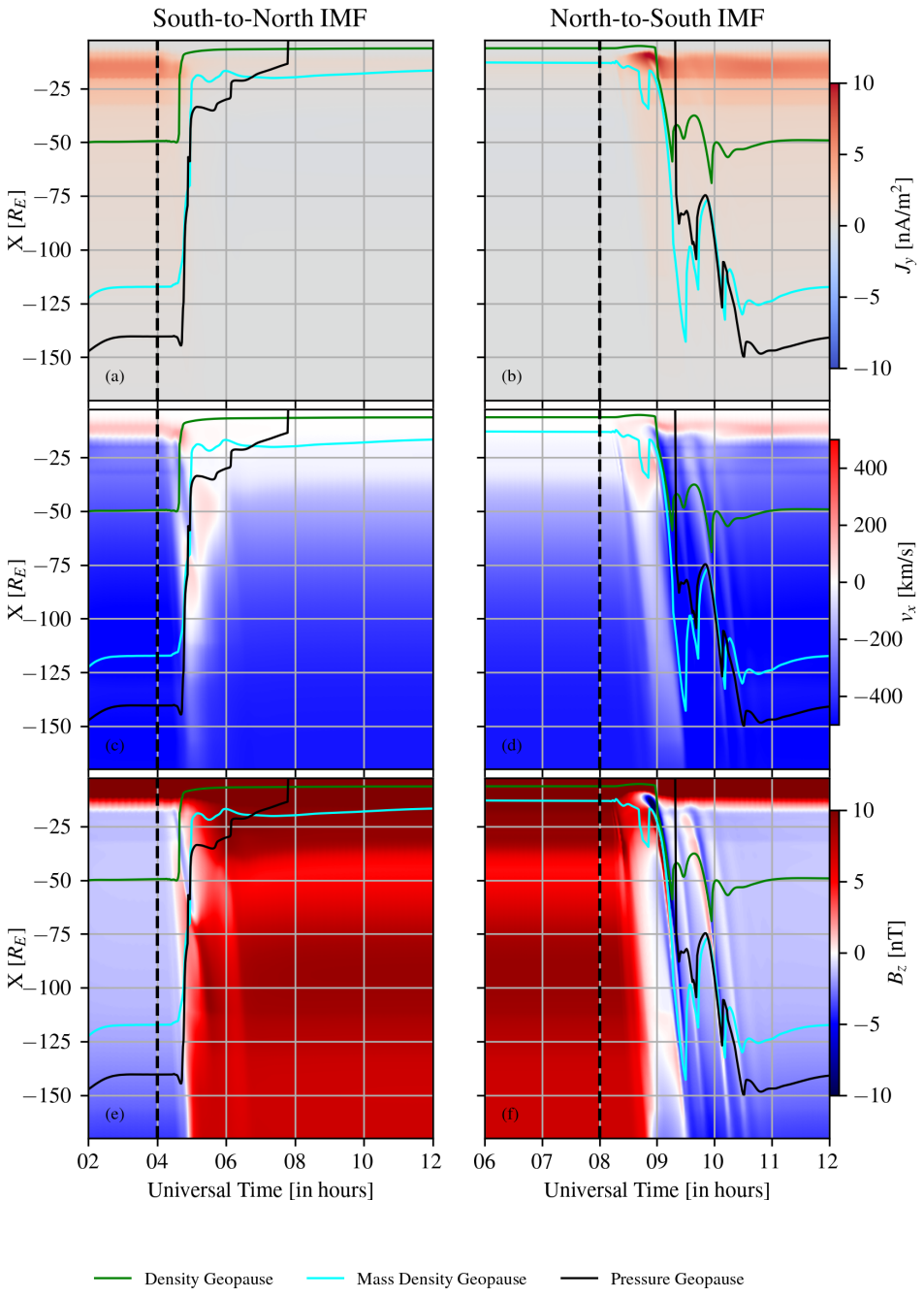

Figure 4.9: Time series of the nightside geopauses along the Sun-Earth line for a plasma composed of solar wind hydrogen, and ionospheric hydrogen and oxygen. Top row, y-component of the current density. Middle row, solar wind velocity in the x-direction. Bottom row, z-component of the magnetic field. Left column, South-to-North IMF configuration. The dashed vertical line at 04:00 UT corresponds to the IMF reversal from South-to-North. Right column, North-to-South IMF configuration. The dashed vertical line at 08:00 UT corresponds to the IMF reversal from North-to-South.

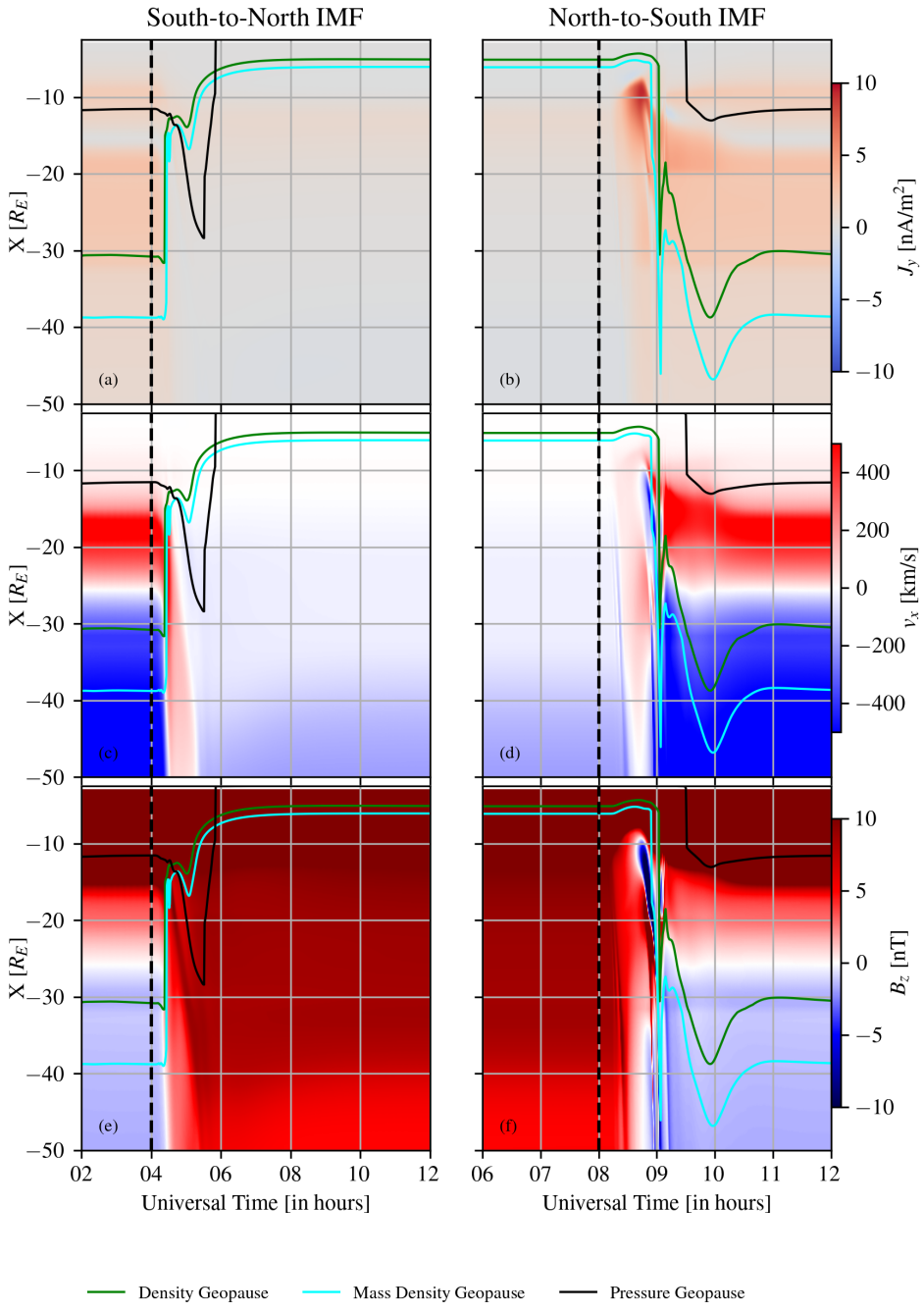

Figure 4.10: Time series of the nightside geopauses along the Sun-Earth line for a plasma composed of solar wind hydrogen, and ionospheric hydrogen and oxygen at an inner boundary mass density of 28 amu/cm^3. Top row, y-component of the current density. Middle row, solar wind velocity in the x-direction. Bottom row, z-component of the magnetic field. Left column, South-to-North IMF configuration. The dashed vertical line at 04:00 UT corresponds to the IMF reversal from South-to-North. Right column, North-to-South IMF configuration. The dashed vertical line at 08:00 UT corresponds to the IMF reversal from North-to-South.

CHAPTER V

Momentum Sources in Multifluid MHD and their Relation to the Geopauses

5.1 Introduction

Multifluid magnetohydrodynamics (MHD) enables the individual tracking of the mass density, pressure, and velocities of a multicomponent plasma. One of the first documented applications of multifluid MHD in the Earth's magnetosphere was by *Winglee* (1998). The two fluid components of the magnetospheric plasma used in that study were solar wind hydrogen ions and ionospheric hydrogen ions. Other research groups extended the capabilities of their single fluid MHD codes to multifluid MHD such as BATS-R-US (*Glocer et al.*, 2009a) and LFM (*Wiltberger et al.*, 2010) . In those cases, they used either an empirical outflow model (*Wiltberger et al.*, 2010) or a physical outflow model (*Glocer et al.*, 2009a) in order to introduce ionospheric plasma into the magnetosphere. *Winglee* (1998) introduced ionospheric outflow through centrifugal acceleration.

Another type of outflow used in MHD simulations is through a passive boundary. With this boundary condition, the ionospheric plasma is set to have zero radial velocity. Thus, the ionospheric plasma can only be introduced in the magnetosphere through MHD forces and numerical diffusion. *Welling and Liemohn* (2014) analyzed

the use of passive outflow in terrestrial magnetospheric simulations. They showed that passive outflow could reproduce some of the magnetospheric dynamics. However, one unrealistic behavior with single fluid MHD was an oscillating flux after an interplanetary magnetic field (IMF) reversal. This behavior was attributed to the fact that single fluid MHD has a single bulk velocity describing both solar wind and ionospheric plasma motion. Passive outflows do not describe the physical processes governing outflow. Nonetheless, passive outflow boundary conditions have been widely used in operational implementations of the Space Weather Modeling Framework (*Tóth et al.*, 2007) at the Community Coordinated Modeling Center (CCMC) and NOAA's Space Weather Prediction Center. Several studies have compared different geospace models used at CCMC (*Rastätter et al.*, 2013; *Gordeev et al.*, 2015; *Ridley et al.*, 2016; *Liemohn et al.*, 2018; *Kubyshkina et al.*, 2019). They demonstrated that global magnetospheric models perform quite well and reproduced the observed features of geospace for quiet times and moderate storms, even with a passive outflow setting for the inner boundary of the MHD model.

In our previous study (*Trung et al.*, 2019), we performed multifluid MHD simulations of the magnetosphere with different outflow compositions under passive boundary conditions. We also applied two different IMF configurations. This was done to understand the contributions of the ionosphere relative to the solar wind in the magnetosphere. We used the concept of geopauses, a surface delineated by equal contributions of the solar wind to the ionosphere (*Moore*, 1991; *Moore and Delcourt*, 1995). For example, the pressure geopause is defined where the solar wind pressure is equal to the total ionospheric plasma pressure. We compared the mass density, number density, pressure geopauses, and magnetopause and found that no single boundary governed the transition from ionospheric dominated processes to solar wind dominated processes.

So far, no studies employing multifluid MHD have analyzed the relationship be-

tween the source terms appearing in the momentum equation on both solar wind and ionospheric plasmas. *Winglee* (1998) used a geopause analysis on multifluid MHD simulations to demonstrate numerically that the ionosphere was an influential source of plasma in magnetospheric dynamics. *Xu et al.* (2016) performed multifluid MHD simulations at Mars and applied the concept of geopauses to demonstrate that planetary ions dominated the lobes and the plasma sheet. *Trung et al.* (2019) examined the location of the geopauses relative to each other and the last closed field line. These studies hint at the importance of the geopause as a indicator of a change in physical processes dominating the plasma dynamics, but a quantitative assessment of the relative contributions from various force terms has not been conducted.

In this study, we explore the relationship between the physical processes emerging from the use of multifluid MHD to the boundaries in steady state. Specifically, we compare the source terms of the multi-fluid momentum equation to the number density geopause, mass density geopause, pressure geopause, and magnetopause.

5.2 Methods

We simulate the magnetosphere using the Space Weather Modeling Framework (SWMF) (*Tóth et al.*, 2007). It links different models together in order to achieve robust numerical simulations with the most efficient use of computational resources possible.

The models used in this simulation are a global magnetospheric (GM) model with an ionospheric electrodynamics (IE) model. The global magnetospheric model is based on the Block Adaptive Tree Solar wind Roe-type Upwind Scheme (*Powell et al.*, 1999). The multifluid MHD version (*Glocer et al.*, 2009a) is used in this study to distinguish the plasma properties of the solar wind and ionospheric plasmas. The ionospheric electrodynamics model used is the Ridley Ionosphere Model (*Ridley and Liemohn*, 2002; *Ridley et al.*, 2004) which consists of a 2d height integrated electric

potential solver with the current density information provided by GM.

The multifluid MHD equations are discussed in depth by *Glocer et al.* (2009a). The multifluid MHD code has been well tested across planetary systems such as Earth (*Glocer et al.*, 2009a; *Ilie et al.*, 2013, 2015b), Mars (*Najib et al.*, 2011; *Xu et al.*, 2016), and Jupiter (*Rubin et al.*, 2015).

The main focus of this study is on the multifluid momentum equation,

$$\frac{\partial \rho_s \mathbf{u}_s}{\partial t} + \nabla \cdot (\rho_s \mathbf{u}_s \mathbf{u}_s + I p_s) = n_s q_s (\mathbf{u_s} - \mathbf{u}_+) \times \mathbf{B} + \frac{n_s q_s}{n_e e} (\mathbf{J} \times \mathbf{B} - \nabla p_e) + S_{\rho_s \mathbf{u}_s} \quad (5.1)$$

where ρ_s is the mass density, $\mathbf{u}_s$ is the bulk flow velocity, p_s is the pressure, q_s is the charge, n_s is the number density, u_+ is the charge averaged velocity defined as,

$$\mathbf{u}_+ = \frac{\sum_s q_s n_s \mathbf{u}_s}{e n_e} \quad (5.2)$$

e is the elementary charge, n_e is the electron charge and is found by summing over the plasma species (thanks to quasineutrality), p_e is the electron pressure, and $S_{\rho_s \mathbf{u}_s}$ is the friction term. It takes the form,

$$S_{\rho_s \mathbf{u}_s} = \frac{1}{\tau_c} \sum_{i \neq s} \min(\rho_s, \rho_i)(\mathbf{u}_i - \mathbf{u}_s) \left(\frac{\mid \mathbf{u}_s - \mathbf{u}_i \mid}{u_c} \right)^{\alpha_c} \quad (5.3)$$

τ_c, the cutoff time scale, is set to 1000 s. $\mathbf{u}_c$, the cutoff velocity, is set to 100 km/s. α_c, the cutoff exponent, is set to 2. The index i is the index denoting the other ion fluids. This term limits the relative velocity between plasma species.

The sources in the momentum equation are terms that cannot be cast in a divergence form (see *Powell et al.* (1999)). Those are the terms on the right hand side of the momentum equation. They are in order, the gyration term, the Hall and electron pressure gradient terms, and interspecies friction.

The inner boundary is set at 2.5 R_E. The density imposed at the surface acts as the ionospheric reservoir. The bulk radial velocity is set to 0 but a temperature is specified, allowing upward diffusion into regions of nonzero radial velocity. The tangential velocity is computed from the electric potential calculated by the Ridley Ionospheric model. The inner boundary conditions are summarized in Table 5.1.

The outer boundary (X = 32 R_E) is the source of heliospheric plasma into the magnetosphere. Across all of the simulations in the study, the solar wind has a X-velocity of -450 km/s, a mass density of 8.7 amu/cm^3, a temperature of 1.2 $\times$ 10^5 K, and a magnetic field magnitude of 10 nT. The two possible magnetic field configurations used in this simulation are a southward IMF and a northward IMF. The solar wind does not have x and y components for the magnetic field in our simulation set. With the two plasma cases and the two IMF settings, four simulation results will be discussed in the following sections.

Table 5.1: Inner boundary conditions

	Case 1	Case 2
# of fluids	2	2
MHD Fluids	Solar Wind H^+ Ionospheric H^+	Solar Wind H^+ O^+
% Composition by Number	100 % Iono H^+	100 % O^+
Total Number Density [/cm^3]	28	28
Total Mass Density [amu/cm^3]	28	448
Ion Temperature [10^4 K]	2.5	2.5

5.3 Results

In this section, we present our post processed computations of the gyration, bulk (Hall and electron pressure gradient), and friction terms. The plots of the simulation are shown at the last time step, 12:00 UT, where the simulations are in steady state. The geopauses generated in our previous study (*Trung et al.*, 2019) are also drawn alongside the source terms.

In order to distinguish possible structures, the source terms are plotted on a symmetric logarithmic scale. The bulk terms and the gyration terms are plotted on a scale ranging from -10^7 to 10^7 amu/cm^2/sec^2. The linear scale is applied between -10^4 and 10^4 amu/cm^2/sec^2 to include possible 0 values. The symmetric logarithmic scales are applied from -10^4 to -10^7 amu/cm^2/sec^2 and 10^4 to 10^7 amu/cm^2/sec^2. The interspecies friction term has logarithmic scaling from -10^2 to -10^5 amu/cm^2/sec^2 and 10^2 to 10^5 amu/cm^2/sec^2. The linear scaling is from -10^2 to 10^2 amu/cm^2/sec^2. Despite these different ranges, the colorscales are carefully set to that the same colors correspond to the same force density values in all of the plots.

Additionally, we compared the momentum sources relative to each other within each plasma species. The calculation was done by taking the absolute value of each force density term and dividing it by the sum of the absolute value of the force density terms. This limits the possible range of values for the ratios from 0 to 1. However because it is possible that some of the larger terms are oppositely directed, it is possible that this ratio calculation can either underestimate or overestimate the influence of each force density term.

5.3.1 Case 1: Hydrogen only ionosphere, Northward IMF

For this case, both the solar wind and the ionospheric plasma are only composed of hydrogen. The IMF is northward and the magnetosphere is in steady state. Both mass density and number density geopauses are the same.

5.3.1.1 Ionospheric hydrogen

In Fig. 5.1, we plot the gyration, bulk term, and the friction terms applied to the ionospheric hydrogen in the meridional plane (X-Z). The components plotted are along the X and Z directions, with the top row showing the x component of the force densities and the lower row showing the z component magnitudes.

In the northward IMF configuration, the gyration terms are prevalent within the magnetopause but also in some parts outside of the magnetopause (Fig. 5.1(a) & (d)). Within the number density geopause, the gyration terms drive the ionospheric plasma sunward in the x-direction and away from the equator in the z-direction. Between the number density geopause and the magnetopause, the gyration terms direct the ionospheric plasma antisunward and away from the Sun Earth line. Outside of the magnetopause, the gyration terms transport the ionospheric plasma antisunward.

The bulk terms (Fig. 5.1(b) & (e)) acting on the ionospheric plasma are mostly confined within the magnetopause (cyan line). The friction acts on the ionospheric hydrogen along the nightside magnetopause, and outside of the magnetopause well beyond $X < -30\ R_E$. Parts of the magnetopause are close to regions where gyration and bulk terms change signs.

The nightside lobe structures with the bulk terms and the gyration terms in the x-direction seem to be associated with the shape of mass/number density (purple line, see Fig. 5.1 (a) and (b)). Within the number geopause, the x-components of the gyration and bulk terms have a magnitude of about 10^5 amu/cm^2/sec^2. Immediately outside of the number density geopause, the x-components of the gyration and bulk terms come close to zero. The friction force densities are also small.

We compared each force density to the sum of the force density magnitudes in Fig. 5.2. For the ratio of the bulk terms, one very distinct structure is a sea of yellow for the bulk term in the dayside (Fig. 5.2 (b) & (e)) represeenting a value close to 1. This indicates that the bulk terms dominate the motion of ionospheric plasma. However, in these regions, the bulk forces acting on the ionospheric plasma are very small due to the lack of ionospheric material beyond the dayside magnetopause (see Fig. 5.1 (b) and (e)). Thus, those features can be ignored.

With those ratio calculations, we can see that the friction terms (Fig. 5.2 (c) & (f)) have an influence on ionospheric hydrogen along a small part of the nightside

magnetopause at high latitudes (ratios between 0.5 and 1). Outside of the magnetopause beyond $X < -30\ R_E$ and $|Z| > 20\ R_E$, the friction terms have absolute ratios ranging from 0.2 to 0.6.

Within the magnetopause, the bulk terms have ratios close to 0.6 while the gyration terms (Fig 5.1 (a) and (d)) have ratios close to 0.4. Referring back to Fig. 5.1, this indicates that the bulk terms and gyration terms act in opposite directions and that the bulk terms are slightly stronger than the gyration terms.

Outside of the nightside magnetopause, at high latitudes, the gyration forces have a greater effect on the ionospheric plasma compared to the friction terms while the bulk terms do not play a significant role. Close to the equator and outside the magnetopause, the bulk terms dictate the transport of ionospheric hydrogen.

5.3.1.2 Solar wind hydrogen

The gyration terms (Fig. 5.3 (a) & (d)) influence the motion of the heliospheric plasma within the magnetopause while the friction (Fig. 5.3 (c) & (f)) displays a profile with colors opposite to the ionospheric one which is expected from the friction formula. The bulk terms (Fig. 5.3 (b) & (e)) for the heliospheric plasma are dominant in a larger volume than the ionospheric plasma. In these regions, ionospheric plasma cannot reach these regions due to the lack of ionospheric outflow so the force density is dominated by the single-fluid nature of these terms.

The nightside magnetopause is coincident with some regions where the bulk terms and the gyration terms change signs. The nightside mass density (and number density) geopause shape seem to be associated with the gyration and bulk terms in the X-direction in this particular case ($X \sim -10\ R_E$).

Looking at the force density ratios for the solar wind (Fig. 5.4), the gyration terms are a limited contributor to the solar wind motion within the magnetopause. The bulk terms dominate everywhere except within the mass density geopause. Within

the mass density geopause, the gyration terms dominate.

The friction terms play a minor role in affecting the motion of the solar wind. The only parts where the friction terms become significant are along the nightside magnetopause for the x-component and outside of the magnetopause.

The pressure geopause does not play a role because there is little ionospheric outflow due to northward IMF.

5.3.2 Case 2: Oxygen only ionosphere, Northward IMF

We examine the case where the ionosphere is only composed of oxygen while keeping the same inner boundary number density of 28 cm^{-3} but now with a much larger mass density.

5.3.2.1 Ionospheric oxygen

The gyration terms act on the ionospheric oxygen in a larger volume compared to the hydrogen only ionosphere (Fig. 5.5 (a) & (d)). In this outflow configuration, the nightside magnetopause overlaps with a regions where the gyration x-components transition from positive to negative. Above and below $Z = 0$ in the nightside, the structure of the gyration terms in the z-direction is not unidirectional. The number density geopause (in green) touches the parts where the z-direction gyration changes signs.

Similar to the hydrogen only ionosphere, the bulk terms acting on ionospheric oxygen are still only significant within the magnetopause. This is because the bulk terms are dependent on the ratio of the number density of the ionospheric plasma to the total plasma number density.

Akin to the ionospheric hydrogen case, the friction terms on the ionospheric oxygen are significant outside of the magnetopause and the mass density geopause. Friction has more influence on the ionospheric oxygen simulation than the ionospheric

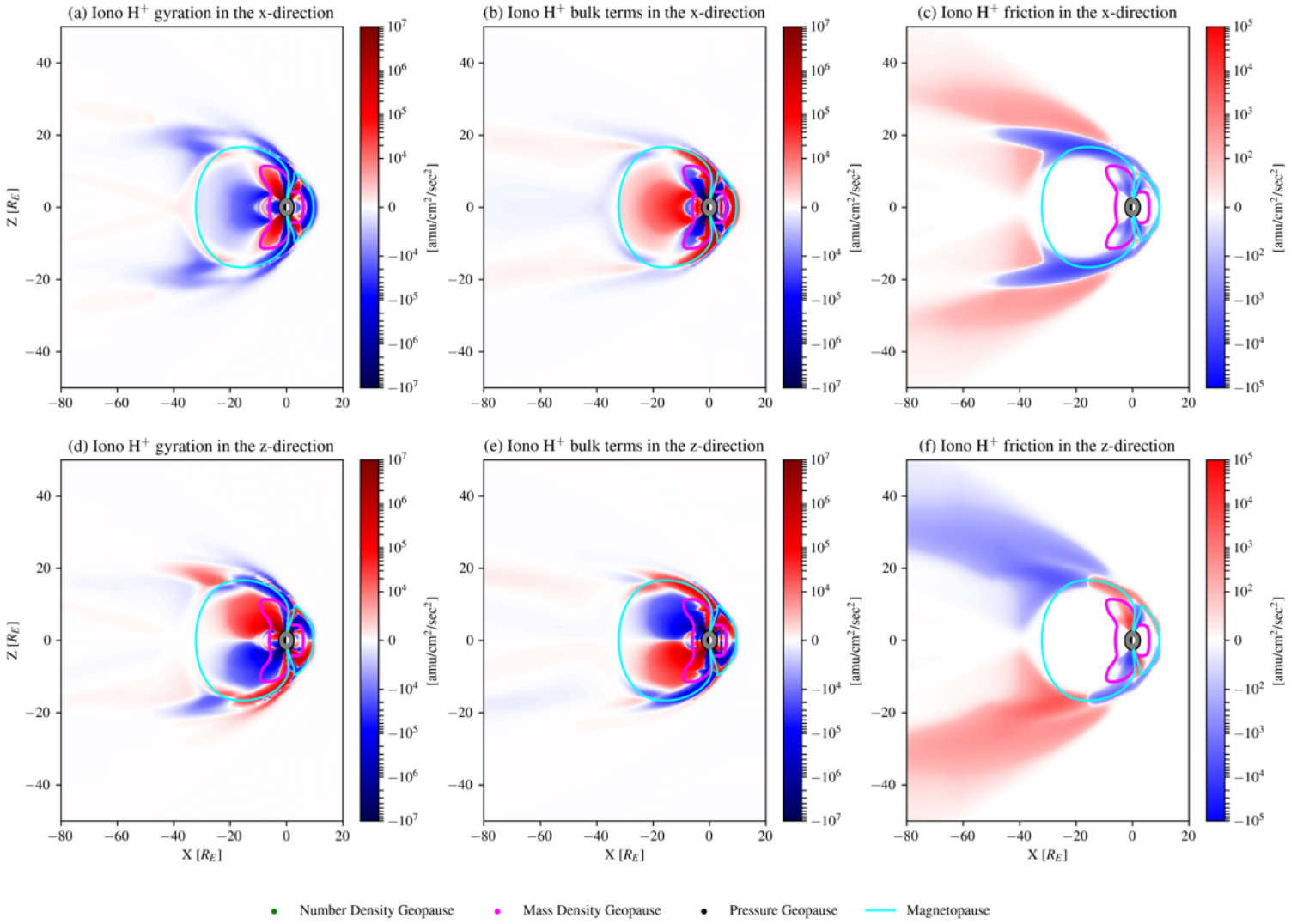

Figure 5.1: Force densities of ionospheric hydrogen for the simulation of solar wind hydrogen with ionospheric hydrogen during northward IMF. Top row: X-component of the gyration force density (a), bulk terms (b), and friction (c). Bottom row: Z-component of the gyration force density (d), bulk terms (e), and friction (f)

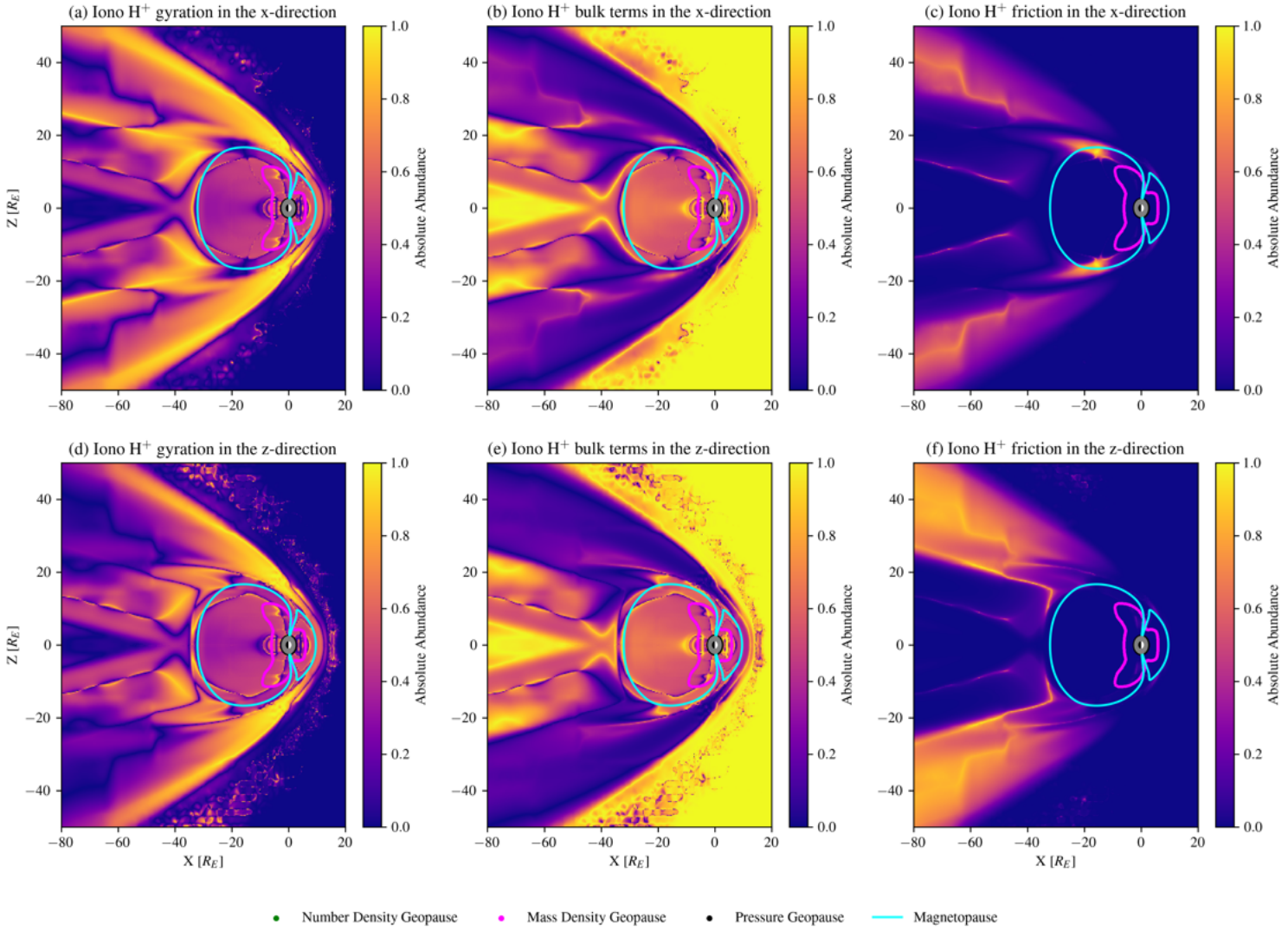

Figure 5.2: Force densities ratios of ionospheric hydrogen for the simulation of solar wind hydrogen with ionospheric hydrogen during northward IMF. Top row: X-component of the gyration force density (a), bulk terms (b), and friction (c). Bottom row: Z-component of the gyration force density (d), bulk terms (e), and friction (f)

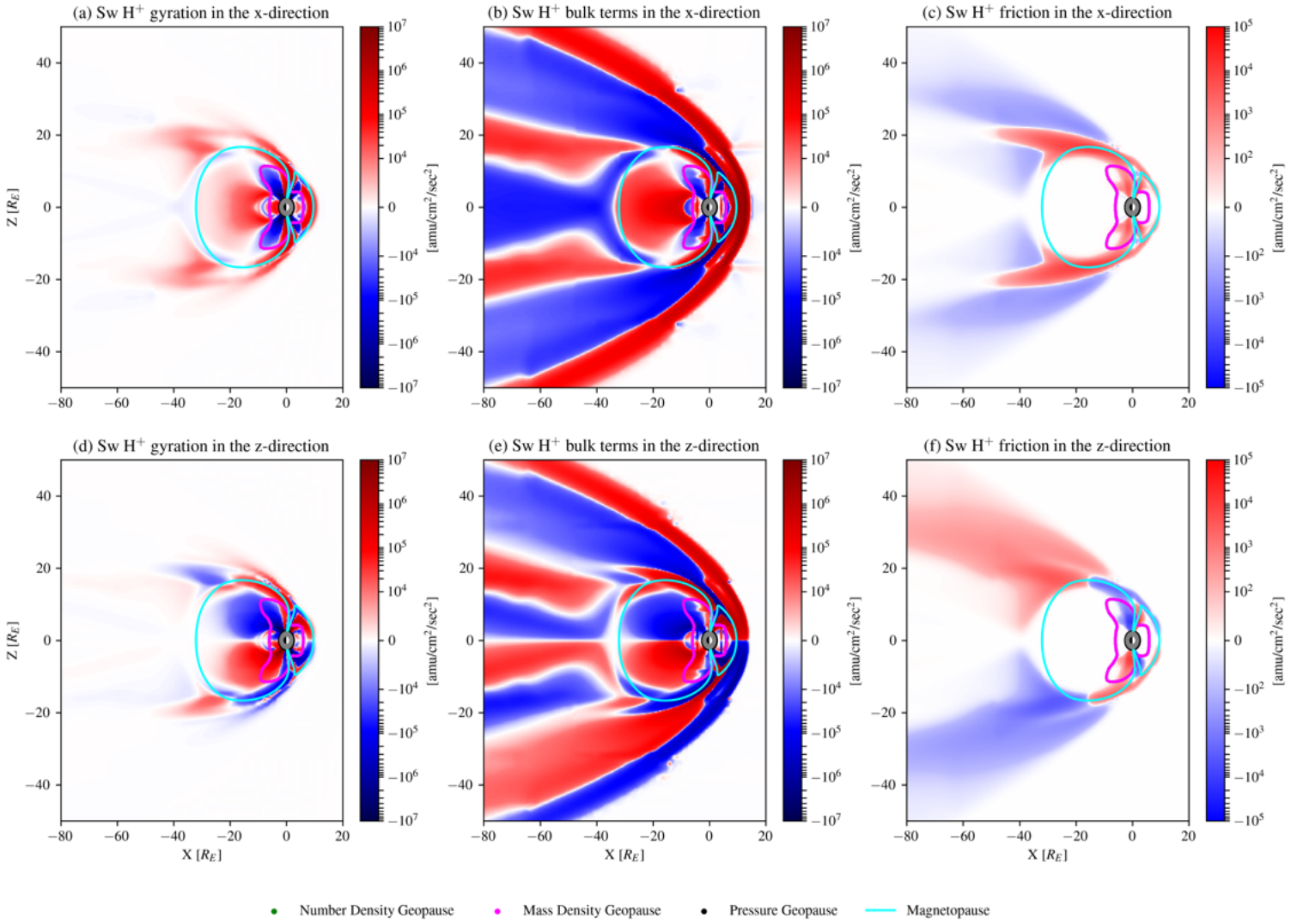

Figure 5.3: Force densities of solar wind hydrogen for the simulation of solar wind hydrogen with ionospheric hydrogen during northward IMF. Top row: X-component of the gyration force density (a), bulk terms (b), and friction (c). Bottom row: Z-component of the gyration force density (d), bulk terms (e), and friction (f)

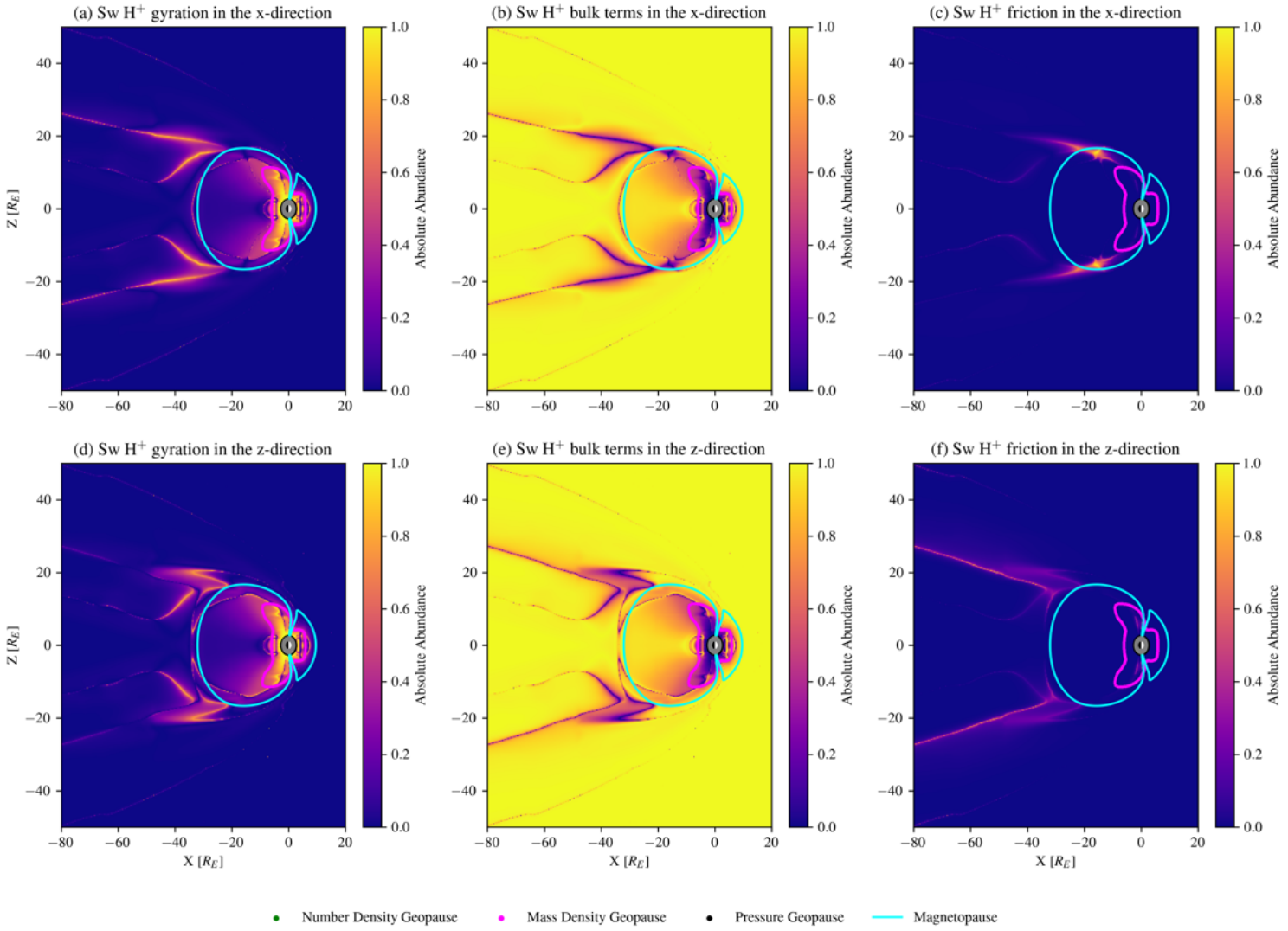

Figure 5.4: Force densities ratios of solar wind hydrogen for the simulation of solar wind hydrogen with ionospheric hydrogen during northward IMF. Top row: X-component of the gyration force density (a), bulk terms (b), and friction (c). Bottom row: Z-component of the gyration force density (d), bulk terms (e), and friction (f)

hydrogen simulation due to the dependence of mass density on the friction terms.

The mass density geopause matches some of the shape of the magnetopause and has additional wing like features emerging in regions around where the gyration, bulk, and friction terms change signs. The number density geopause is associated with features in the x-components of the gyration and bulk terms in regions where these terms undergo a significant change by multiple orders of magnitude.

Looking at the absolute ratios of the force terms for the ionospheric oxygen (Fig. 5.6), there are still the unusual structures appearing upstream of the bow shock. These would indicate that the gyration terms would dominate outside of the dayside magnetopause. However, the ionospheric oxygen number density in these regions is very small. Referring back to Fig. 5.6, these regions do not have a significant influence on ionospheric oxygen through gyration or bulk forces.

Fig. 5.6 (a) & (d) shows that the wingtips of the mass density geopause are close to regions where the ionospheric force densities are dominated by the gyration terms.

5.3.2.2 Solar wind hydrogen

An examination of the force densities applied on the solar wind hydrogen (Fig. 5.7) reveals that the nightside magnetopause delineates a region where the x-component of the gyration changes polarity. The z-component of the gyration has a bidirectional pattern above and below $Z = 0$. The solar wind bulk terms are dominant beyond the magnetopause.

The number density geopause is also overlaps with the two small lobe structures seen at $X = -10\ R_E$ for the x component of the gyration and bulk terms (5.7 (a) & (b)). The wing tips seen for the mass density geopause are more apparent in the solar wind force densities. They are coincident in the regions where the gyration and bulk terms change signs. The force ratio calculations for the solar wind (Fig. 5.8) show that those wing tips are surrounded by structures where the gyration terms are

dominant. The number densities are supported by the gyration terms.

Similar to the ionospheric hydrogen outflow case, the pressure geopause does not play a significant role.

5.3.3 Case 1: Hydrogen only ionosphere, Southward IMF

In this case, we are examining the magnetosphere during southward IMF with a hydrogen only ionosphere. As a reminder, the mass density and number density geopauses are the same.

5.3.3.1 Ionospheric hydrogen

The force densities in the meridional plane for this case are plotted in Fig. 5.9.

On the nightside, the gyration terms in the x-direction within the pressure geopause have a magnitude of about 10^5 amu/cm^2/sec^2 and direct the ionospheric hydrogen antisunward. Outside of the pressure geopause, the gyration terms are fairly small. The z-component of the gyration terms have a magnitude of close to 10^5 amu/cm^2/sec^2 in the pressure geopause. Between the mass density geopause and the pressure geopause, the z-component of the gyration term drops by several orders of magnitude to values close to 0.

Outside of the mass density geopause at $X = 0$, $Z = 0$, the width of the tip coincides with the location of the white band structures associated with the gyration terms. Along $Z = 0$, the x-component of the gyration force is applied to the ionospheric hydrogen sunward, while above $Z = 5$ R_E and below $Z = -5$, the x-component of the gyration force is applied antisunward. The end of the nightside magnetopause ($X = -30$, $Z = 0$) R_E coincides with a region where the x-components of the gyration term and bulk terms go to 0.

The force density ratios for ionospheric hydrogen (Fig 5.10) show that within the mass density geopause the bulk terms dominate and that the gyration terms are

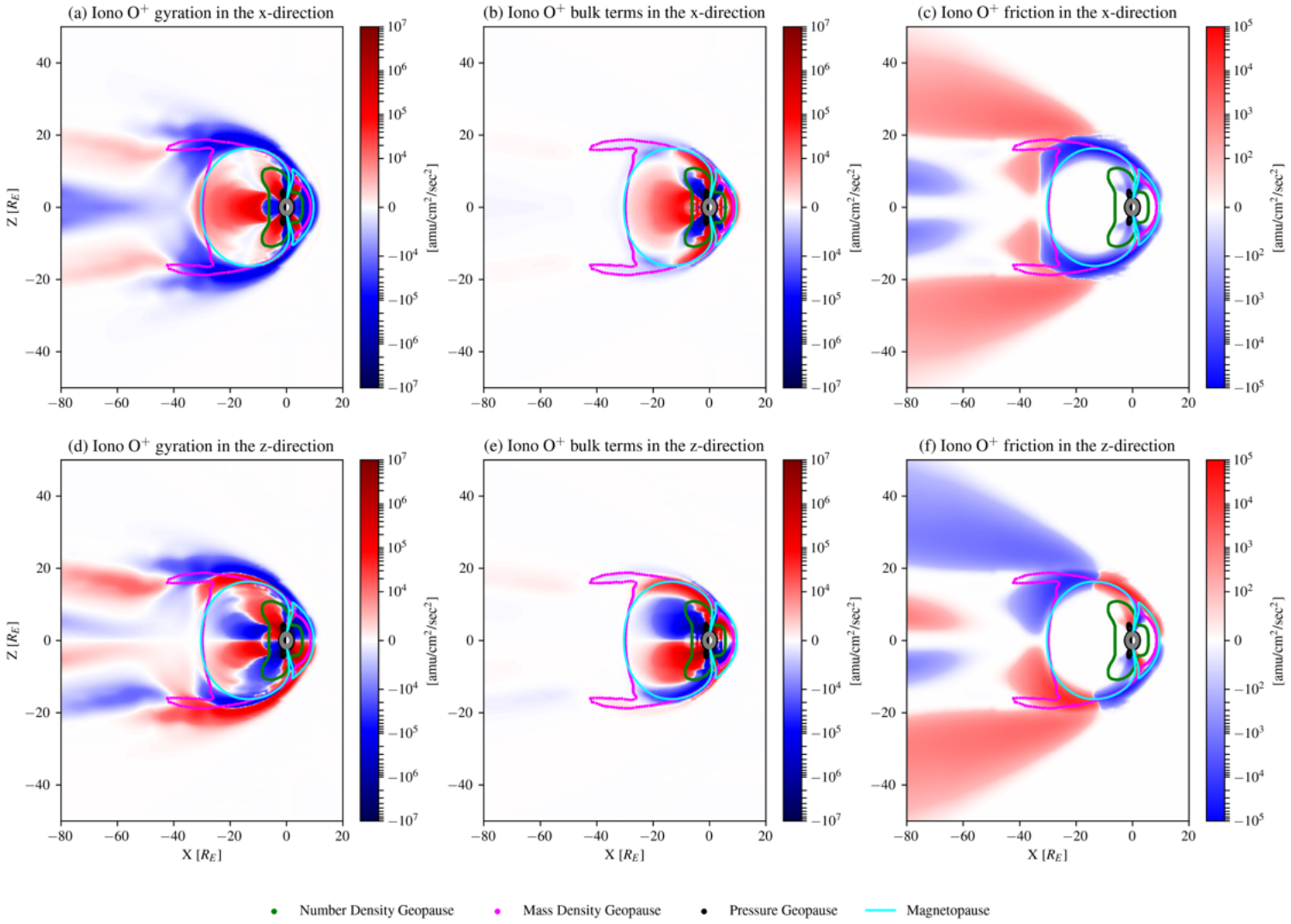

Figure 5.5: Force densities of ionospheric oxygen for the simulation of solar wind hydrogen with ionospheric oxygen during northward IMF. Top row: X-component of the gyration force density (a), bulk terms (b), and friction (c). Bottom row: Z-component of the gyration force density (d), bulk terms (e), and friction (f)

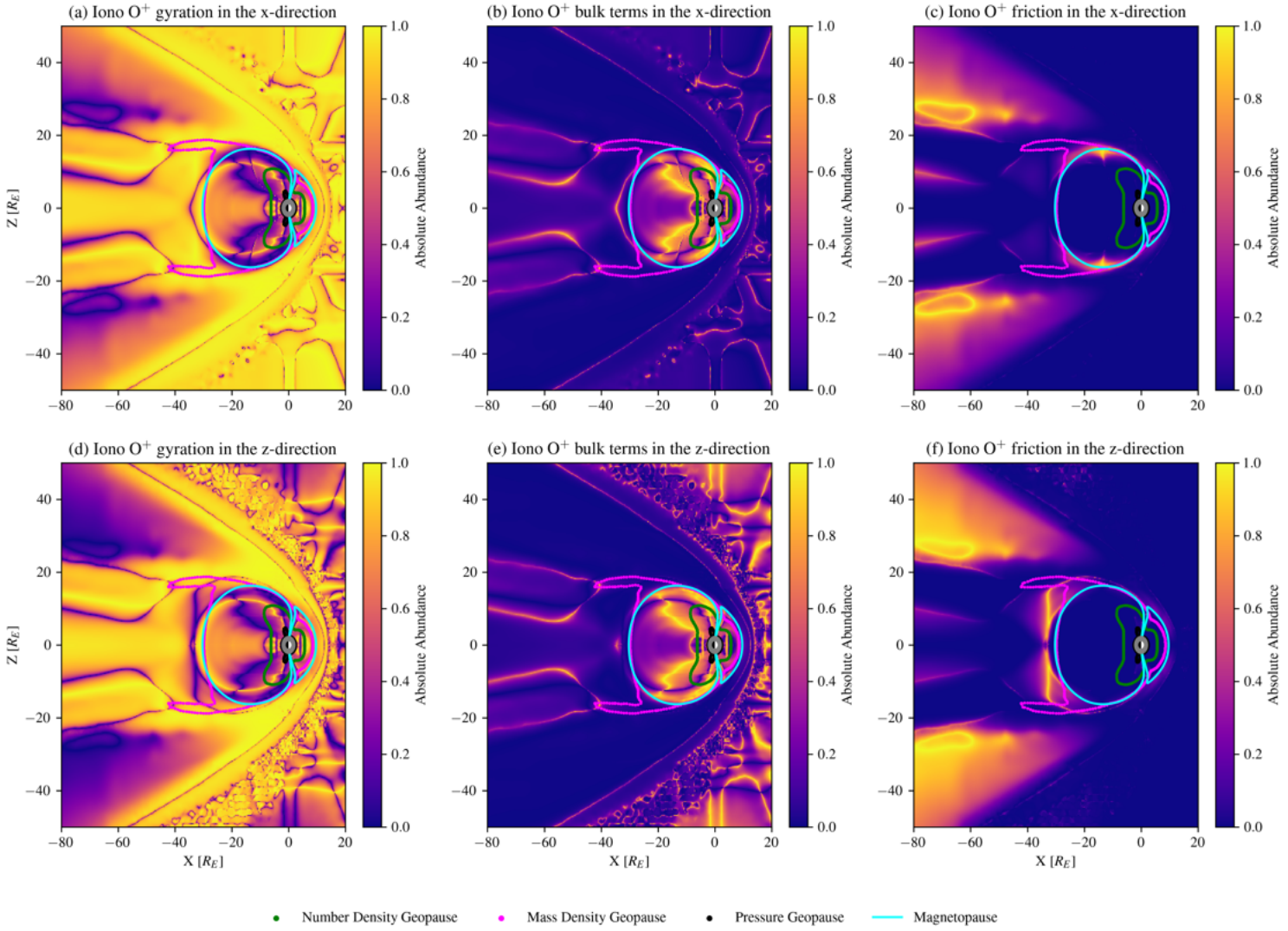

Figure 5.6: Force densities ratios of ionospheric oxygen for the simulation of solar wind hydrogen with ionospheric oxygen during northward IMF. Top row: X-component of the gyration force density (a), bulk terms (b), and friction (c). Bottom row: Z-component of the gyration force density (d), bulk terms (e), and friction (f)

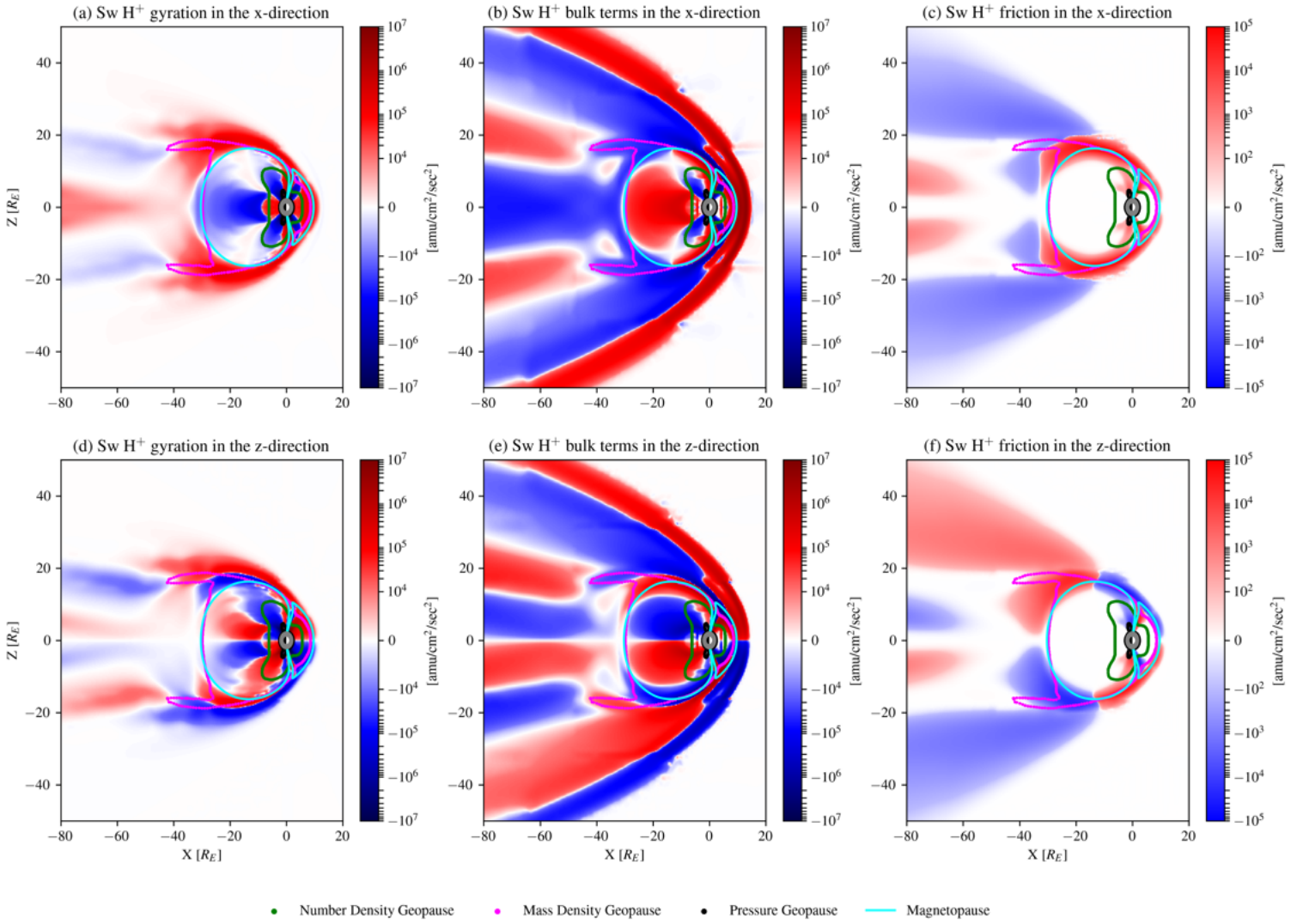

Figure 5.7: Force densities of solar wind hydrogen for the simulation of solar wind hydrogen with ionospheric oxygen during northward IMF. Top row: X-component of the gyration force density (a), bulk terms (b), and friction (c). Bottom row: Z-component of the gyration force density (d), bulk terms (e), and friction (f)

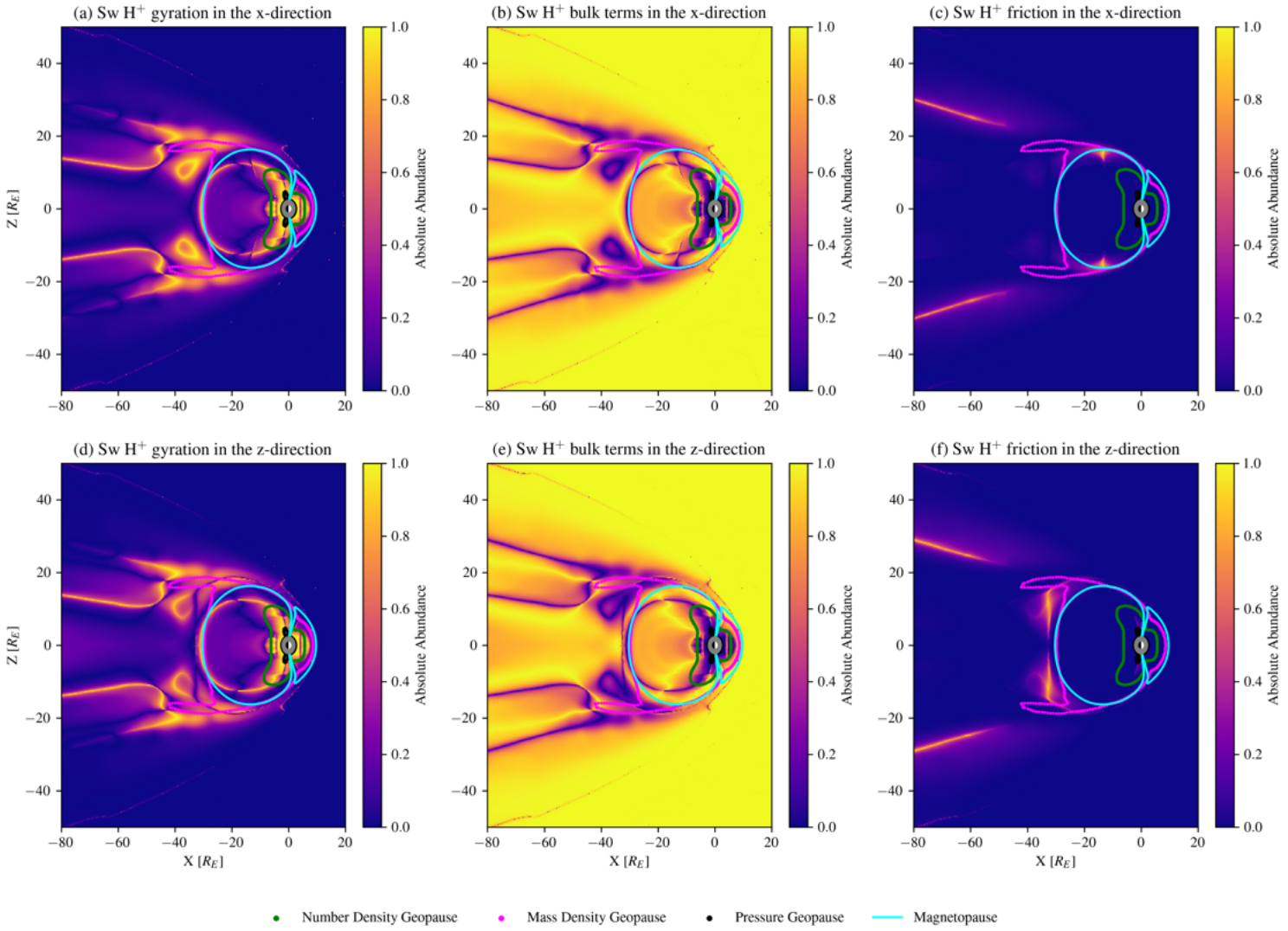

Figure 5.8: Force densities ratios of solar wind hydrogen for the simulation of solar wind hydrogen with ionospheric oxygen during northward IMF. Top row: X-component of the gyration force density (a), bulk terms (b), and friction (c). Bottom row: Z-component of the gyration force density (d), bulk terms (e), and friction (f)

a minor contributor to the motion of the ionospheric hydrogen. The jet structure outside of the mass density geopause is dominated by the bulk terms. The friction terms play a minor role in regulating the motion of the ionospheric hydrogen plasma at high latitudes. Again, the unusual structures appear upstream of the bow shock and are a numerical artifact resulting from the very low number density of ionospheric hydrogen.

5.3.3.2 Solar wind hydrogen

The gyration terms for the solar wind (Fig. 5.11 (a) & (d)) show colors opposite to the ionospheric hydrogen gyration terms. Similar to the ionospheric hydrogen gyration terms, the pressure density does outline a drop off in the magnitude of the gyration terms for the solar wind.

Within the nightside magnetopause, the gyration terms direct the solar wind earthward and towards the equator. Outside of it, the gyration terms direct the solar wind antisunward.

The bulk terms (Fig. 5.11 (b) & (e)) are more widespread throughout the magnetosphere. However, between the magnetopause and the mass geopause, the bulk terms are not acting significantly on the solar wind. Along the Sun-Earth line on the nightside, the bulk terms direct the solar wind in the same direction as the gyration terms.

Fig. 5.12 shows that for the solar wind, the friction does not play a major role in regulating solar wind motion compared to the other force density terms. The gyration dominates within the mass density geopause. The bulk terms dominate everywhere outside of the mass density geopause and within the magnetopause.

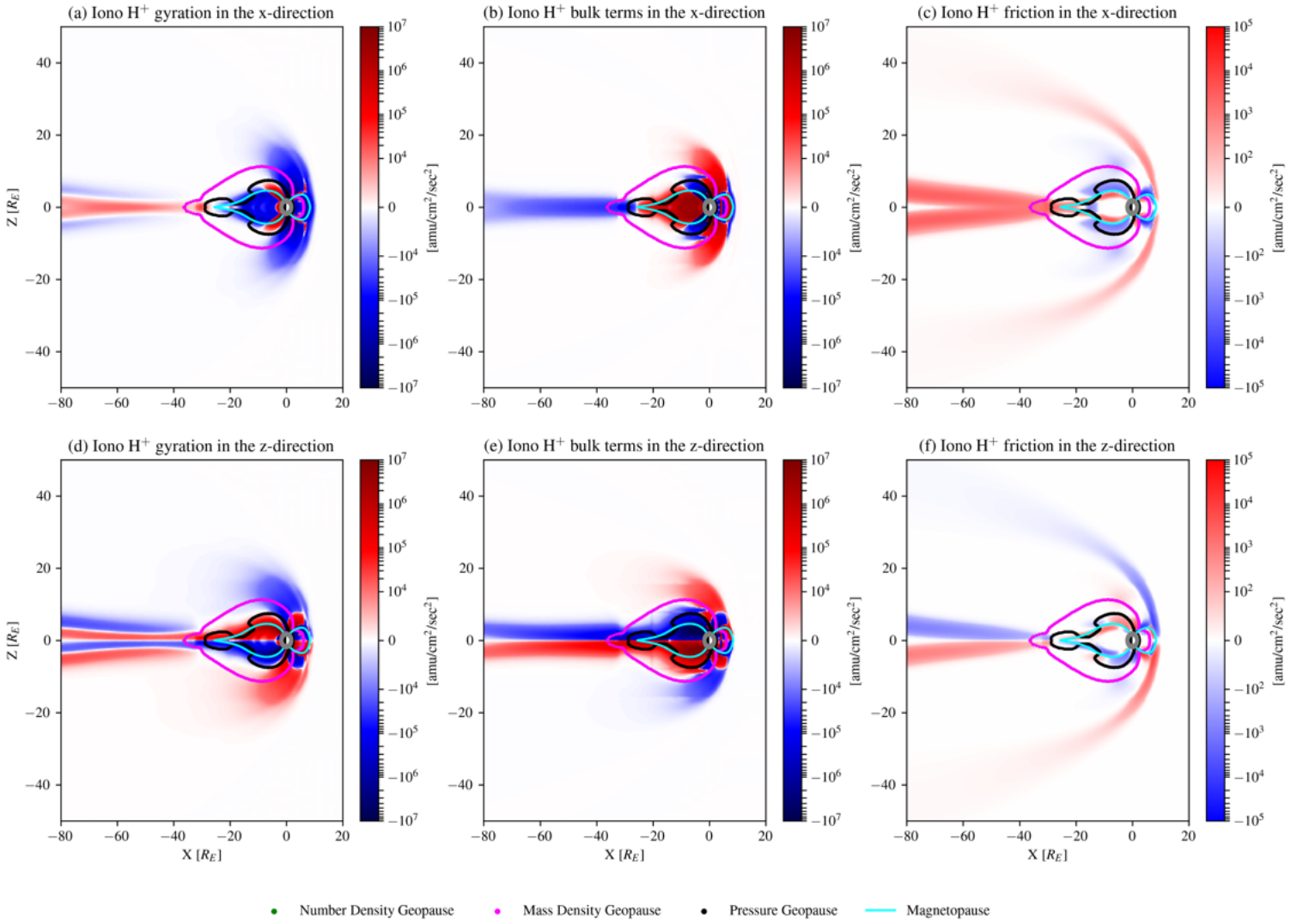

Figure 5.9: Force densities of ionospheric hydrogen for the simulation of solar wind hydrogen with ionospheric hydrogen during southward IMF. Top row: X-component of the gyration force density (a), bulk terms (b), and friction (c). Bottom row: Z-component of the gyration force density (d), bulk terms (e), and friction (f)

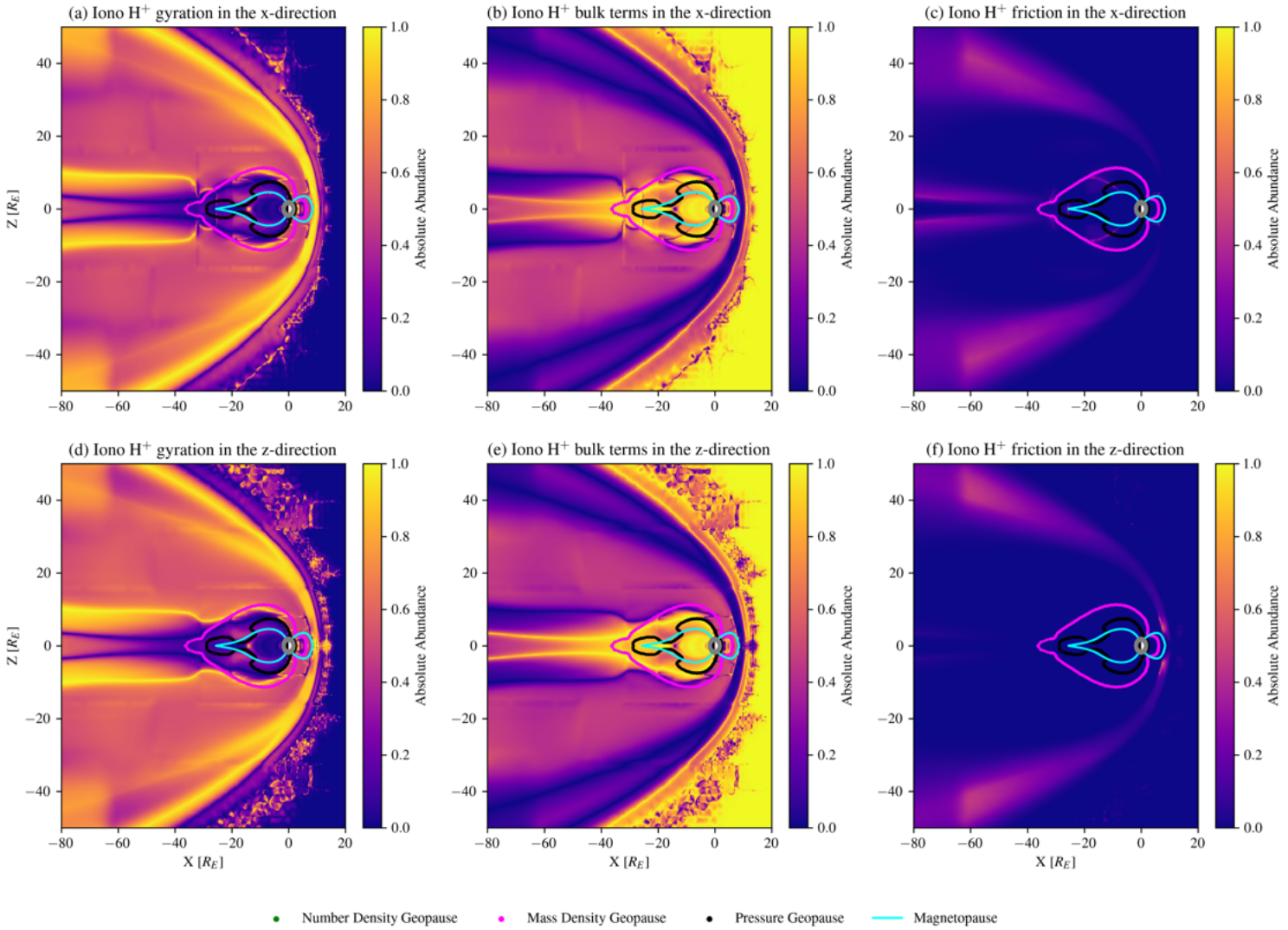

Figure 5.10: Force densities ratios of ionospheric hydrogen for the simulation of solar wind hydrogen with ionospheric hydrogen during southward IMF. Top row: X-component of the gyration force density (a), bulk terms (b), and friction (c). Bottom row: Z-component of the gyration force density (d), bulk terms (e), and friction (f)

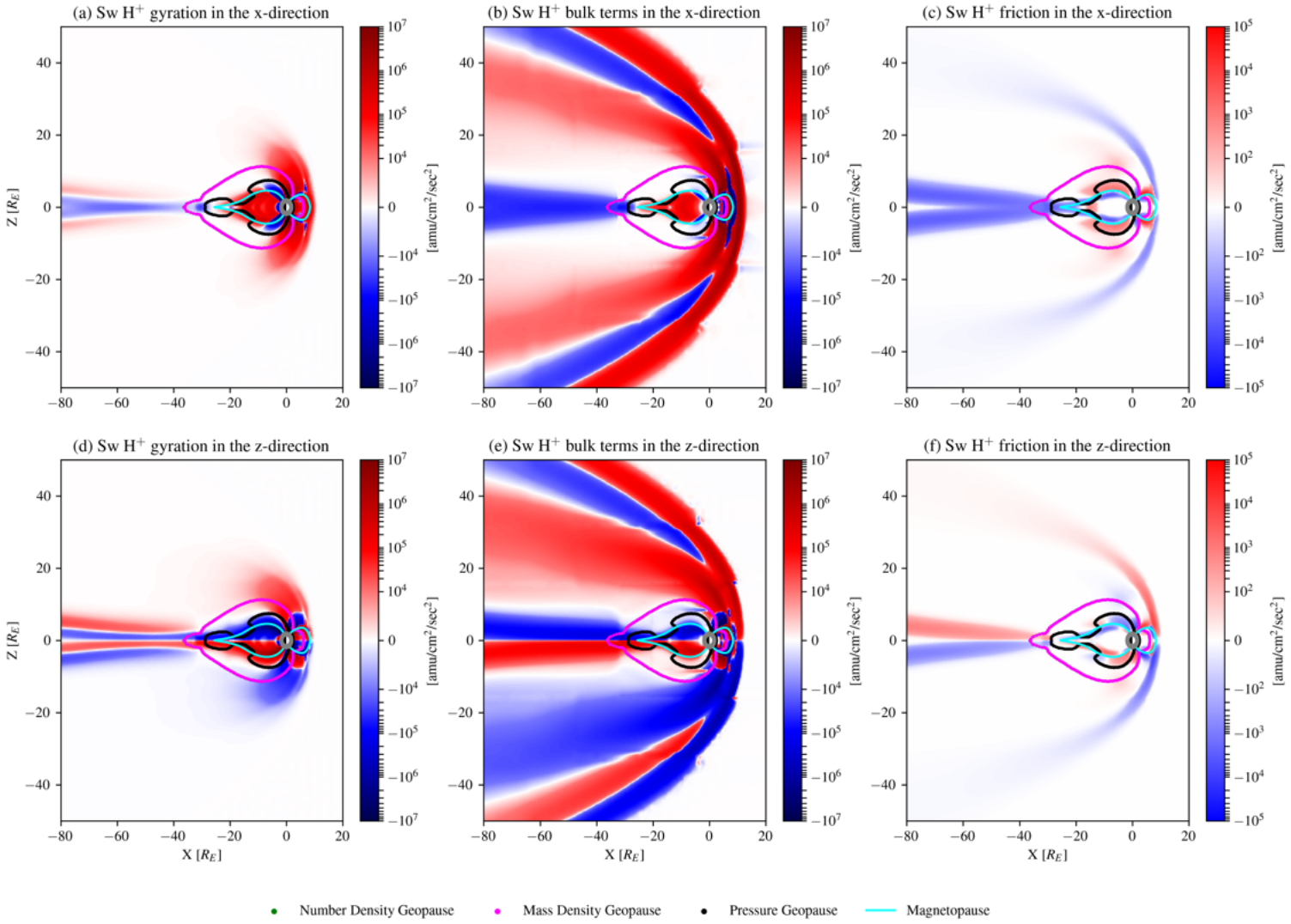

Figure 5.11: Force densities of solar wind hydrogen for the simulation of solar wind hydrogen with ionospheric hydrogen during southward IMF. Top row: X-component of the gyration force density (a), bulk terms (b), and friction (c). Bottom row: Z-component of the gyration force density (d), bulk terms (e), and friction (f)

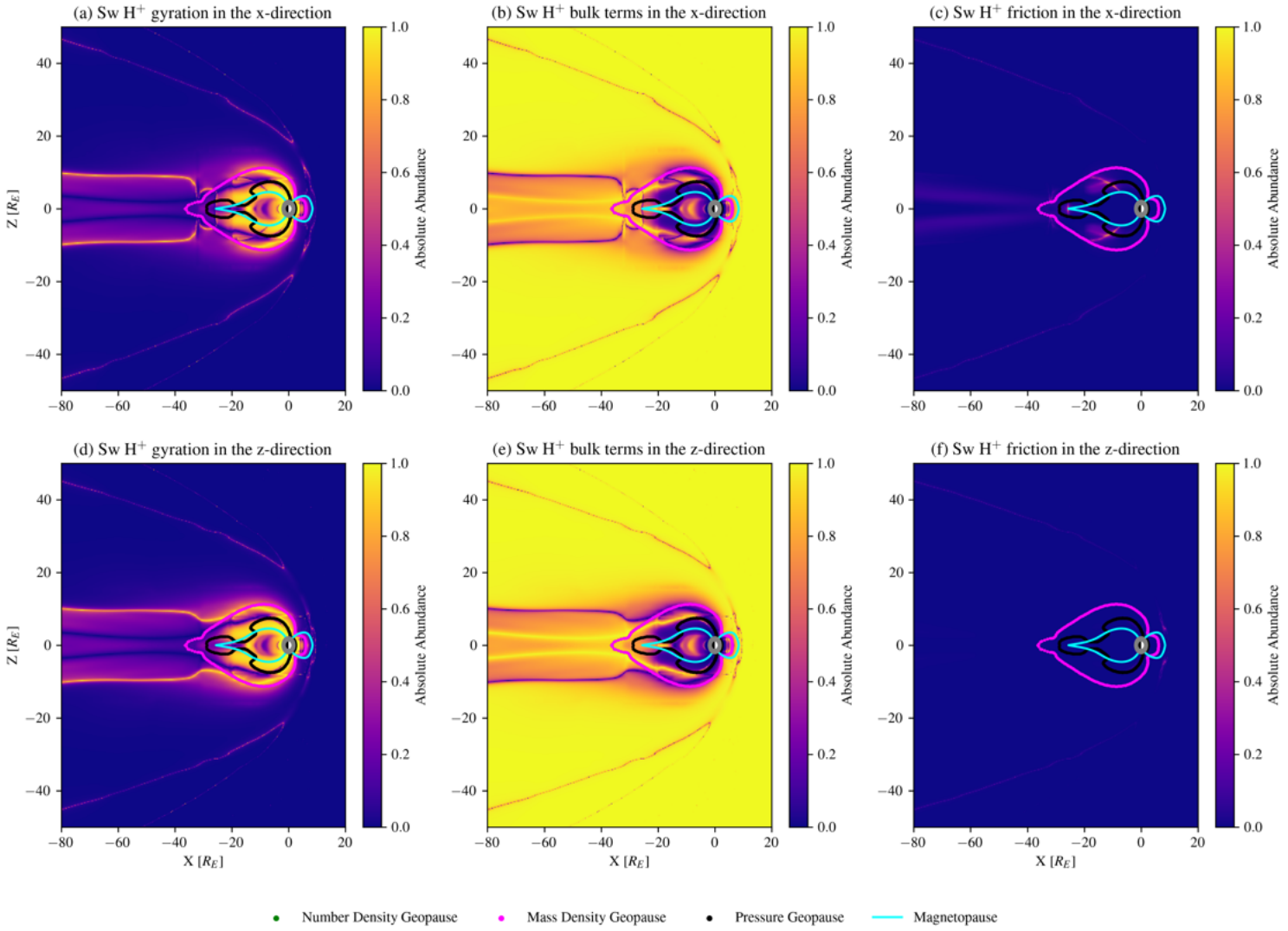

Figure 5.12: Force densities ratios of solar wind hydrogen for the simulation of solar wind hydrogen with ionospheric hydrogen during southward IMF. Top row: X-component of the gyration force density (a), bulk terms (b), and friction (c). Bottom row: Z-component of the gyration force density (d), bulk terms (e), and friction (f)

5.3.4 Case 2: Oxygen only ionosphere, Southward IMF

The last configuration that we are presenting is the oxygen only ionosphere under a southward IMF.

5.3.4.1 Ionospheric oxygen

For the ionospheric oxygen (Fig. 5.13), the gyration term along the x-direction is directed antisunward. The bulk terms in the x-direction are also directed antisunward. In the z-direction, both bulk and gyration terms direct the ionospheric oxygen towards the equator.

In the nightside along the Sun-Earth line, the location where the bulk terms in the X-direction and the X and Z components of the gyration terms approach zero ($X \sim -15\ R_E$) coincide with the end of the nightside magnetopause. Beyond the nightside magnetopause, the width of the pressure geopause is close to the width of the z-component gyration structure for oxygen.

The friction terms act to accelerate the ionospheric oxygen along the mass density geopause and to direct the ionospheric plasma earthward. However, they are too small to play a significant role in the transport of ionospheric oxygen.

When comparing the force densities (Fig. 5.14), the gyration terms has a greater influence in the motion of the ionospheric oxygen outside of the nightside number density geopause. The bulk terms dominate inside of the number density geopause. Between the pressure geopause and the number density geopause, the gyration terms have a greater influence on the motion of the ionospheric oxygen compared to the bulk terms.

Also, the plot of the force densities indicate that the gyration term is very dominant in the dayside. However, when examining the values of the force densities, the gyration terms are fairly small. This makes sense since there is very little ionospheric oxygen outside of the dayside magnetopause.

5.3.4.2 Solar wind hydrogen

The gyration terms on the solar wind (Fig. 5.15) in the x-direction act to slow it down in the dayside. The gyration terms deflect the solar wind around Earth. Outside of the nightside magnetopause, gyration in the x-direction acts sunward. In the z-direction, gyration forces push the solar wind away from $Z = 0$.

In the nightside, the bulk terms will act in a direction opposite of the gyration terms. Outside of the nightside magnetopause, the bulk terms in the x-direction act in an antisunward direction while the bulk terms in the z-direction act to push the solar wind towards $Z = 0$.

The pressure geopause outside of the nightside magnetopause is overlapping with structures associated with the bulk terms and gyration terms in the z-direction.

The friction acting on the solar wind does not play a part in its motion (Fig. 5.16), the bulk terms logically play a role throughout the magnetosphere. Within the pressure geopause, the bulk terms are slightly larger than the gyration terms. In the immediate vicinity outside of the pressure geopause, the bulk terms are very small compared to the gyration terms.

The many findings from the two cases and two IMF orientations presented above are summarized in Tables 5.2– 5.5. For each model configuration, these tables list the two ion species (ionospheric and heliospheric origin) and the associated figures, and then for each of the three momentum equation right-hand-side force density terms, it lists the key features of the magnitude of that term and where that term is dominant relative to the other force densities. These tables provide a guide for understanding where each of the momentum equation terms are important across near-Earth space. It is seen that, quite often, one of the geopauses is the boundary for where a force density changes with respect to absolute or relative magnitude.

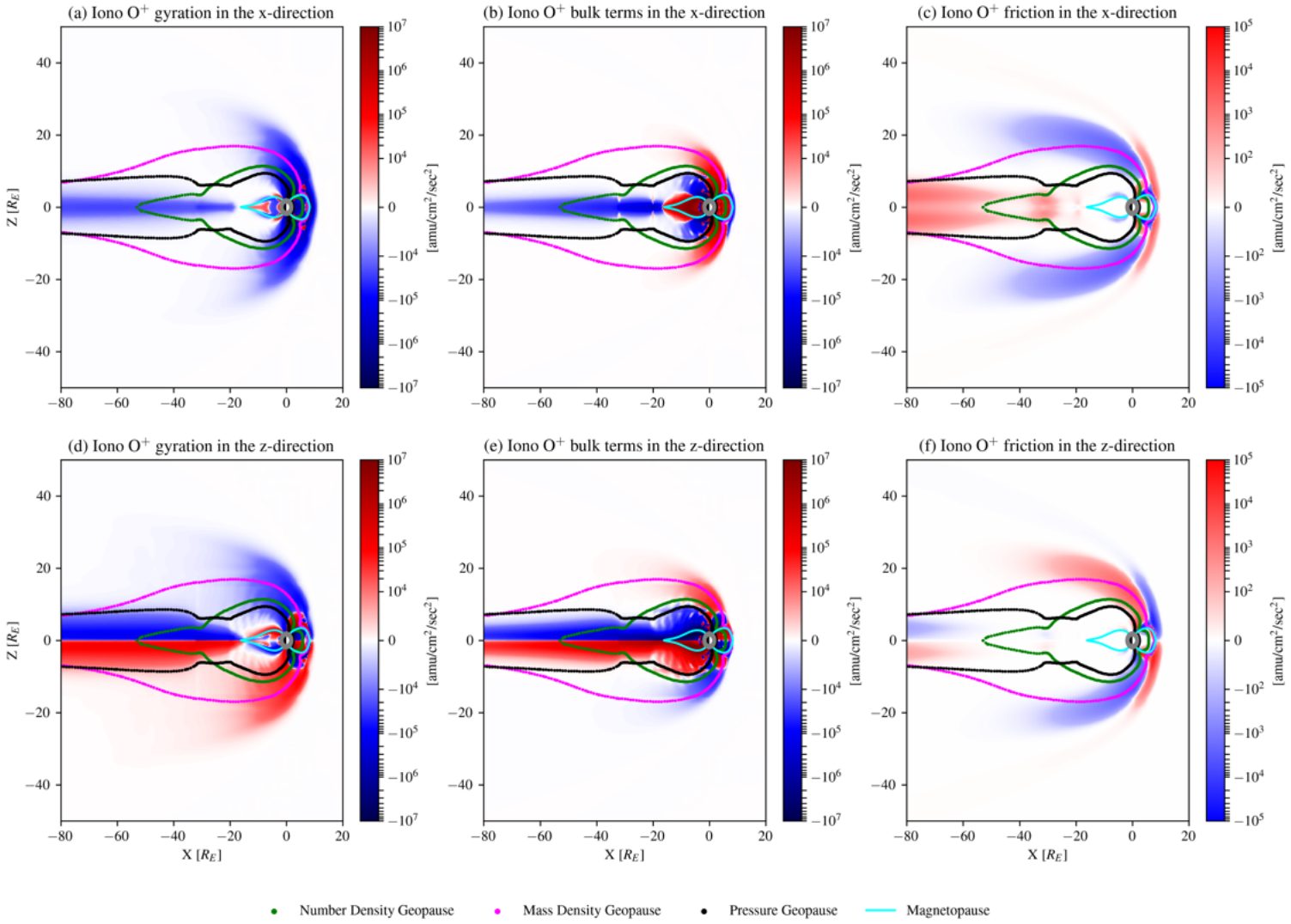

Figure 5.13: Force densities of ionospheric oxygen for the simulation of solar wind hydrogen with ionospheric hydrogen during southward IMF. Top row: X-component of the gyration force density (a), bulk terms (b), and friction (c). Bottom row: Z-component of the gyration force density (d), bulk terms (e), and friction (f)

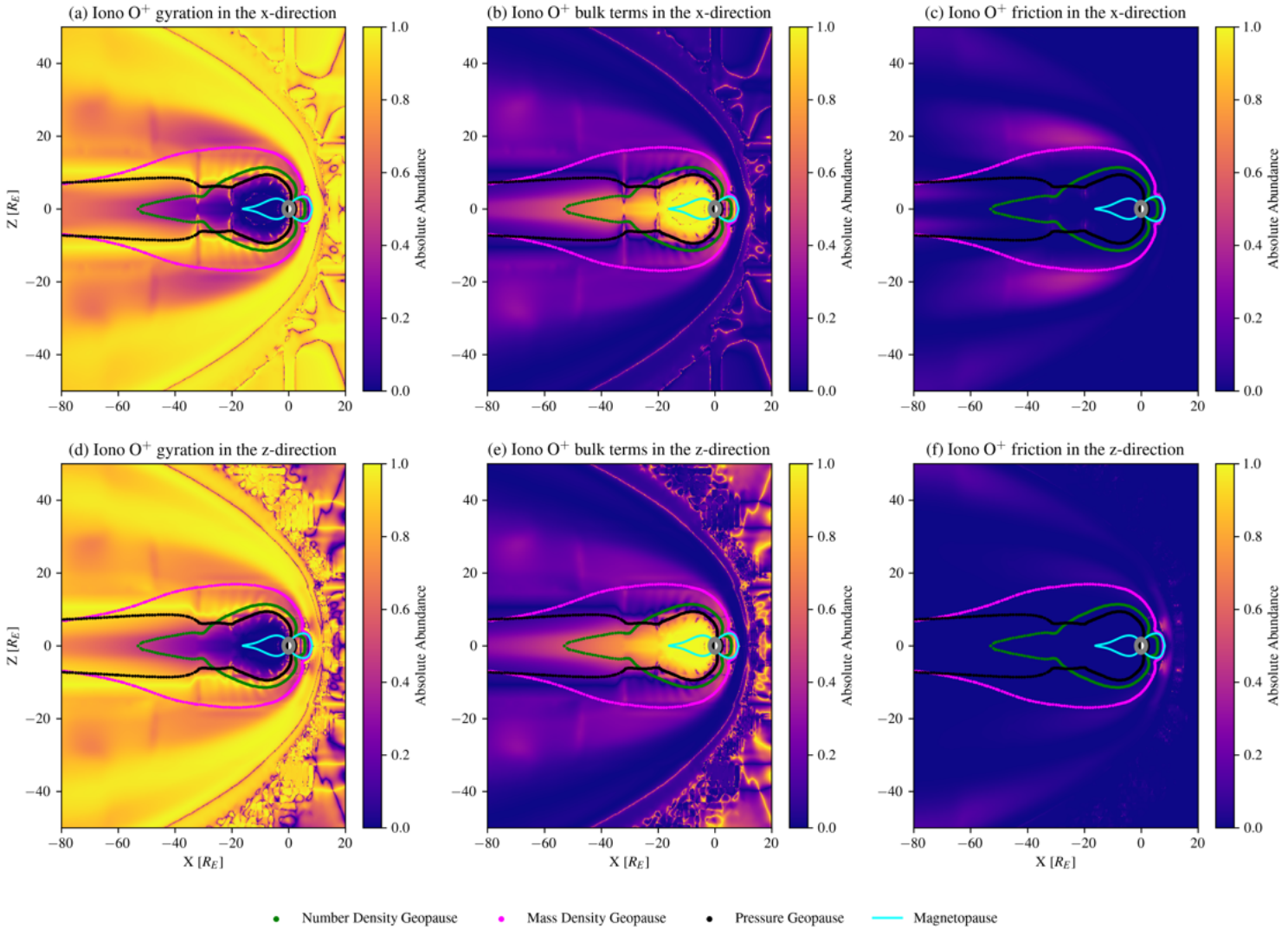

Figure 5.14: Force densities ratios of ionospheric oxygen for the simulation of solar wind hydrogen with ionospheric hydrogen during southward IMF. Top row: X-component of the gyration force density (a), bulk terms (b), and friction (c). Bottom row: Z-component of the gyration force density (d), bulk terms (e), and friction (f)

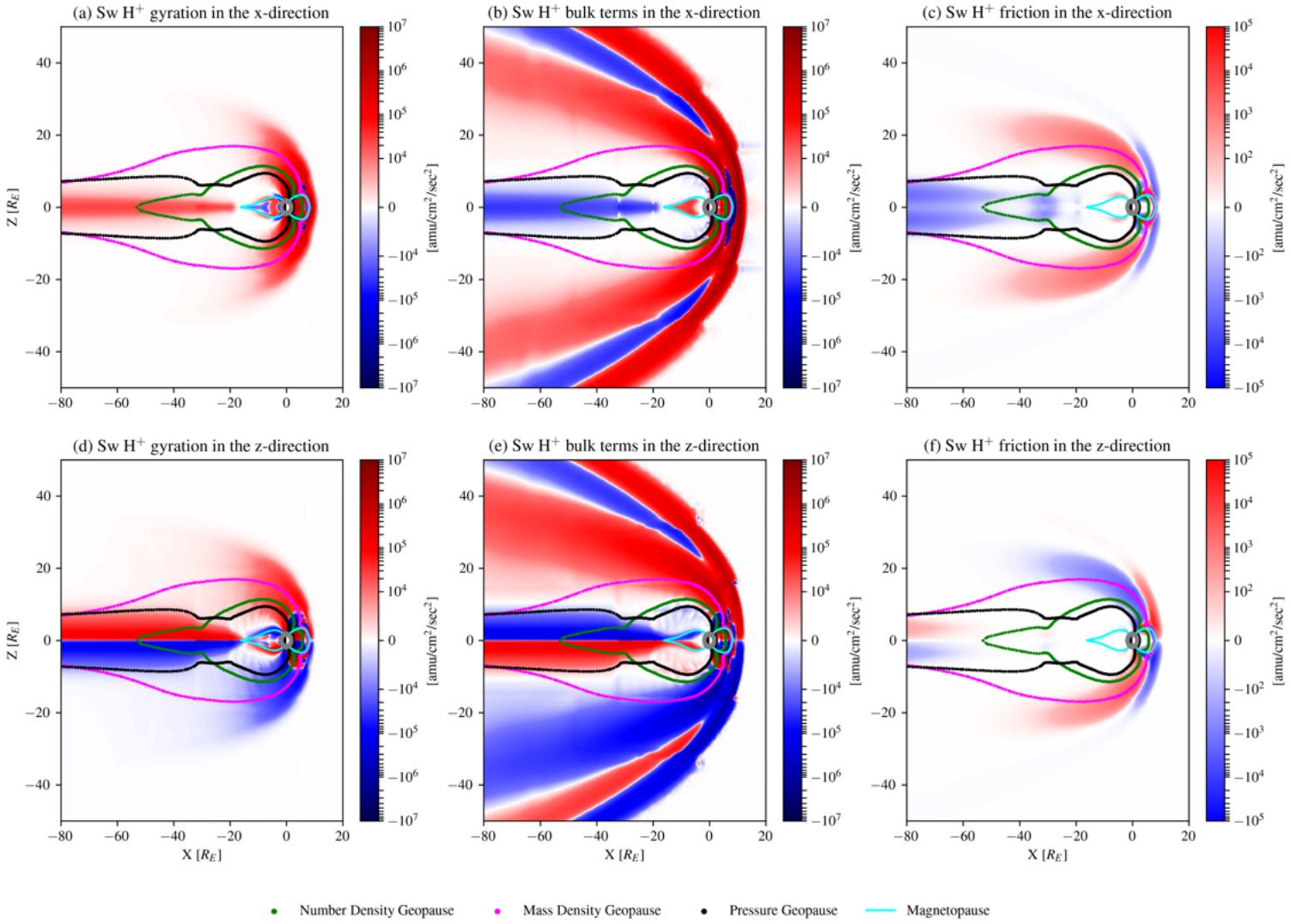

Figure 5.15: Force densities of solar wind hydrogen for the simulation of solar wind hydrogen with ionospheric hydrogen during southward IMF. Top row: X-component of the gyration force density (a), bulk terms (b), and friction (c). Bottom row: Z-component of the gyration force density (d), bulk terms (e), and friction (f)

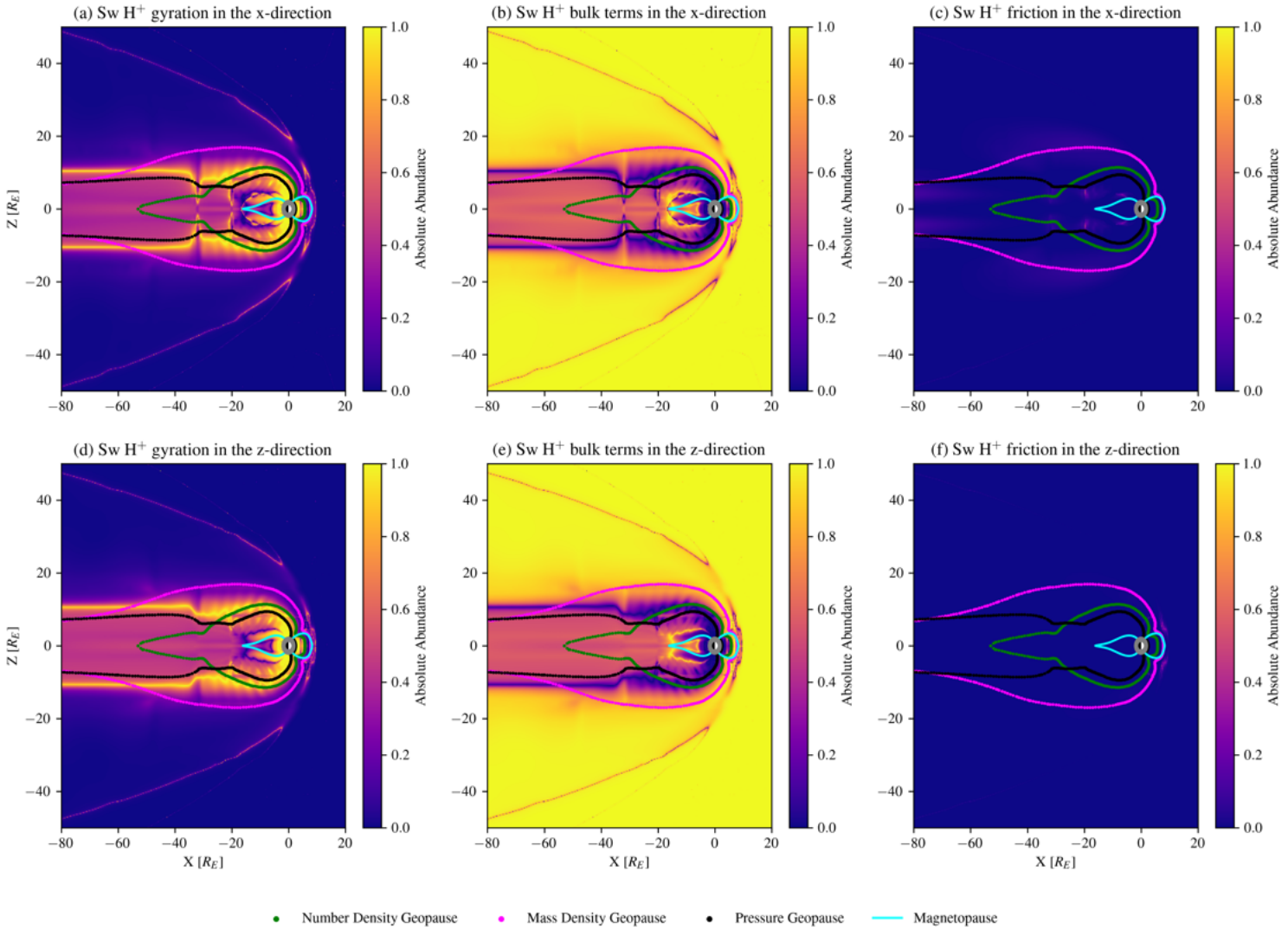

Figure 5.16: Force densities ratios of solar wind hydrogen for the simulation of solar wind hydrogen with ionospheric hydrogen during southward IMF. Top row: X-component of the gyration force density (a), bulk terms (b), and friction (c). Bottom row: Z-component of the gyration force density (d), bulk terms (e), and friction (f)

Table 5.2: Summary of results for Case 1 (ionospheric H^+) with northward IMF

	Figures	Term	Magnitude	Dominant?
Ionospheric H^+ during northward IMF	1 & 2	Gyration	Large inside density geopause, sign flip beyond this, large just beyond last closed field line	In dayside magnetosheath and just beyond nightside last closed field line
		Bulk	Same structure as gyration terms, but opposite sign nearly everywhere	Inside last closed field line and down central tail
		Friction	Large near and outside of last closed field line	In deep tail magnetosheath, and isolated spots near last closed field line
Heliospheric H^+ during northward IMF (with Iono H^+)	3 & 4	Gyration	Large inside density geopause, sign flip outside this, large just beyond last closed field line	Inside density geopause and just beyond nightside last closed field line
		Bulk	Large everywhere, sign flips at density geopause and last closed field line	Outside of density geopause
		Friction	Large near and outside of last closed field line	Small locations near last closed field line

5.4 Discussion

In the context of our simulations, the gyration term is simplified to a form dependent on the relative velocity between the ionospheric and heliospheric plasma. The charge averaged velocity takes the form,

$$\mathbf{u}_+ = \frac{n_{sw}\mathbf{u}_{sw} + n_{io}\mathbf{u}_{io}}{n_{sw} + n_{io}} \tag{5.4}$$

where the *io* and *sw* subscripts are abbreviations for ionospheric and solar wind. We can rewrite the gyration term for the solar wind to,

Table 5.3: Summary of Case 2 (ionospheric O^+) results with northward IMF

	Figures	Term	Magnitude	Dominant?
Ionospheric O^+ during northward IMF	5 & 6	Gyration	Large inside density geopause, sign flip at last closed field line, sign flip at wingtips of mass density geopause	Outside last closed field line
		Bulk	Large inside the mass density geopause	Inside last closed field line
		Friction	Large near and beyond the last closed field line	Small spots near mass density geopause, and deep tail magnetosheath
Heliospheric H^+ during northward IMF (with Iono O^+)	7 & 8	Gyration	Sharp gradient at density geopause, sign change at last closed field line and wingtips of mass density geopause	Inside density geopause and just beyond nightside last closed field line
		Bulk	Large everywhere, sign flips at density geopause and last closed field line	Outside of density geopause
		Friction	Large near and outside of last closed field line	Small locations near last closed field line

Table 5.4: Summary of Case 3 (ionospheric H^+) results with southward IMF

	Figures	Term	Magnitude	Dominant?
Ionospheric H^+ during southward IMF	9 & 10	Gyration	Large inside pressure geopause, in dayside magnetosheath, and down central tail	In magnetosheath
		Bulk	Same structure as gyration terms, opposite sign on dayside, same sign on nightside	Inside of density geopause and down central tail
		Friction	Outside of last closed field line	In deep tail magnetosheath
Heliospheric H^+ during southward IMF (with Iono H^+)	11 & 12	Gyration	Large inside pressure geopause, in dayside magnetosheath, and down central tail	Inside mass density geopause
		Bulk	Large everywhere, sometimes the same sign as gyration force	Outside of mass density geopause
		Friction	Large near and beyond last closed field line	Never dominant

Table 5.5: Summary of Case 4 (ionospheric O^+) results with southward IMF

	Figures	Term	Magnitude	Dominant?
Ionospheric O^+ during southward IMF	13 & 14	Gyration	Large inside pressure geopause, in dayside magnetosheath, and down central tail	Outside of density geopause
		Bulk	Same structure as gyration terms, opposite sign on dayside, same sign on nightside	Inside of density geopause
		Friction	Large outside of last closed field line, especially beyond density geopause	Small spots in midtail magnetosheath
Heliospheric H^+ during southward IMF (with Iono O^+)	15 & 16	Gyration	Large inside pressure geopause, in dayside magnetosheath, and down central tail	Thin region right outside of the pressure geopause
		Bulk	Large everywhere, sometimes the same sign as gyration force	Most locations, except near the pressure geopause
		Friction	Large outside of last closed field line, especially beyond density geopause	Never dominant

$$\mathbf{f}_{gyr,sw} = en_{sw}\frac{n_{io}}{n_{sw}+n_{io}}(\mathbf{u}_{sw}-\mathbf{u}_{io})\times\mathbf{B} \tag{5.5}$$

In this functional form, the gyration term for the solar wind takes a velocity dependence similar to friction (relative velocity between two fluids), albeit in a direction perpendicular to the velocity used in the friction term. The gyration term has an effective number density equal to half of the harmonic mean of the number density of the ionospheric and heliospheric plasma. If we examine the gyration term for the ionospheric plasma, it is found by switching places for the solar wind and ionospheric terms. This will give a form similar to the gyration term to the solar wind.

The gyration term for the solar wind and the ionospheric plasma are equal in magnitude but antiparallel. This can be seen in case 1 for Figs. 5.1 & 5.3 where the magnitudes of the gyration terms for the ionospheric plasma and the solar wind are equal in magnitude but they are directed in opposite directions as seen by the same structures and changing colors. This also holds for the other cases (see Figs. 5.5 & 5.7 for case 2, Figs. 5.9 & 5.11 for case 3, and Figs. 5.13 & 5.15 for case 4). This result is only valid for a two fluid plasma.

We can also rewrite the gyration term in the form of,

$$\mathbf{f}_{gyr,sw} = m_{sw}n_{sw}\nu_{io\to sw}(\mathbf{u}_{sw}-\mathbf{u}_{io})\times\hat{b} \tag{5.6}$$

where $\nu_{io\to sw}$ is the momentum transfer frequency due to gyration from the ionospheric plasma to the solar wind plasma, and $\hat{b}$ is a unit vector in the direction of the magnetic field. $\nu_{io\to sw}$ is defined as,

$$\nu_{io\to sw} = \frac{eB}{m_{sw}}\frac{n_{io}}{n_{sw}+n_{io}} \tag{5.7}$$

B is the magnitude of the magnetic field. The momentum transfer frequency for the solar wind becomes the gyrofrequency of the solar wind plasma when the

ionospheric number density is much larger than the solar wind number density.

If we take the ratio $\nu_{io \to sw}$ to $\nu_{sw \to io}$, we obtain the expression,

$$\frac{\nu_{io \to sw}}{\nu_{sw \to io}} = \frac{m_{io} n_{io}}{m_{sw} n_{sw}} \tag{5.8}$$

which is simply the ratio of the mass density of the ionospheric plasma to the mass density of the solar wind plasma.

At the mass density geopause, the momentum transfer frequency of the solar wind to the ionospheric plasma is equal to the momentum transfer frequency of the ionospheric plasma to the solar wind. Outside of the mass density geopause, gyration has a greater effect on transferring momentum from the solar wind plasma to the ionospheric plasma than from the solar wind plasma to the ionospheric plasma while the opposite occurs inside the mass density geopause.

The bulk terms are applied to both plasma species in the same direction. This is because the direction of the bulk terms is dictated by the cross product of the current density with the magnetic field and the electron pressure gradient. The strength of the bulk term for both species are dependent on the density multiplier. At the number density geopause, the bulk terms are equal in magnitude for both heliospheric and ionospheric plasmas.

An examination of the ratio plots for the solar wind tells us that friction is negligible in comparison to the gyration and the bulk terms in large regions of geospace for both IMF configurations. In the mantle regions far from the magnetopause during northward IMF, friction can dominate the ionospheric plasma. In those cases, friction pushes the ionospheric plasma towards the equator and earthward while the other force terms are weak in these regions. In these regions, this implies that the ionospheric plasma is moving at a higher speed than the solar wind plasma. The higher ionospheric plasma speeds are due to the gyration terms acting anti sunward along the magnetopause. In other words, gyration acts to accelerate the ionospheric

plasma anti sunward while decelerating the solar wind plasma.

As such, the ratio calculations can be approximated in most of geospace as a comparison between the bulk terms and the gyration terms. This ratio gives us an insight into the force terms dominating the plasma and their relationships to the geopauses.

During northward IMF, the ionospheric plasma's motion within the nightside magnetopause is influenced by both the bulk and the gyration terms in similar amounts. Outside of the magnetopause, the motion of the ionospheric plasma is dominated by gyration at high latitudes, the bulk terms dominate close to the equator and friction at high latitudes. In the regions where friction dominates the motion of the ionospheric plasma, the ionospheric plasma travels at a faster speed in the x-direction than the solar wind. There are numerical artifacts in the dayside due to the low number density of the ionospheric plasma.

For the solar wind plasma, the bulk terms are dominant throughout geospace except inside the number density geopause where the gyration terms dominate. With a heavier ionospheric plasma, the mass density geopause structure is associated with regions where there the force dominating the solar wind plasma changes from bulk forces to gyration forces.

During southward IMF, for the ionospheric plasma, the bulk terms are dominant within the number density geopause while the gyration terms become dominant outside of it. The bulk terms for the ionospheric plasma is dependent on the ratio of the ionospheric number density compared to the total plasma number density which will become less than 1/2 outside of the number density geopause. The number density geopause roughly outlines a transition region where the ionospheric plasma is dominated by the bulk terms while outside of the number density geopause, gyration dominates.

In this study, we have not included an inner magnetosphere model or a physical

outflow model to isolate the effects of multifluid MHD on the geopauses and the momentum equations. This shouldn't influence our findings, though. The relationships of the force density terms to the geopause surfaces is not dependent on the accuracy of the magnetospheric structure or the ionospheric outflow pattern. The addition of an inner magnetospheric drift physics model or a polar wind outflow model might change the shape of the geopauses but not how the terms in the momentum equation relate to those boundaries.

Furthermore, this study only examined idealized solar wind conditions and did not take into account dipole tilt or seasonal effects. Again, though, this should not influence the relationship of the momentum equation terms to the geopause locations. Dynamic driving conditions and a case-specific Earth orientation will distort the geopause shapes but not change the physics.

5.5 Conclusion

As a follow up to *Trung et al.* (2019), we analyzed the relationship between the sources in the momentum equation and the geopauses under different ionospheric compositions and IMF condition in a two fluid plasma to explore the physical properties of the number density, mass density, and pressure geopauses.

We have found that for the solar wind, the number density geopause does represent a transition in the physics dominating the solar wind plasma. Inside of the number density geopause, the heliospheric plasma's motion is mostly governed by the gyration terms. Outside of the number density geopause, the solar wind plasma is governed mostly by the bulk terms.

In the context of a two fluid singly ionized plasma, we defined a momentum transfer frequency which is simply the gyration frequency scaled by the number density multiplier seen in the momentum equation. This term gives a new interpretation of the mass density geopause. It represents a boundary where the momentum transfer

frequency from the solar wind plasma to the ionospheric plasma due to gyration is equal to the momentum transfer frequency from the ionospheric plasma to the solar wind plasma.

During northward IMF, we find that within the magnetopause, the ionospheric plasma's motion is governed by the gyration and bulk terms in similar amounts. Outside of the magnetopause, the bulk terms dominate closer to the equator and the gyration terms dominate at high latitudes for the hydrogen only ionosphere. While for the oxygen only ionosphere, the gyration terms dominate along the equator outside of the magnetopause and the friction terms dominate at high latitudes. In contrast, the solar wind is dominated by the gyration terms inside of the number density geopause and dominated by the bulk terms outside of the number density geopause.

During southward IMF, the structures of the bulk terms and the gyration terms seem to be related to the pressure and mass density geopauses. The number density geopause outlines a transition from the bulk terms dominating the ionospheric plasma in the number density geopause to the gyration terms dominating it outside of the geopause.

Friction does not seem to play a dominant role in shaping the geopauses or the dynamics of the heliospheric and ionospheric plasma during both IMF configurations. However, friction has provided an indirect way to determine that the ionospheric plasma could travel at faster speeds than the solar wind plasma in our simulations. This has been seen across all outflow and ionospheric cases presented in this study. Within our simulations, this is possible due to the gyration term. Future space missions such as NASA's gateway mission will be able to aid in measuring outflowing ionospheric plasma velocities.

Further work will examine changes in the geopause structure in relation to the source terms by including inner magnetospheric models such as *Ilie et al.* (2012) and more realistic outflow models (*Glocer et al.*, 2009b).

CHAPTER VI

Conclusions

6.1 Summary

This thesis has focused on the concept of the geopause, a surface defined where physical parameters (number density, mass density, and pressure) of both solar wind and ionospheric plasma are equal. To distinguish the number density, velocity, and pressure between plasma components, modeling required the use of multifluid magnetohydrodynamics through the Space Weather Modeling Framework. The simulations varied the composition at the inner boundary to adjust the mass density of the ionospheric plasma. The simulations also varied the orientation of the solar wind magnetic field to alter the ionospheric outflow. Twelve hours of simulation data was generated and used to generate three studies.

In Chapter 1, we have introduced the Earth magnetospheric environment. In Chapter 2, we described the equations to model the solar wind and the ionospheric plasmas. In Chapter 3, we compared the geopause definitions to the magnetopause to show that there was no single boundary dictating the dominance of solar wind or ionospheric plasma in the magnetosphere. In Chapter 4, we assessed the transient effects of changing the mass density of the ionospheric outflow on the geopauses. In Chapter 5, we compared the force densities in the multifluid MHD momentum equations to the geopauses.

6.2 Study 1: Steady State Characteristics of the Terrestrial Geopause

In chapter 3, the question explored was, "How do the geopauses behave with respect to the magnetopause in steady state?" We compared the geopauses to the magnetopause in both the equatorial (X-Y) and the meridional (X-Z) plane during steady state at the time step of the simulation. The simulations showed that the dayside magnetopause was not influenced by the presence of oxygen in the outflow for both IMF orientations and was larger than the other geopauses. In contrast, the nightside magnetopause was sensitive to the conditions in the outflow. The nightside magnetopause was smaller than the other geopauses with southward IMF. With northward IMF, the nightside magnetopause was the largest structure in comparison with the plasma based geopauses. Our results indicated that no single boundary surface dictates the transition from a solar wind dominated plasma to ionosphere dominated plasma.

6.3 Study 2: Transient Characteristics of the Terrestrial Geopause

In chapter 4, we explored the question, "How do the geopauses behave in response to the solar wind's magnetic field reversal?" We synthesized 12 hours of simulation data across four different ionospheric composition and solar wind magnetic field orientation. After the North-to-South IMF reversal, our simulations indicated that oxygen dominated ionospheric outflows would drive changes in the geopause at a faster rate compared to the hydrogen dominated ionospheric outflows. Additionally, the oxygen dominated outflows would reach steady states at later times compared to the hydrogen dominated outflows. After the South-to-North IMF reversal, our simulations

indicate that the mass density of the ionospheric outflows plays a very small role in the post reversal transient structures of the geopause. This can be explained by the lack of coupling between the solar wind and the Earth's magnetic field which leads to a quenching in ionospheric outflow. The dynamics of magnetotail structures, such as the formation of X-lines and plasmoid releases down the tail, closely match the timing of the dynamics seen in the plasma geopauses, although the locations are often different.

6.4 Study 3: Momentum Sources in Multifluid MHD and their Relation to the Geopauses

In chapter 5, the study aimed to answer the question, "How do the force terms in the multifluid momentum equation relate to the geopauses?" The solar wind plasma is dominated by the bulk terms outside of the number density geopause and dominated by the bulk terms outside of the number density geopause. For the ionospheric plasma, it is more dependent on the orientation of the solar wind magnetic field and the composition. With an oxygen only ionosphere, during southward IMF, the gyration term dominated outside of the number density geopause and the bulk terms dominated inside the number density geopause. For a hydrogen only ionosphere, the transition in dominance from the gyration term outside of the number density geopause to the bulk terms inside of the number density geopause is abrupt. During northward IMF, the magnetopause was the boundary indicating the transition in dominating the ionospheric plasma.

The mass density geopause represents a boundary where gyration frequency scaled by the number density multiplier is the same across both species of plasma. The pressure geopause only provides an indication for outflow.

The friction terms did not play a significant role in governing the motion of the

plasma and the geopauses. However, the friction terms provided an indirect means in determining that the ionospheric plasma within our simulations could travel at speeds faster than the solar wind plasma.

6.5 Further work

Our simulations omitted the ring current. Physical models of ring currents use kinetic theory to model its dynamics. Drift physics can be captured through kinetic theory but not through MHD models. The absence of ring currents in MHD model underestimates the pressure near Earth (*De Zeeuw et al.*, 2004). Further work includes coupling BATS-R-US with the Hot Electron Ion Drift Integrator (*Ilie et al.*, 2012) to model the ionospheric and heliospheric plasma populations in order to capture kinetic physics.

The multifluid simulations used simple conditions where the outflow was at a fixed number density and composition and driven solely by the multifluid MHD equations. As such, future improvements for our studies would use a realistic outflow model such as the Polar Wind Outflow Model (*Glocer et al.*, 2009b) which avoids the need to specify an arbitrary the number density, velocity, and pressure of the inner boundary.

Future studies will include realistic solar wind conditions. Realistic solar wind conditions can be found through NASA's OMNI data set, solar wind data measured by a collection of satellites. These conditions can be included as outer boundary conditions within the Space Weather Modeling Framework. Plasma measurements from NASA satellites will be compared to simulation data for data-model comparisons. NASA's Coordinated Data Analysis Web provides measurements taken by satellites. Orbit data can be used by the SWMF to interpolate the numerical solutions to the satellite location in order to perform data to model comparisons. Geopause analysis will be used in determining the ionospheric plasma contribution to in situ satellite measurements.

Our previous studies have indicated that it was possible during southward IMF conditions for ionospheric plasma to be transported to distances greater than 60 Earth radii (the average Earth-Moon distance). The lunar orbiter Kaguya detected oxygen near the Moon when the Moon was in the plasma sheet (*Terada et al.*, 2017). Further evidence of oxygen on the Moon was through the detection of rust on the Moon at high latitudes (*Li et al.*, 2020).

The NASA gateway mission will help improve the capabilities of forecasting models by adding an additional data point in measuring conditions in the local plasma. The THEMIS B and C spacecrafts currently orbiting the moon do not have ion mass spectrometers to measure the charge to mass ratio of the local plasma. The Heliophysics Environmental and Radiation Measurement Experiment Suite (HERMES) is a suite of instruments that will be onboard of the gateway orbiting the moon. Among them is a ion mass spectrometer that will be able to measure the charge to mass ratio in order to determine the ionized species of the local plasma reaching the moon. This can help constrain parameters used in the friction term within the multifluid model.

Bibliography

Bonizzoni, G., and E. Vassallo (2002), Plasma physics and technology; industrial applications, *Vacuum*, *64*(3), 327–336, doi:10.1016/S0042-207X(01)00341-4, the Fouth Iberian Vacuum Meeting.

Borovsky, J. E., and J. A. Valdivia (2018), The earth's magnetosphere: A systems science overview and assessment, *Surveys in Geophysics*, *39*(5), 817–859, doi:10.1007/s10712-018-9487-x.

Brambles, O. J., W. Lotko, P. A. Damiano, B. Zhang, M. Wiltberger, and J. Lyon (2010), Effects of causally driven cusp o+ outflow on the storm time magnetosphere-ionosphere system using a multifluid global simulation, *Journal of Geophysical Research: Space Physics (1978-2012)*, *115*(A9), doi:10.1029/2010JA015469.

Burch, J. L., T. E. Moore, R. B. Torbert, and B. L. Giles (2016a), Magnetospheric multiscale overview and science objectives, *Space Science Reviews*, *199*(1), 5–21, doi:10.1007/s11214-015-0164-9.

Burch, J. L., et al. (2016b), Electron-scale measurements of magnetic reconnection in space, *Science*, *352*(6290), doi:10.1126/science.aaf2939.

Cassak, P. A., and M. A. Shay (2007), Scaling of asymmetric magnetic reconnection: General theory and collisional simulations, *Physics of Plasmas*, *14*(10), 102,114, doi:10.1063/1.2795630.

Chandler, M. O., and T. E. Moore (2003), Observations of the geopause at the equatorial magnetopause: Density and temperature, *Geophysical Research Letters*, *30*(16), doi:10.1029/2003GL017611.

Chapman, S., and V. C. A. Ferraro (1931), A new theory of magnetic storms, *Terrestrial Magnetism and Atmospheric Electricity*, *36*(2), 77–97, doi:10.1029/TE036i002p00077.

Chappell, C. R., K. K. Harris, and G. W. Sharp (1970), A study of the influence of magnetic activity on the location of the plasmapause as measured by ogo 5, *Journal of Geophysical Research (1896-1977)*, *75*(1), 50–56, doi:https://doi.org/10.1029/JA075i001p00050.

Chappell, C. R., T. E. Moore, and J. H. Waite (1987), The ionosphere as a fully adequate source of plasma for the Earth's magnetosphere, *Journal of Geophysical Research: Space Physics*, *92*(A6), 5896–5910, doi:10.1029/JA092iA06p05896.

De Zeeuw, D. L., S. Sazykin, R. A. Wolf, T. I. Gombosi, A. J. Ridley, and G. Tóth (2004), Coupling of a global MHD code and an inner magnetospheric model: Initial results, *Journal of Geophysical Research: Space Physics*, *109*(A12), doi:10.1029/2003JA010366.

Dungey, J. W. (1961), Interplanetary magnetic field and the auroral zones, *Phys. Rev. Lett.*, *6*, 47–48, doi:10.1103/PhysRevLett.6.47.

Eastwood, J. P., et al. (2017), The economic impact of space weather: Where do we stand?, *Risk Analysis*, *37*(2), 206–218, doi:https://doi.org/10.1111/risa.12765.

Glocer, A., G. Tóth, Y. Ma, T. Gombosi, J.-C. Zhang, and L. M. Kistler (2009a), Multifluid block-adaptive-tree solar wind roe-type upwind scheme: Magnetospheric composition and dynamics during geomagnetic storms-initial results, *Journal of Geophysical Research: Space Physics (1978-2012)*, *114*(A12), doi:10.1029/2009JA014418.

Glocer, A., G. Tóth, T. Gombosi, and D. Welling (2009b), Modeling ionospheric outflows and their impact on the magnetosphere, initial results, *Journal of Geophysical Research: Space Physics*, *114*(A5), doi:https://doi.org/10.1029/2009JA014053.

Glocer, A., M. Fok, X. Meng, G. Tóth, N. Buzulukova, S. Chen, and K. Lin (2013), CRCM + BATS-R-US two-way coupling, *Journal of Geophysical Research: Space Physics*, *118*(4), 1635–1650, doi:10.1002/jgra.50221.

Gloeckler, G., and D. C. Hamilton (1987), AMPTE ion composition results, *Physica Scripta*, *T18*, 73–84, doi:10.1088/0031-8949/1987/t18/009.

Goldstein, J. (2007), Plasmasphere response: Tutorial and review of recent imaging results, in *Solar Dynamics and Its Effects on the Heliosphere and Earth.*, edited by D. N. Baker, B. Klecker, S. J. Schwartz, R. Schwenn, and R. Von Steiger, pp. 203–216, Springer New York, New York, NY.

Gombosi, T. I. (1994), *Generalized transport equations*, p. 187–226, Cambridge Atmospheric and Space Science Series, Cambridge University Press, doi:10.1017/CBO9780511524943.007.

Gombosi, T. I., G. Toth, D. L. D. Zeeuw, K. C. Hansen, K. Kabin, and K. G. Powell (2002), Semirelativistic magnetohydrodynamics and physics-based convergence acceleration, *Journal of Computational Physics*, *177*(1), 176 – 205, doi:https://doi.org/10.1006/jcph.2002.7009.

Gombosi, T. I., et al. (2021), What sustained multi-disciplinary research can achieve: The space weather modeling framework, *J. Space Weather Space Clim.*, *11*, 42, doi:10.1051/swsc/2021020.

Gordeev, E., et al. (2015), Assessing the performance of community-available global mhd models using key system parameters and empirical relationships, *Space Weather*, *13*(12), 868–884, doi:https://doi.org/10.1002/2015SW001307.

Haiducek, J. D., D. T. Welling, N. Y. Ganushkina, S. K. Morley, and D. S. Ozturk (2017), SWMF global magnetosphere simulations of January 2005: Geomagnetic indices and cross-polar cap potential, *Space Weather*, *15*(12), 1567–1587, doi:10.1002/2017SW001695.

Hultqvist, B., M. Øieroset, G. Paschmann, and R. Treumann (1999), *Magnetospheric Plasma Sources and Losses: Final Report of the ISSI Study Project on Source and Loss Processes*, Space Sciences Series of ISSI, Springer Netherlands.

Ilie, R., and M. W. Liemohn (2016), The outflow of ionospheric nitrogen ions: A possible tracer for the altitude-dependent transport and energization processes of ionospheric plasma, *Journal of Geophysical Research: Space Physics*, *121*(9), 9250–9255, doi:10.1002/2015JA022162.

Ilie, R., M. W. Liemohn, J. Kozyra, and J. Borovsky (2010a), An investigation of the magnetosphere-ionosphere response to real and idealized co-rotating interaction region events through global magnetohydrodynamic simulations, *Proceedings of the Royal Society A: Mathematical, Physical and Engineering Sciences*, *466*(2123), 3279–3303, doi:10.1098/rspa.2010.0074.

Ilie, R., M. W. Liemohn, and A. Ridley (2010b), The effect of smoothed solar wind inputs on global modeling results, *Journal of Geophysical Research: Space Physics*, *115*(A1), doi:10.1029/2009JA014443.

Ilie, R., M. W. Liemohn, G. Tóth, and R. M. Skoug (2012), Kinetic model of the inner magnetosphere with arbitrary magnetic field, *Journal of Geophysical Research: Space Physics*, *117*(A4), doi:10.1029/2011JA017189.

Ilie, R., R. M. Skoug, P. Valek, H. O. Funsten, and A. Glocer (2013), Global view of inner magnetosphere composition during storm time, *Journal of Geophysical Research: Space Physics*, *118*(11), 7074–7084, doi:10.1002/2012JA018468.

Ilie, R., N. Ganushkina, G. Tóth, S. Dubyagin, and M. W. Liemohn (2015a), Testing the magnetotail configuration based on observations of low-altitude isotropic boundaries during quiet times, *Journal of Geophysical Research: Space Physics*, *120*(12), 10,557–10,573, doi:10.1002/2015JA021858.

Ilie, R., M. W. Liemohn, G. Tóth, N. Yu Ganushkina, and L. K. S. Daldorff (2015b), Assessing the role of oxygen on ring current formation and evolution through numerical experiments, *Journal of Geophysical Research: Space Physics*, *120*(6), 4656–4668, doi:10.1002/2015JA021157.

Kelley, M. C. (2009), *2 Fundamentals of Atmospheric, Ionospheric, and Magnetospheric Plasma Dynamics*, vol. 96, pp. 27–70, Academic Press.

Klein, K. G., and D. Vech (2019), Solar wind plasma parameter distributions at 1 au, *Research Notes of the AAS*, *3*(7), 107, doi:10.3847/2515-5172/ab3465.

Komar, C. M., A. Glocer, M. D. Hartinger, K. R. Murphy, M.-C. Fok, and S.-B. Kang (2017), Electron drift resonance in the mhd-coupled comprehensive inner magnetosphere-ionosphere model, *Journal of Geophysical Research: Space Physics*, *122*(12), 12,006–12,018, doi:10.1002/2017JA024163.

Kronberg, E. A., et al. (2014), Circulation of heavy ions and their dynamical effects in the magnetosphere: Recent observations and models, *Space Science Reviews*, *184*(1), 173–235, doi:10.1007/s11214-014-0104-0.

Kubyshkina, M., V. A. Sergeev, N. A. Tsyganenko, and Y. Zheng (2019), Testing efficiency of empirical, adaptive, and global mhd magnetospheric models to represent the geomagnetic field in a variety of conditions, *Space Weather*, *17*(5), 672–686, doi:https://doi.org/10.1029/2019SW002157.

Li, S., P. G. Lucey, A. A. Fraeman, A. R. Poppe, V. Z. Sun, D. M. Hurley, and P. H. Schultz (2020), Widespread hematite at high latitudes of the moon, *Science Advances*, *6*(36), eaba1940, doi:10.1126/sciadv.aba1940.

Liemohn, M., et al. (2018), Real-Time SWMF at CCMC: Assessing the Dst output from continuous operational simulations, *Space Weather*, *16*(10), 1583–1603, doi:10.1029/2018SW001953.

Liemohn, M. W., and D. T. Welling (2016), *Ionospheric and Solar Wind Contributions to Magnetospheric Ion Density and Temperature throughout the Magnetotail*, chap. 8, pp. 101–114, American Geophysical Union (AGU), doi:10.1002/9781119066880.ch8.

Ma, Y., A. F. Nagy, K. C. Hansen, D. L. DeZeeuw, T. I. Gombosi, and K. G. Powell (2002), Three-dimensional multispecies mhd studies of the solar wind interaction with mars in the presence of crustal fields, *Journal of Geophysical Research: Space Physics*, *107*(A10), SMP 6–1–SMP 6–7, doi:https://doi.org/10.1029/2002JA009293.

Maggiolo, R., and L. M. Kistler (2014), Spatial variation in the plasma sheet composition: Dependence on geomagnetic and solar activity, *Journal of Geophysical Research: Space Physics*, *119*(4), 2836–2857, doi:10.1002/2013JA019517.

Meng, X., G. Tóth, M. W. Liemohn, T. I. Gombosi, and A. Runov (2012), Pressure anisotropy in global magnetospheric simulations: A magnetohydrodynamics model, *Journal of Geophysical Research: Space Physics*, *117*(A8), doi:10.1029/2012JA017791.

Meng, X., G. Tóth, A. Glocer, M.-C. Fok, and T. I. Gombosi (2013), Pressure anisotropy in global magnetospheric simulations: Coupling with ring current models, *Journal of Geophysical Research: Space Physics*, *118*(9), 5639–5658, doi:10.1002/jgra.50539.

Mitchell, D. G., K. C. Hsieh, C. C. Curtis, D. C. Hamilton, H. D. Voss, E. C. Roelof, and P. C:son-Brandt (2001), Imaging two geomagnetic storms in energetic neutral atoms, *Geophysical Research Letters*, *28*(6), 1151–1154, doi: 10.1029/2000GL012395.

Moore, T. E. (1991), Origins of magnetospheric plasma, *Reviews of Geophysics*, *29*(S2), 1039–1048, doi:10.1002/rog.1991.29.s2.1039.

Moore, T. E., and D. C. Delcourt (1995), The geopause, *Reviews of Geophysics*, *33*(2), 175–209, doi:10.1029/95RG00872.

Moore, T. E., et al. (1999), Ionospheric mass ejection in response to a cme, *Geophysical Research Letters*, *26*(15), 2339–2342, doi:10.1029/1999GL900456.

Najib, D., A. F. Nagy, G. Tóth, and Y. Ma (2011), Three-dimensional, multifluid, high spatial resolution MHD model studies of the solar wind interaction with Mars, *Journal of Geophysical Research (Space Physics)*, *116*, A05204, doi: 10.1029/2010JA016272.

Nakamura, T. K. M. (2021), *The Earth's Low-Latitude Boundary Layer*, chap. 12, pp. 177–191, American Geophysical Union (AGU), doi: https://doi.org/10.1002/9781119815624.ch12.

Pembroke, A., F. Toffoletto, S. Sazykin, M. Wiltberger, J. Lyon, V. Merkin, and P. Schmitt (2012), Initial results from a dynamic coupled magnetosphere-ionosphere-ring current model, *Journal of Geophysical Research: Space Physics*, *117*(A2), doi:10.1029/2011JA016979.

Powell, K. G., P. L. Roe, T. J. Linde, T. I. Gombosi, and D. L. D. Zeeuw (1999), A solution-adaptive upwind scheme for ideal magnetohydrodynamics, *Journal of Computational Physics*, *154*(2), 284 – 309, doi: https://doi.org/10.1006/jcph.1999.6299.

Priest, E., and T. Forbes (2000), *Magnetic Reconnection: MHD Theory and Applications*, Cambridge University Press, doi:10.1017/CBO9780511525087.

Pulkkinen, A., L. Rastätter, M. Kuznetsova, M. Hesse, A. Ridley, J. Raeder, H. J. Singer, and A. Chulaki (2010), Systematic evaluation of ground and geostationary magnetic field predictions generated by global magnetohydrodynamic models, *Journal of Geophysical Research: Space Physics*, *115*(A3), doi:10.1029/2009JA014537.

Pulkkinen, A., et al. (2011), Geospace environment modeling 2008-2009 challenge: Ground magnetic field perturbations, *Space Weather*, *9*(2), doi: 10.1029/2010SW000600.

Pulkkinen, A., et al. (2013), Community-wide validation of geospace model ground magnetic field perturbation predictions to support model transition to operations, *Space Weather*, *11*(6), 369–385, doi:10.1002/swe.20056.

Rastätter, L., M. M. Kuznetsova, A. Vapirev, A. Ridley, M. Wiltberger, A. Pulkkinen, M. Hesse, and H. J. Singer (2011), Geospace environment modeling 2008-2009 challenge: Geosynchronous magnetic field, *Space Weather*, *9*(4), doi:10.1029/2010SW000617.

Rastätter, L., et al. (2013), Geospace environment modeling 2008-2009 challenge: Dst index, *Space Weather*, *11*(4), 187–205, doi:10.1002/swe.20036.

Ridley, A. J. (2007), Alfvén wings at Earth's magnetosphere under strong interplanetary magnetic fields, *Annales Geophysicae*, *25*(2), 533–542, doi:10.5194/angeo-25-533-2007.

Ridley, A. J., and M. W. Liemohn (2002), A model-derived storm time asymmetric ring current driven electric field description, *Journal of Geophysical Research: Space Physics*, *107*(A8), SMP 2–1–SMP 2–12, doi:10.1029/2001JA000051.

Ridley, A. J., D. L. De Zeeuw, T. I. Gombosi, and K. G. Powell (2001), Using steady state mhd results to predict the global state of the magnetosphere-ionosphere system, *Journal of Geophysical Research: Space Physics*, *106*(A12), 30,067–30,076, doi:https://doi.org/10.1029/2000JA002233.

Ridley, A. J., A. D. Richmond, T. I. Gombosi, D. L. De Zeeuw, and C. R. Clauer (2003), Ionospheric control of the magnetospheric configuration: Thermospheric neutral winds, *Journal of Geophysical Research: Space Physics*, *108*(A8), doi:https://doi.org/10.1029/2002JA009464.

Ridley, A. J., T. I. Gombosi, and D. L. De Zeeuw (2004), Ionospheric control of the magnetosphere: conductance, *Annales Geophysicae*, *22*(2), 567–584, doi:10.5194/angeo-22-567-2004.

Ridley, A. J., D. L. De Zeeuw, and L. Rastätter (2016), Rating global magnetosphere model simulations through statistical data-model comparisons, *Space Weather*, *14*(10), 819–834, doi:https://doi.org/10.1002/2016SW001465.

Rubin, M., et al. (2015), Self-consistent multifluid MHD simulations of Europa's exospheric interaction with Jupiter's magnetosphere, *Journal of Geophysical Research: Space Physics*, *120*(5), 3503–3524, doi:10.1002/2015JA021149.

Sharp, R. D., W. Lennartsson, W. K. Peterson, and E. G. Shelley (1982), The origins of the plasma in the distant plasma sheet, *Journal of Geophysical Research: Space Physics*, *87*(A12), 10,420–10,424, doi:10.1029/JA087iA12p10420.

Shelley, E. G., R. G. Johnson, and R. D. Sharp (1972), Satellite observations of energetic heavy ions during a geomagnetic storm, *Journal of Geophysical Research*, *77*(31), 6104–6110, doi:10.1029/JA077i031p06104.

Shim, J. S., et al. (2012), CEDAR Electrodynamics Thermosphere Ionosphere (ETI) Challenge for systematic assessment of ionosphere/thermosphere models: Electron

density, neutral density, NmF2, and hmF2 using space based observations, *Space Weather*, *10*(10), doi:10.1029/2012SW000851.

Siscoe, G. L., G. M. Erickson, B. U. A. Sonnerup, N. C. Maynard, K. D. Siebert, D. R. Weimer, and W. W. White (2001), Global role of $E_{\|}$ in magnetopause reconnection: An explicit demonstration, *Journal of Geophysical Research: Space Physics*, *106*(A7), 13,015–13,022, doi:10.1029/2000JA000062.

Song, P., D. L. De Zeeuw, T. I. Gombosi, C. P. T. Groth, and K. G. Powell (1999), A numerical study of solar wind-magnetosphere interaction for northward interplanetary magnetic field, *Journal of Geophysical Research: Space Physics*, *104*(A12), 28,361–28,378, doi:10.1029/1999JA900378.

Terada, K., S. Yokota, Y. Saito, N. Kitamura, K. Asamura, and M. N. Nishino (2017), Biogenic oxygen from Earth transported to the Moon by a wind of magnetospheric ions, *Nature Astronomy*, *1*(2), 0026, doi:10.1038/s41550-016-0026.

Tóth, G., D. L. De Zeeuw, T. I. Gombosi, W. B. Manchester, A. J. Ridley, I. V. Sokolov, and I. I. Roussev (2007), Sun-to-thermosphere simulation of the 28-30 October 2003 storm with the Space Weather Modeling Framework, *Space Weather*, *5*(6), doi:10.1029/2006SW000272.

Tóth, G., Y. Ma, and T. I. Gombosi (2008), Hall magnetohydrodynamics on block-adaptive grids, *Journal of Computational Physics*, *227*(14), 6967–6984, doi:https://doi.org/10.1016/j.jcp.2008.04.010.

Tóth, G., et al. (2005), Space weather modeling framework: A new tool for the space science community, *Journal of Geophysical Research: Space Physics*, *110*(A12), doi:https://doi.org/10.1029/2005JA011126.

Tóth, G., et al. (2012), Adaptive numerical algorithms in space weather modeling, *Journal of Computational Physics*, *231*(3), 870 – 903, doi:https://doi.org/10.1016/j.jcp.2011.02.006, special Issue: Computational Plasma Physics.

Trung, H.-S., M. W. Liemohn, and R. Ilie (2019), Steady state characteristics of the terrestrial geopauses, *Journal of Geophysical Research: Space Physics*, *124*(7), 5070–5081, doi:10.1029/2019JA026636.

Vasyliūnas, V. M. (2012), The physical basis of ionospheric electrodynamics, *Annales Geophysicae*, *30*(2), 357–369, doi:10.5194/angeo-30-357-2012.

Wang, C.-P., L. R. Lyons, and V. Angelopoulos (2014), Properties of low-latitude mantle plasma in the earth's magnetotail: Artemis observations and global mhd predictions, *Journal of Geophysical Research: Space Physics*, *119*(9), 7264–7280, doi:https://doi.org/10.1002/2014JA020060.

Welling, D. T., and M. W. Liemohn (2014), Outflow in global magnetohydrodynamics as a function of a passive inner boundary source, *Journal of Geophysical Research: Space Physics*, *119*(4), 2691–2705, doi:10.1002/2013JA019374.

Welling, D. T., and A. J. Ridley (2010), Exploring sources of magnetospheric plasma using multispecies MHD, *Journal of Geophysical Research: Space Physics*, *115*(A4), doi:10.1029/2009JA014596.

Welling, D. T., V. K. Jordanova, A. Glocer, G. Toth, M. W. Liemohn, and D. R. Weimer (2015), The two-way relationship between ionospheric outflow and the ring current, *Journal of Geophysical Research: Space Physics*, *120*(6), 4338–4353, doi:10.1002/2015JA021231.

Welling, D. T., G. Tóth, V. K. Jordanova, and Y. Yu (2018), Integration of RAM-SCB into the Space Weather Modeling Framework, *Journal of Atmospheric and Solar-Terrestrial Physics*, *177*, 160 – 168, doi:https://doi.org/10.1016/j.jastp.2018.01.007.

Wiltberger, M., W. Lotko, J. G. Lyon, P. Damiano, and V. Merkin (2010), Influence of cusp O+ outflow on magnetotail dynamics in a multifluid MHD model of the magnetosphere, *Journal of Geophysical Research: Space Physics*, *115*(A10), doi:10.1029/2010JA015579.

Winglee, R. (2000), Mapping of ionospheric outflows into the magnetosphere for varying IMF conditions, *Journal of Atmospheric and Solar-Terrestrial Physics*, *62*(6), 527 – 540, doi:https://doi.org/10.1016/S1364-6826(00)00015-8.

Winglee, R. M. (1998), Multi-fluid simulations of the magnetosphere: The identification of the geopause and its variation with IMF, *Geophysical Research Letters*, *25*(24), 4441–4444, doi:10.1029/1998GL900217.

Winglee, R. M., D. Chua, M. Brittnacher, G. K. Parks, and G. Lu (2002), Global impact of ionospheric outflows on the dynamics of the magnetosphere and cross-polar cap potential, *Journal of Geophysical Research: Space Physics*, *107*(A9), SMP 11–1–SMP 11–12, doi:10.1029/2001JA000214.

Xu, S., M. W. Liemohn, C. Dong, D. L. Mitchell, S. W. Bougher, and Y. Ma (2016), Pressure and ion composition boundaries at Mars, *Journal of Geophysical Research: Space Physics*, *121*(7), 6417–6429, doi:10.1002/2016JA022644.

Young, D. T., H. Balsiger, and J. Geiss (1982), Correlations of magnetospheric ion composition with geomagnetic and solar activity, *Journal of Geophysical Research: Space Physics*, *87*(A11), 9077–9096, doi:10.1029/JA087iA11p09077.

Yu, Y., and A. J. Ridley (2009), Response of the magnetosphere-ionosphere system to a sudden southward turning of interplanetary magnetic field, *Journal of Geophysical Research: Space Physics*, *114*(A3), doi:10.1029/2008JA013292.

Zhang, J., et al. (2007), Understanding storm-time ring current development through data-model comparisons of a moderate storm, *Journal of Geophysical Research: Space Physics*, *112*(A4), doi:10.1029/2006JA011846.